

**CATALYTIC REACTIVITY OF COPPER SURFACES IN THE SYNTHESIS OF
CARBON NANOSTRUCTURES**

A Dissertation

by

BEHNAZ RAHMANI DIDAR

Submitted to the Office of Graduate and Professional Studies of
Texas A&M University
in partial fulfillment of the requirements for the degree of

DOCTOR OF PHILOSOPHY

Chair of Committee,	Perla B. Balbuena
Committee Members,	Jorge Seminario
	Benjamin Wilhite
	Michael J. Demkowicz
Head of Department,	M. Nazmul Karim

May 2019

Major Subject: Chemical Engineering

Copyright 2019 Behnaz Rahmani Didar

ABSTRACT

Graphene and carbon nanotubes exhibit extraordinary and diverse properties, and therefore these nanomaterials are finding an increasing number of applications in many industries. However, the major obstacle in the integration of these nanomaterials into practical devices is the inability to cost-effectively produce them in high qualities and large scales, and tailor them towards specific needs. The catalytic chemical vapor deposition (CCVD) is currently the most common method of synthesis of these nanomaterials, and their associated growth mechanism is a subject of intense study. The central theme to these studies is elucidating how the many different parameters such as temperature, catalyst and substrate type, and carbon source gas type and composition may affect the resulting structure and properties of these nanomaterials.

This study focuses upon the earliest stages of nucleation whereby the carbon-containing precursor gas dissociates on the catalyst surface and forms carbon networks, and how this stage may be affected by environmental parameters. The research presented here was conducted using first-principles based kinetic Monte Carlo simulations and other density functional theory-based theoretical methods to characterize catalytic and growth mechanisms of carbon nanostructures mainly using copper (Cu) as the catalyst, although for comparison, other commonly used transition metals have also been studied alongside Cu.

Results obtained explain, from an atomistic level perspective, why the practice of flowing hydrogen gas alongside methane in the CCVD method is important for methane

dehydrogenation. Results also show that the presence of surface oxygen facilitates methane dehydrogenation on Cu surfaces and inhibits that on nickel surfaces. The decomposition of acetylene on supported Cu and cobalt nanoparticles and the effects of the catalyst support and support doping are also discussed. Some discernible differences are found in the performance of the two metal nanoparticles. In addition, the effect of temperature on the coalescence of small graphene islands on Cu, as studied in this dissertation, provides new insights into graphene growth mechanisms.

DEDICATION

To the memory of my father

ACKNOWLEDGEMENTS

During the conduct of this research, I was fortunate enough to be surrounded by many supportive and helpful individuals. I cherish the energy and effort that I spent on this research and treasure the lessons that I learned and people whom I met, including my colleagues and friends. I thank my committee members for supporting my work and providing constructive feedback to improve it. I am thankful to Dr. Fernando Soto and Luis E. Camacho-Forero for their insightful conversations and helpful lessons.

I am especially grateful to my advisor, Professor Balbuena, for her guidance, support, and brilliant ideas throughout my PhD studies, and for inspiring me to continue on the research path.

I would also like to acknowledge the computational resources provided by the Texas A&M University Brazos HPC cluster and Texas A&M High Performance Research Computing, that executed the calculations reported in this dissertation.

Finally, I am forever thankful to my parents whom have instilled in me the spirit to persevere and the appreciation for the value of knowledge and education, and to my siblings for their support and joyful presence in my life.

CONTRIBUTORS AND FUNDING SOURCES

Contributors

This work was supervised by a dissertation committee consisting of Professors Perla B. Balbuena [advisor], Jorge Seminario and Benjamin Wilhite of the department of Chemical Engineering and Professor Michael Demkowicz of the department of Materials Science and Engineering.

The experimental data and images in Chapter 5 were provided by Professor Homa Khosravian.

All other work conducted for the dissertation was completed by the student independently.

Funding Sources

Financial support for this work was provided by the Department of energy, Basic Energy Sciences, under Grant Numbers DE-FG02-06ER15836 and DE-SC0019379.

TABLE OF CONTENTS

	Page
ABSTRACT	ii
DEDICATION	iv
ACKNOWLEDGEMENTS	v
CONTRIBUTORS AND FUNDING SOURCES.....	vi
TABLE OF CONTENTS	vii
LIST OF FIGURES.....	xi
LIST OF TABLES	xvii
1. INTRODUCTION.....	1
2. THEORETICAL AND COMPUTATIONAL METHODS	10
2.1 The Schrödinger Equation	11
2.2 Density Functional Theory	12
2.2.1 Pseudopotentials	14
2.2.2 Self-Consistent Solution to Kohn-Sham Equation	14
2.2.3 van der Waals Forces in DFT	15
2.2.4 DFT+U.....	16
2.2.5 The Nudged Elastic Band (NEB) Method	16
2.3 Ab Initio Molecular Dynamics	17
2.4 Transition State Theory (TST).....	19
2.4.1 Harmonic Transition State Theory (HTST).....	20
2.4.2 Vibrational Frequency Calculations	20
2.5 Kinetic Monte Carlo	21
2.5.1 Lattice Kinetic Monte Carlo	22
2.5.2 Graph-Theoretical KMC Algorithm	24
3. HYDROCARBON DECOMPOSITION ON COPPER SURFACES: REACTION MECHANISMS	26

3.1 Summary.....	26
3.2 Introduction.....	26
3.3 Computational and System Details.....	29
3.4 Results.....	30
3.4.1 Adsorption of CH ₄ and intermediate Species	30
3.4.2 Dissociation Energy Barriers	31
3.4.3 Pre-Exponential Factors.....	33
3.4.4 Diffusion	33
3.4.5 KMC	34
3.4.5.1 Surface Lattice Grid and Adsorbed Species	34
3.4.6 CH ₄ Dissociation Pathway.....	35
3.4.6.1 Effect of Temperature.....	35
3.4.6.2 Effect of Pressure.....	37
3.4.6.3 Effect of H ₂ in the Feedstock Gas.....	38
3.5 Conclusions.....	39
4. HYDROCARBON DECOMPOSITION ON COPPER SURFACES: OXIDATION EFFECTS.....	41
4.1 Summary.....	41
4.2 Introduction.....	42
4.3 Computational and System Details.....	45
4.4 Results.....	48
4.4.1 Part 1	48
4.4.1.1 Adsorption of Oxygen onto Cu(100) and Cu(111) Surfaces	48
4.4.1.2 Adsorption of Carbon onto Oxygenated Cu(100) and Cu(111) Surfaces.....	50
4.4.1.3 AIMD Study of C Adsorption onto Oxygenated Cu(100) and Cu(111) Surfaces	55
4.4.2 Part 2.....	62
4.4.2.1 CH ₄ Dehydrogenation on Clean Cu (111) and Ni (111) Surfaces.....	62
4.4.2.2 CH ₄ Dehydrogenation on Cu (111) and Ni (111) with 1/16 ML O Coverage	63
4.4.2.3 CH ₄ Dehydrogenation on Cu (111) and Ni (111) with 6/16 ML O Coverage	65
4.4.2.4 Electronic Factors	68
4.5 Conclusions.....	70
5. CARBON STRUCTURES NUCLEATION AND GROWTH.....	73
5.1 Summary.....	73
5.2 Introduction.....	73
5.3 Experimental Details	76
5.4 Computational and System Details.....	78

5.5 Experimental Observations.....	79
5.6 Results.....	81
5.6.1 Adsorption of C ₆ rings and Graphene Islands on Cu (111)	81
5.6.1.1 Rings	81
5.6.1.2 Graphene Fragments	82
5.6.2 Effect of Temperature on the Rotation and Orientation of an Isolated Fragment	83
5.6.3 Effect of Temperature on the Rotations and Alignments of a Pair of Fragments.....	85
5.6.4 Effect of Fragments Proximity on the Rotation and Alignments of Fragments.....	87
5.7 Conclusions.....	90
6. HYDROCARBON DECOMPOSITION ON SUPPORTED NANOPARTICLES	91
6.1 Summary.....	91
6.2 Introduction.....	92
6.3 Computational and System Details.....	96
6.4 Results.....	98
6.4.1 Part 1	98
6.4.1.1 Mo-Doping of the MgO Surface.....	98
6.4.1.2 Adsorption of Cu and Co Atoms and Nanoparticles on Pristine, Mo-Doped and Stepped MgO Surfaces	99
6.4.1.3 The Adsorption and Dissociation of C ₂ H ₂ on Supported Cu and Co Nanoparticles.....	105
6.4.1.3.1 C ₂ H ₂ Adsorption	105
6.4.1.3.2 C ₂ H ₂ Dehydrogenation (C ₂ H ₂ → CCH + H).....	109
6.4.1.3.3 C ₂ H ₂ C-C Bond Scission (C ₂ H ₂ → CH + CH).....	109
6.4.2 Part 2	111
6.4.2.1 Carbon Dissolution/Interaction in Unsupported Nanoparticles	111
6.4.2.2 MgO-Supported Cu Nanoparticles	116
6.4.2.2.1 Supported 32-Atom Cu Nanoparticle.....	117
6.4.2.2.2 Supported 38-Atom Cu Nanoparticle.....	118
6.4.2.2.3 Adhesion Energy between Carburized Cu Nanoparticles and MgO Support.....	119
6.4.2.3 Adhesion of Graphene Fragment to Carburized Supported Cu Nanoparticles	121
6.4.2.4 Charge Density of Carburized Supported Cu Nanoparticles	123
6.4.2.5 Bader Charge Analysis	126
6.5 Conclusions.....	127
7. CONCLUSIONS AND FUTURE DIRECTIONS	130

REFERENCES.....	138
APPENDIX A. HYDROCARBON DISSOCIATION ON COPPER SURFACES: REACTIONS MECHANISMS.....	156
APPENDIX B. OXYGEN ADSORPTION ON LOW-INDEX COPPER SURFACES.....	158
APPENDIX C. ADSORPTION AND DIFFUSION OF CARBON RINGS.....	167
APPENDIX D. C ₂ H ₂ DECOMPOSITION ON SUPPORTED NANOPARTICLES.....	170

LIST OF FIGURES

	Page
Figure 1.1 A section of a graphene sheet showing the lattice base vectors \vec{a} and \vec{b} , and roll-up vector \vec{r} . Red and blue indicate zigzag and armchair rims of nanotubes, respectively, that would yield from rolling up the graphene sheet along those directions. Some chiral indices (n,m) are shown. Filled black circles refer to metallic whereas empty black circles refer to semiconductor chiralities	4
Figure 2.1 Energy profile of a reaction initial state \leftrightarrow transition state \leftrightarrow final state. Forward reaction activation $\Delta E_{a,fwd}$, reverse reaction activation $\Delta E_{a,rev}$ and reaction ΔE_{rxn} energies are noted	23
Figure 2.2 The lattice (graph theoretical) kMC algorithm described in section 2.5.2.....	25
Figure 3.1 Most thermodynamically favorable adsorption configurations and energies of CH ₄ and intermediate species on Cu (111). Cu, C and H atoms are shown in orange, black and white.....	31
Figure 3.2 Energy barriers for reactions involved in the dissociation of CH ₄	32
Figure 3.3 The mapping of adsorbed species involved in the dissociation of CH ₄ onto the Cu (111) surface lattice grid. Here, green sites indicate hollow- <i>fcc</i> sites.....	35
Figure 3.4 The dehydrogenation of CH ₃ ($CH_3 \rightarrow CH_2 + H$) on the lattice grid.....	35
Figure 3.5 Results obtained from KMC of the CH ₄ dissociation on Cu (111) at a) 1200K and b) 1500K temperature and 0.03 mTorr pressure. Bottom curves correspond to the H and H ₂ species of their top figures	36
Figure 3.6 Results obtained from KMC of the CH ₄ dissociation on Cu (111) at 1200K temperature and a) 0.03 mTorr b) 0.5 Torr c) 1 Torr pressure. Bottom curves correspond to the H and H ₂ species of their top figures.....	37
Figure 3.7 Results obtained from KMC of the CH ₄ dissociation on Cu (111) at 1200K temperature and 0.03mTorr pressure and a) 0% H ₂ b) 10% and c) 50% H ₂ molar fraction, in feed. Bottom curves correspond to the H and H ₂ species of their top figures.....	38
Figure 4.1 Adsorption sites of a) Cu(100) and b) Cu(111) surfaces. Grey and brown atoms are Cu atoms on the 2 nd and 3 rd layer from top.....	46

Figure 4.2 Diagram of the O adsorption energy per O atom calculated using DFT (at 0K) for Cu (100) and (111) surfaces. Dashed lines between data points are to aid in visualization	49
Figure 4.3 Side (upper panels) and top (lower panels) view images of a single C atom adsorbed onto Cu (111) at various O coverages, as a result of DFT relaxation at 0K. Cu, O and C atoms are shown in blue, red and brown, respectively	52
Figure 4.4 Side (upper panels) and top (lower panels) view images of a single C atom adsorbed onto Cu (100) with various O coverage, as a result of DFT relaxation at 0K. Cu, O and C atoms are shown in blue, red and brown, respectively	53
Figure 4.5 C adsorption energy per O atom calculated using DFT for Cu (100) and (111) surfaces. Cu, O and C atoms are shown in blue, red and brown, respectively. Dashed lines between data points are to aid in visualization	54
Figure 4.6 Optimized structures (top) and their charge density difference maps (bottom) at 0.38ML O coverage on Cu (100) and Cu (111). Light-blue and yellow clouds represent charge accumulation (negative) and depletion (positive), respectively. O atoms are shown in red, while Cu atoms are shown in blue, grey (2 nd layer from top) and brown (3 rd layer from top). Grey and brown atoms are also <i>hcp</i> -hollow and <i>fcc</i> -hollow sites, respectively. The maps are plotted in isosurface level of 0.005 e/Å ³	56
Figure 4.7 Time evolution of adsorbed C (in brown) on Cu (100) with 0.5ML O coverage obtained from AIMD simulations at 1200K temperature	57
Figure 4.8 Time evolution of adsorbed C (in brown) on Cu (100) with 0.5ML O coverage obtained from AIMD simulations at 600K	58
Figure 4.9 Time evolution of adsorbed C on Cu (111) with 0.5ML O coverage obtained from AIMD simulations at 1200K temperature	60
Figure 4.10 Time evolution of adsorbed C on Cu (111) with 0.5ML O coverage obtained from AIMD simulations at 600K temperature	61
Figure 4.11 Energy profile for CH ₄ dehydrogenation on clean (black) and 1/16 ML Oxygen covered (orange) Cu (111) surfaces. The numbers in parenthesis at the maxima are the energy barriers for each step, and the values at the minima are the reaction energies	62

Figure 4.12 Energy profile for CH ₄ dehydrogenation on clean (black) and 1/16 ML Oxygen covered (grey) Ni (111) surfaces	63
Figure 4.13 Charge density difference maps of a) 1 O* on Cu (111) b) 1 O* on Ni (111) c) 6 O* on Cu (111) and d) 6 O* on Ni (111). Yellow and blue colors represent areas with charge depletion (positive) and accumulation (negative), respectively. (Isosurface level = 0.002 e/Å ³)	66
Figure 4.14 Energy profile for CH ₄ dehydrogenation on clean (black) and 6/16 ML Oxygen covered (brown) Cu (111) surfaces	67
Figure 4.15 Energy profile for CH ₄ dehydrogenation on clean (black) and 6/16 ML Oxygen covered (dark grey) Ni (111) surfaces	67
Figure 4.16 Projected density of states (PDOS) onto the d-orbitals of the metal atoms in clean, 1/16 ML and 6/16 ML O pre-adsorbed Cu (left) and Ni (right) surfaces. The vertical lines indicate d-band centers.....	69
Figure 4.17 PDOS onto CH ₃ molecules in the final state on clean and 1/16 ML and 6/16 ML O pre-adsorbed Cu (left) and Ni (right) surfaces	70
Figure 5.1 The Cu slab and the single graphene overlayer from which the fragments were extracted	78
Figure 5.2 Topographical and differential conductance (dI/dV) STM images of graphene growth on Cu (111), provided by Prof. Homa Khosravian. (A) Graphene islands and C atoms are both observed in one single image before final controlled annealing. (B) Differential conductance (dI/dV) image of the STM image shown in A. Graphene islands look smoother and darker in differential conductance images. (C) Complete graphene coverage over Cu (111) after final annealing. The domain boundaries are visible in this STM image. (D) Differential conductance (dI/dV) image of STM image shown in C. The entire image has the same color, which indicates either all the terraces are Cu (111) or graphene/Cu (111). Other parts will support that the latter is true. (E) Moiré pattern was observed on some terraces. (F) Graphene films grown through the controlled thermal cycling method terminated at Cu (111) step edges but changed their shape (the area inside the black circle shows such a shape change)	80
Figure 5.3 An isolated graphene fragment adsorbed on the Cu (111) surface before AIMD (0ps) and after 10ps at temperatures of 900K and 1200K. The initial orientation (24°) of the fragment	

with respect to Cu lattice is shown in purple at 0ps. The final orientations are 32° for 900K and zero for 1200K.....	84
Figure 5.4 Surface reconstruction observations of the Cu slab in the presence of a graphene fragment taken from 10ps of AIMD simulations performed at temperatures of 900K and 1200K. Light green atoms depict surface Cu atoms	84
Figure 5.5 A pair of graphene fragments adsorbed on the Cu (111) surface (distance between centers of mass = 1nm) before AIMD (0ps) and after 10ps at temperatures of 900K and 1200K. The initial orientations (24°) of both of the fragments with respect to Cu lattice is shown in purple at 0ps. The final orientations at 900K are shown as 35° for the left fragment (in orange) and 4° for the right (in purple). The final orientations at 1200K are 26° for the left fragment (in orange) and 20° for the right (in purple).....	86
Figure 5.6 Surface reconstruction observations of the Cu slab in the presence of a pair of graphene fragments taken from 10ps of AIMD simulations performed at temperatures of 900K and 1200K. Light green atoms depict surface Cu atoms	86
Figure 5.7 A pair of graphene fragments adsorbed on the Cu (111) surface at close vicinity to each other (distance between centers of mass = 0.8nm) and after 10ps at temperatures of 900K and 1200K. The initial orientations (24°) of both of the fragment with respect to Cu lattice is shown in purple at 0ps. The final orientations at 900K are 15° for the left fragment (in orange) and 10° for the right (in purple). The final orientations of both fragments at 1200K are zero	88
Figure 5.8 Surface reconstruction observations of the Cu slab in the presence of a pair of graphene fragments at close vicinity taken from 10ps of AIMD simulations performed at temperatures of 900K and 1200K. Light green atoms depict surface Cu atoms.....	88
Figure 6.1 Modifications to the MgO (100) surface by substitution of Mo (1 and 5atoms) for Mg on the top layer, adsorption of Mo on MgO and insertion of Mo in MgO subsurface. Mg, O and Mo atoms are shown in green, red and blue	98
Figure 6.2 Most favorable adsorption configurations of Cu and Co atoms onto the three types of MgO surfaces. Adsorption energies, bond lengths and Bader charges (orange for Cu/Co and blue for Mo) are also	

indicated. Mg, O, Mo, Cu and Co atoms are shown in green, red, blue, orange and darker blue	100
Figure 6.3 Structure of nanoparticles built by successive addition of atoms. a) and b) Cu ₉ and Co ₉ on MgO, c) and d) Cu ₁₀ and Co ₁₀ on Mo-doped, e) and f) Cu ₁₀ and Co ₁₀ on stepped MgO (i.e. MgO (105)).....	102
Figure 6.4 Adsorption energies of Cu and Co to the MgO surfaces per each addition step	103
Figure 6.5 Nanoparticle cohesive energies on the MgO surfaces per addition of Cu or Co atoms.....	104
Figure 6.6 Side and top views of before and after C ₂ H ₂ adsorption on a) Cu and b) Co, nanoparticles on pristine MgO (100) (shown in green (Mg) and red (O) sticks). Adsorption energies are also indicated. Charge density difference maps (isosurface level=0.001 e/Å ³) before adsorption are also shown. Blue and yellow areas indicate accumulation (negative) and depletion (positive) of charge	106
Figure 6.7 Side and top views of before and after C ₂ H ₂ adsorption on a) Cu and b) Co, nanoparticles on Mo-doped MgO (100) (shown in blue (Mo), green (Mg) and red (O) sticks). Adsorption energies are also indicated. Charge density difference maps (isosurface level=0.001 e/Å ³) before adsorption are also shown. Blue and yellow areas indicate accumulation (negative) and depletion (positive) of charge	107
Figure 6.8 Side and top views of before and after C ₂ H ₂ adsorption on a) Cu and b) Co, nanoparticles on Stepped MgO (i.e. MgO (105)). Charge density difference maps (isosurface level=0.001 e/Å ³) before adsorption are also shown. Blue and yellow areas indicate accumulation (negative) and depletion (positive) of charge. Adsorption energies are also indicated.....	108
Figure 6.9 Energy profiles of left) C ₂ H ₂ → CHC + H and right) C ₂ H ₂ → CH + CH reactions happening on Cu and Co nanoparticles on the three MgO surfaces of study. Activation energy barriers are indicated in blue. The reaction coordinate has arbitrary units and is equivalent to the number of images used in NEB calculations.....	110
Figure 6.10 Initial structures of Cu nanoparticles: a) 38-atom <i>fcc</i> , (b) 55-atom icosahedral, and (c) 68-atom <i>fcc</i>	111
Figure 6.11 Energy of interactions for the successive addition of C atoms into 38-, 55-, and 68-atom Cu nanoparticles compared to 55-atom Ni nanoparticle	112

Figure 6.12 Gradual carburization and structure distortion of the un-supported 38-atom Cu nanoparticle. C atoms are in brown. For “+1C”, the single C atom is at the center of the nanoparticle and is hidden from view	114
Figure 6.13 a) Energy of interaction for the successive addition of C atoms into 32-atom Cu nanoparticles: unsupported and supported on MgO(100) and MgO(111) and b) the 32-atom Cu nanoparticle used on the MgO supports	117
Figure 6.14 Energy of interaction for the successive addition of C atoms into unsupported, MgO(100) and MgO(111) supported 38-atom Cu nanoparticles.....	119
Figure 6.15 Average distance of closest Cu and C atoms to MgO support for all four carburized Cu nanoparticle and support cases. C atoms in both 32- and 38-atom Cu nanoparticles supported by the MgO(111) support are closer to the support compared to the nanoparticles supported by MgO(100) (illustrated in the image to the right)	120
Figure 6.16 Energy of adhesion of the carburized 32- and 38-atom Cu nanoparticles to MgO(100) and MgO(111) supports during successive C atom additions. Adhesion of the Cu nanoparticles to the MgO(111) is greater, and in agreement with Figure 6.15	121
Figure 6.17 (a) Image of graphene fragment adhering to the MgO(100) supported carburized 32-atom Cu nanoparticle. (b) Image of graphene fragment adhering to the MgO(111) supported carburized Cu nanoparticle	122
Figure 6.18 Charge density difference analysis before and after carburization and addition of graphene fragment for (a) MgO(100) supported 32-atom Cu, (b) MgO(111) supported 32-atom Cu, (c) MgO(100) supported 38-atom Cu, and (d) MgO(111) supported 38-atom Cu. Blue and yellow colors represent negative (accumulation) and positive (depletion) charge densities, respectively. Isosurface level = $0.001 e/\text{\AA}^3$	125
Figure 6.19 Average partial atomic charges of the left) carburized unsupported 32- and 38-atom Cu nanoparticles and right) Cu nanoparticle, C atoms, and the graphene fragment in contact with the nanoparticle. Charge transfer is greater for supported Cu nanoparticles, especially among the carbons and graphene fragment.....	126

LIST OF TABLES

	Page
Table 3.1 Energy barriers and pre-exponential factors for the forward (dehydrogenation) and reverse (hydrogenation) reactions involved in the CH ₄ dissociation on Cu (111).....	34
Table 3.2 Diffusion energy barriers and pre-exponential factors of intermediates in the dissociation of CH ₄ on Cu (111)	34
Table 4.1 Adsorption sites and energies for adsorption of single O and C atoms on clean Cu (100) and (111) surfaces. Preferred adsorption sites and energies are marked in bold	49
Table 4.2 Adsorption energies and electronic charge of 1 and 6 O atoms on Cu (111) and Ni (111) surfaces, referring to 1/16 and 6/16 ML O coverages.....	64
Table 6.1 Formation energies of the three types of modifications of the MgO (100) by Mo; substitutional (cation doping), adsorption and insertion. For the substitution of 5Mo atoms for 5Mg atoms, the formation energy is normalized by the number of Mo atoms.....	99
Table 6.2 Adhesion energies between graphene fragment and cluster (carburized nanoparticle) and between support and cluster for all four cases of supported carburized Cu nanoparticles. All energies in eV	123

1. INTRODUCTION

Catalysis plays a pivotal role across many industries. This is because the role of the catalyst is to accelerate a chemical reaction, which would otherwise take a much longer time to occur, by providing a lower energy pathway between the reactant and product. This occurs while the catalyst itself remains unchanged. Catalysis is classified into two main categories: homogeneous and heterogeneous. The advantage of heterogeneous catalysis over that of homogeneous where the catalyst and reactant are in the same phase, is that it allows less waste and toxic compounds and easier catalyst recycling, hence greener catalytic processes [1]. The overarching goal in heterogeneous catalysis is to be able to guide a certain reaction along a certain path and to achieve the highest selectivity possible. Recent advances in theoretical techniques and computational power along with progress in catalysts synthesis and characterization techniques have offered us vast insights into reactions and mechanisms occurring over catalyst surfaces. These advances have allowed investigation of reactions and processes at a relatively fast rate and with the accuracy that is seldom achievable via experimental setups. Specifically, computational heterogeneous catalysis has heralded a new era for the discovery and design of more efficient nanoscale catalysts and associated processes which is benefited from the emerging of nanoscale materials and makes possible their technologies [2].

Graphene and carbon nanotubes (CNT) are fascinating nanomaterials that have revealed extraordinary electrical, mechanical, thermal and optical properties and

potential applications in energy, electronics, biomedical technologies, composites and coatings, sensors, photonics and optoelectronics [3-10]. Although incredibly light weight, these materials are extremely strong.

Graphene is a 2D material consisting of merely carbon (C) atoms arranged in a single layer with a honey-comb lattice. This arrangement stems from the sp^2 hybridization of the s and p orbitals of C atoms. This arrangement is not always a perfect honey-comb lattice with sp^2 bonds. Kinks, grain boundaries, discontinuities, bond abnormalities and attached functional groups are all defects that are usually present in graphene. These defects impart various properties on graphene. The inability to tailor graphene to specific needs and produce it in large scales and high qualities has truly stifled its wide-spread application across different industries. Graphene was first isolated by mechanically stripping off a single layer from graphite (referred to as the “scotch tape method”) [11]. However, the delicacy of this method inhibits its scaling up of production and limits it to small and high quality samples. Graphene can also be synthesized by reduction of graphene oxide [12], although it prolongs graphene production time. However, scale-up of the process, in addition to controlled and selective removal of oxide and/or hydroxyl functionals from the graphene oxide, have posed major challenges [13, 14]. The catalytic chemical vapor deposition (CCVD) is the alternative method which has shown scalability and a fair degree of control over growth [15]. The key parameter in this method is the catalyst which is usually a transition metal (TM). In general, with respect to graphene growth, transition metals are considered powerful catalysts due to their partially filled d orbitals and their ability to dissolve

carbon [5]. Here, the catalyst provides the surface and template upon which the 2D graphene network forms. Any growth of a graphene network begins with the dissociation of a C precursor gas on the surface of the catalyst. The TM catalyst plays a key role in determining the dissociation pathway of the C precursor gas and the active surface species present on the catalyst in early and later stages of growth. One goal (goal *i*) of this dissertation is to *study the pathway through which C is produced from the C containing source gas arriving on the catalyst surface and also the effect which other species and growth parameters may have on this path*, with a special focus on Cu as the TM catalyst.

Carbon atoms from precursor gas dissociation diffuse on the Cu catalyst surface and bond to neighboring carbon atoms. Here, it is important that the catalyst provides C atoms or other C-containing species appropriate channels to diffuse on its surface. This stage, termed as ‘*nucleation*’, is the start of the formation of graphene islands. It is widely believed that defects resulting from grain boundaries stem from the growth of many graphene islands with different orientations and therefore efforts have been focused on finding ways to prevent or correct the disorientations. A second goal (goal *ii*) of this dissertation is to *investigate graphene islands nucleation and the effect that temperature may have on their dynamic evolution on Cu catalyst surfaces*.

Prior to the synthesis of graphene, Iijima reported synthesis and observation of a new type of “finite carbon structure” in 1991 [16]. These structures soon became known as carbon nanotubes. Historically, carbon nanofibers were first fabricated using the arc discharge [16-18] and laser ablation [19, 20] methods which require very high

temperatures. Later on, the catalytic chemical vapor deposition (CCVD) method [21] became the more prevalent method owing to its lower operating temperatures due to the presence of a catalyst, greater control on structure and scalability [4]. A single-walled carbon nanotube (SWCNT) can be imagined as a rolled up form of a graphene sheet. The direction in which the graphene sheet is rolled up, dictates its properties. This direction – the roll-up vector, \vec{r} – is defined as:

$$\vec{r} = n\vec{a} + m\vec{b} \quad (1.1)$$

Where \vec{a} and \vec{b} are lattice base vectors of graphene and n and m are integers. The (n, m) combination is called the chiral index of the SWCNT and is used to identify the SWCNT type. All CNT are either metallic or semiconducting. If $n = m$, the resulting SWCNT has an armchair structure at the rim of the tube and is always metallic. While if $m = 0$, the SWCNT has a zigzag structure at the rim. Any other combination would result in various chiralities of the SWCNT where if $n - m$ is a multiple of 3, the

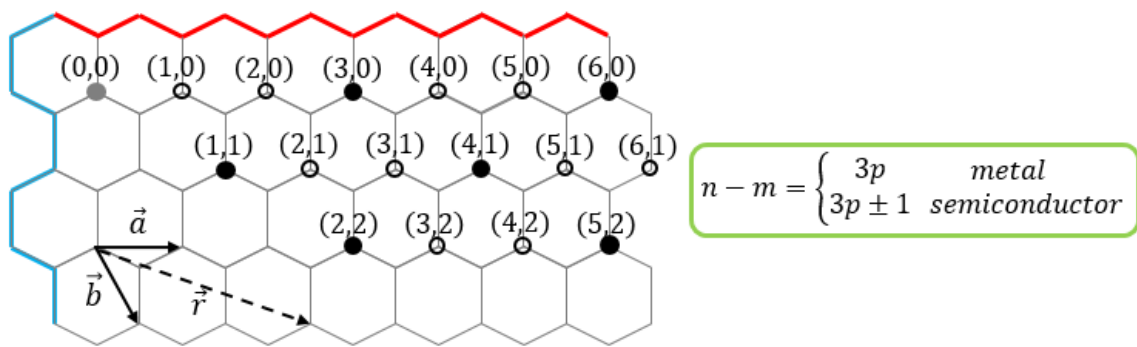


Figure 1.1 A section of a graphene sheet showing the lattice base vectors \vec{a} and \vec{b} , and roll-up vector \vec{r} . Red and blue indicate zigzag and armchair rims of nanotubes, respectively, that would yield from rolling up the graphene sheet along those directions. Some chiral indices (n, m) are shown. Filled black circles refer to metallic whereas empty black circles refer to semiconductor chiralities.

SWCNT would render metallic characteristics [22]. The diameter d of the tube can be calculated from the chiral indices by [23]:

$$d = \frac{\sqrt{3} a_{C-C}}{\pi} \sqrt{n^2 + nm + m^2} \quad (1.2)$$

Where a_{C-C} corresponds to the nearest neighbor C-C distance and $\sqrt{3}a_{C-C}$ is the graphene lattice constant. This is the best and most widely used approach to identify a SWCNT type, although rolling up a graphene sheet is not the method with which SWCNTs are synthesized.

As inferred from above, properties of SWCNT are inherently related to their chirality and structure [4, 24, 25]. Tuning the properties of SWCNT towards a certain application would require the precise control over its growth at every stage and has proven to be a challenging task. Currently, such control over diameter, length, density, structure and chirality has not been entirely achieved and is the subject of intense theoretical and experimental investigation [26].

At present, the CCVD method is the most promising method for both graphene and SWCNT synthesis. The method lies at the intersection of thin layer growth and heterogeneous catalysis and specifically requires a catalyst, either unsupported (floating catalyst) or supported. In the floating catalyst method (FCCVD) [27], the catalyst is usually in the form of an organometallic compound such as ferrocene which evaporates at high temperatures. This catalyst precursor is introduced into a reactor at high temperatures along with a carbon source gas and hydrogen (or another reduction agent) as the carrier gas. Upon insertion, the catalyst precursor vapor is reduced by hydrogen to

metallic nanoparticles and the carbon source gas is catalytically pyrolyzed on the catalyst nanoparticle surface. As such, CNT can be formed continuously as long as the catalyst precursor and carbon source gas are continuously flown in the reactor. In the supported method, the catalyst nanoparticles are deposited on the support from a solution. This system is then heated in a chamber along with a flow of a reducing agent such as H₂. The catalyst may also be prepared from a solution and pulverized into a very fine powder of the catalyst-containing particles and deposited onto the surface of a support. After the catalyst nanoparticles have formed, a flow of C-precursor gas is introduced to the chamber at high temperatures. Thus, carbon nanotubes are produced, provided that the conditions are suitable for growth.

The mechanism of growth for CNT has been most successfully described with the vapor-liquid-solid (VLS) model [28] which is generally used for nanowire growth. In this model, the *vapor* carries the active components onto the *liquid* (due to high temperatures) catalyst where it diffuses into the catalyst, and *solid* precipitates are produced and growth begins. Main factors in this model are the bulk diffusion of the vapor into the liquid and also the liquid state of the catalyst, which are not always observed and rather contradicted at times [29-31]. As such, the growth mechanism remains unclear in many aspects and requires further investigation.

In the CCVD method, the first and crucial role of the catalyst is to adsorb and decompose the C precursor gas into the C atoms necessary for the formation of a C network at early growth stages. It is noted that decomposition of the C precursor gas by the catalyst does not necessarily lead to CNT growth [32]. TM have shown great

potential in this regard, mainly due to their partially filled d orbitals which can overlap with valence orbitals (chemisorption) of carbon, but also due to van der Waals forces [33]. Eventually, the same interactions lead to carbon cap formation. Since TM differ in their d orbital occupancy, interaction strength, and structure from one another, the choice of TM catalyst may therefore play an essential role in determining the resulting CNT chirality.

The catalyst also plays the important role of maintaining the binding to the nanotube and an active rim whereby allowing further growth of the nanotube. In fact, it is believed that the catalyst used in SWCNT growth plays a major role in determining the chirality and diameter of the SWCNT [24, 34, 35]. Statistical analysis of the structures of CNT and catalyst samples obtained from *ex situ* transmission electron microscopy, has led to an interesting observation regarding the relationship between the diameter of CNT and catalyst. In this regard, Fiawoo et al [36] whom performed these experiments and analysis, identified two main contact modes with which the nanotube grows on the catalyst particle; tangential and perpendicular. In the perpendicular mode, the nanotube grows with a diameter smaller than that of the catalyst particle. More specifically, the ratio of the nanotube diameter to that of the particle is less than 0.75. Otherwise, growth is considered as tangential. The relative abundance of these modes were found to be dependent on synthesis time with perpendicular mode being associated with short synthesis time. [33, 36, 37].

The catalyst support has also shown catalytic activity and template and anchoring effect on the catalyst. Undesirable SWCNT growth termination has been ascribed to

catalyst deactivation which may take place due to carbon overlayer (poisoning) [38, 39], catalyst morphological changes [40] and catalyst support evolution brought [41] on at high temperatures. In fact, it is argued that the unifying parameter in all these factors may be the catalyst support [41]. For example, in an experimental study [40], catalyst deactivation and growth termination has been linked to catalyst morphological changes and Ostwald ripening of the metal catalyst, a process whereby metal atoms from small metal particles diffuse to larger metal particles. Undoubtedly, the catalyst support plays a major role in the diffusion of such metal atoms. The size and structure of catalyst nanoparticles is also found to be dictated by the catalyst support, which is especially due to its surface defects such as oxygen vacancies [42, 43].

In terms of catalyst-support interactions, two distinctive growth modes – tip growth and root growth – are identified. When this interaction is weak, the catalyst particle is raised from the support surface as growth of the CNT proceeds and is positioned at the tip of the tube, hence, tip growth. Whereas, stronger interaction would lead to the catalyst particle remaining on the support and the CNT rooting and growing out from the catalyst surface, hence, root growth. Understanding the catalyst and catalyst support and the effect that they may have on the initial stages of growth, can undoubtedly help in the direction of controlling and tuning growth. Nonetheless, such aspects of the catalyst can rarely be experimentally investigated in detail at the nanometer scale in which these events take place. A third goal (goal *iii*) of this dissertation is to *investigate the effect of the catalyst support and the presence of support dopants in the dissociation of the C precursor gas and carburization of the catalyst.*

To achieve the discussed goals, in this dissertation, computational and theoretical methods are used to study several atomistic level aspects of the early stages of growth, focusing on copper as the catalyst. In Chapter 2, an overall description of all computational and theoretical methods, used throughout the dissertation, including density functional theory, *ab initio* molecular dynamics and kinetic Monte Carlo, is presented. Specific details and descriptions of the systems under investigation are further discussed in each chapter. Goal *i* is addressed in Chapters 3 and 4, where first in Chapter 3 the energy barriers of the dissociation reactions of methane, acetylene and ethylene on copper are found. These barriers are then incorporated into a kinetic Monte Carlo scheme to evolve the system in time and understand the kinetics of the dissociation of the precursor gas on copper. Following this section and in Chapter 4, the effect of surface pre-adsorbed oxygen on the adsorption and dissociation of methane is studied. Goal *ii* is addressed in Chapter 5, where *ab initio* molecular dynamics along with an experimental setup are used to study the effect of temperature on graphene island orientations. Goal *iii* is addressed in Chapter 6, where a commonly used metal oxide is used as the support for copper nanoparticle catalysts. The effect of doping the support on the dissociation of a carbon precursor gas on the catalyst is studied. The effect of different facets of the support on carburization and some other factors are also investigated. Finally, in Chapter 7, conclusions of this dissertation study are presented and some future directions are given.

2. THEORETICAL AND COMPUTATIONAL METHODS

Experimental discovery and design of catalysts can involve a costly and tedious trial and error process. Theoretical and computational methods have greatly alleviated this problem and complemented experimental studies by studying catalysts and their effectiveness at a molecular/atomic scale, and with increasing accuracy that can help focus experimental efforts in the most promising of paths [44]. First principles calculations have allowed detailed investigation of systems and explanation of phenomena that are otherwise impossible or difficult to conduct and obtain in experimental settings. Density functional theory (DFT) – a first principles method – calculates the electronic density of a system and allows the determination of its electronic and geometric structure corresponding to the ground state (lowest energy) of that system. From this information, many other properties of the system can be determined. In *ab initio* molecular dynamics (AIMD), these forces and the potential energy of the system are calculated at each time step. A limitation of AIMD is that due to the computational cost of solving the Schrödinger equation at each time step, relatively short simulations can be performed and the statistics is sometimes insufficient [45]. Additional techniques based on DFT include the DFT-based nudged elastic band (NEB) method that finds the minimum energy pathway for a reaction with known initial and final states (structures). Coarse grained methods such as Kinetic Monte Carlo (kMC) provide us with insights into the kinetic performance of a system at certain operating conditions with several competing pathways that have similar energy barriers.

In this chapter, the methods and theories used in this dissertation are described.

2.1. The Schrödinger Equation

The Universe in which we live in can be described, with high accuracy, with the Schrödinger equation. A simple form of this equation is the time-independent form, given by [46]:

$$\hat{H}\psi = E\psi \quad (2.1)$$

Here, \hat{H} is the Hamiltonian operator, ψ is the eigenstates of the Hamiltonian and E is the ground state energy of the system including electrons and nuclei. Solution of this equation, yields the ground state and hence other properties of the system. More precisely, \hat{H} is the sum of kinetic energy of electrons, kinetic energy of nuclei, [Coulombic] interaction energy of electrons with one another, [Coulombic] interaction energy of the electrons with nuclei, and [Coulombic] interaction energy of nuclei with one another:

$$\hat{H} = \hat{K}_E + \hat{K}_N + \hat{U}_{EE} + \hat{U}_{EN} + \hat{U}_{NN} \quad (2.2)$$

These kinetic and interaction energies depend on the spatial coordinates of each electron and the nuclei. In addition, ψ is in fact the electronic wave function, which to a good approximation, is a function of spatial coordinates of electrons. As such, since there are many electrons in any given system, solving the Schrödinger equation – this many-body problem – becomes exceedingly difficult with the increase in system size.

To solve the Schrödinger equation to a fair degree of accuracy, some approximations are necessary. One valid approximation is that since nuclei are significantly more massive and slower than electrons, then electrons follow nuclei

instantaneously and therefore electronic distribution of a system determines the potential for the motion of the nuclei. This is referred to as the Born-Oppenheimer approximation [47]. The Hamiltonian then becomes the sum of kinetic energy of electrons and the interaction energies of electrons with one another, electrons with nuclei and nuclei with one another. To numerically solve the Schrödinger equation, a series of methods such as Hartree-Fock and density functional theory, were successively devised of which only density functional theory will be discussed here.

2.2. Density Functional Theory (DFT)

In DFT, the energy of the system is a functional of the electron density [2, 48, 49]. DFT is based entirely on two fundamental theorems developed by Kohn and Hohenberg in the 1960's. The theorems state that *a) the ground state energy from Schrödinger's equation is a unique functional of the electron density, and b) the electron density that minimizes the energy of the overall functional is the true electron density corresponding to the full solution of the Schrödinger equation* [50]. This electron density can be found from:

$$\rho(r) = 2 \sum \psi^*(r)\psi(r) \quad (2.3)$$

Where the asterisk refers to the complex conjugate and the factor 2 is to account for the fact that each wave function can be occupied by two electrons with opposing spins. It is important to note that the wave function cannot be directly observed. The term $\psi^*(r)\psi(r)$ is, in fact, the probability of an electron being at a certain coordinate, r .

Equations to find the correct density functional were soon after derived by Kohn and Sham [51]. By assuming electrons not interacting with one another, the system of n

interacting electrons simplified to n non-interacting systems of one-electrons. The equations that Kohn and Sham derived are similar to Schrödinger's equation and are in the form of [51, 52]:

$$\left[-\frac{\hbar^2}{2m} \nabla^2 + V(r) + V_H(r) + V_{XC}(r) \right] \psi_i(r) = \varepsilon_i \psi_i(r) \quad (2.4)$$

Now, finding the true electron density requires solving the above set of equations, for each electron. The first term on the left hand side of the equation refers to the electron kinetic energy. The second term is the interaction potential of an electron with the collection of nuclei. The third term, namely Hartree potential, is the interaction potential (Coulombic repulsion) of an electron with the total electron density. All interacting terms are grouped into the fourth term, V_{XC} the exchange-correlation potential. This term consists of the exchange part which is the repulsion between electrons with the same spin and the correlation part which is the sum of interactive (n -electrons) and non-interactive (one-electron) kinetic energies along with the new correlation term due to the n non-interacting one-electron system assumption. Therefore the self-interaction contribution on an electron is accounted for in V_{XC} . The exact form of an exchange-correlation functional is not exactly known. The simplest form of this functional is one in which the electron density is assumed to be constant at any point throughout a uniform electron gas and the local electron density is used to define the functional. This approximation is called the *local density approximation* (LDA) [53]. However, this simplistic form does not faithfully represent the true nature of systems. An improved form of the exchange-correlation functional uses this local electron density

along with the local electron density gradient. This is called the *generalized gradient approximation* (GGA) [54, 55]. Within GGA, many methods have been devised with which the electron density gradient can be approximated. One of the most commonly used functionals is the Perdew-Burke-Ernzerhof (PBE) functional [56] which has been utilized throughout this dissertation. Development of other more accurate functionals is one of the most important and active areas of intense investigation in the field of quantum chemistry.

2.2.1. Pseudopotentials

Due to the sheer number of electrons in any given system, approximations regarding them are especially effective in reducing the computational burden of DFT calculations. Since core electrons are tightly bound to the nucleus and do not define chemical interactions, they can be assumed as *frozen* to the *core*, hence, the frozen core approximation. In this approximation, only the valence electrons are dealt with and Coulomb potential of these valence electrons are described by *pseudopotentials*. One approach to the frozen core approximation is the projector augmented wave (PAW) method [57, 58] which smoothens the wave function while reproducing all-electron results to a high precision. This approach is used throughout this dissertation.

2.2.2. Self-Consistent Solution to Kohn-Sham Equation

Equipped with the foregoing approximations and calculations, a self-consistent iterative algorithm is followed and solved to calculate the energy of the system [45]. First, an initial structure is given by which an initial electron density is known. From this initial density, Kohn-Sham equations yield the wave function, $\psi(r)$, from which a new

electron density is calculated. The two electron densities are compared; if they do not match within a set tolerance, a new electron density is assumed based on the energy eigenvalues calculated. The procedure is repeated until the ground state electronic density and hence ground state energy is found.

Force is a useful parameter in quantum mechanics. At each electronic minimization iteration, the electrostatic force on a nucleus can be conveniently calculated using the equation stated by the Hellmann-Feynman theorem [59, 60]:

$$F = -\frac{dE}{dr} = -\langle \psi \left| \frac{\partial \hat{H}}{\partial r} \right| \psi \rangle = -\frac{\partial \hat{U}_{NN}}{\partial r} - \int \frac{\partial \hat{U}_{EN}}{\partial r} \rho(r) dr \quad (2.5)$$

The DFT method utilizing GGA functional yields reasonable atomic structure, energetics, charge densities and vibrational frequencies, but have shown to fail when dealing with van der Waals (vdW) forces which arise from dispersion interactions [61]. Subsequently, several techniques have been devised to incorporate vdW forces into DFT calculations.

2.2.3. Van der Waals Forces in DFT

To account for the vdW forces, a density-independent term is simply added to the energy density functional [62]. The added dispersion term contains a long range interaction term and a dispersion coefficient. Over the years, the formalism of these two constituents have been improved to dampen the divergence of the long range interaction term and to include more, if not all, chemical elements in the dispersion coefficient term. In this dissertation, the DFT-D3 method of Grimme et al [63] is used which takes into

account the neighboring atoms and their volumes in the calculation of the dispersion coefficient. These values are also updated and adjusted throughout the calculations.

2.2.4. DFT+U

The repulsive self-interaction of an electron and itself is not completely cancelled in DFT functionals. This results in large errors in calculations in strongly correlated systems which give rise to such self-interaction of electrons. Example of such systems are transition metal atoms which have tight-binding and localized *d* and *f* electron orbitals. To account for these interactions, a simple “+*U*” (Hubbard *U*) correction to the DFT functionals such as LDA and GGA was proposed [64, 65]. This correction is only applied to the localized orbitals and not to the remainder of the valence electrons [64]. In recent years, and introduced by Dudarev et al [66], an even simpler approach has gained popularity by which the Coulomb interaction is coupled with exchange correction in a single parameter U_{eff} , given as $U_{eff} = U - J$. There are two approaches to finding the value of the U_{eff} parameter. One is to take a property of the system under study and find the U_{eff} which can reproduce the experimental value of this property. The second approach is to use other kinds of *ab initio* methods that can estimate this parameter [45]. In this dissertation, particularly in chapter 4, the Dudarev method is used where the U_{eff} values for elements are taken from previously published work elsewhere.

2.2.5. The Nudged Elastic Band (NEB) Method

NEB is a valuable DFT-based method used to find the minimum energy pathway (MEP) of a reaction and its energy barrier [67]. This method is based on dividing the path between the reactant and product (the two minima determined *a priori*) into several

images that serve as an initial guess and are connected by an “elastic band”. During an NEB calculation, this elastic band is optimized meaning that the forces perpendicular and along the band are minimized. Hence, the saddle point and energy barrier are found and all images are then along the MEP. The climbing-image method (CI-NEB) [68] is an improvement on NEB in that it identifies the high energy image early on in the calculations, modifies the force on this image and raises it higher on the minimum energy path. Thus, CI-NEB finds the saddle point more efficiently.

2.3. *Ab Initio* Molecular Dynamics

In molecular dynamics (MD), kinetic and potential energies that describe the state of a system are defined by atomic coordinates and velocities.

$$K = \frac{1}{2} \sum_i^{3N} m_i v_i^2 \quad (2.6)$$

$$U = U(r_1, \dots, r_{3N}) \quad (2.7)$$

In classical MD, the forces acting on atoms can be calculated from empirical interatomic potentials and force fields. In turn, these calculated forces yield new atomic positions and velocities via integration of Newton’s law of motion (Equation 2.8), from which new forces acting on each nucleus are calculated [49].

$$F_i = m_i a_i = m_i \frac{dv_i}{dt} \quad (2.8)$$

A major limitation of classical MD is the unavailability of such interatomic potentials and force fields for every specific system of study.

In *ab initio* MD, rather than using empirical force fields to calculate forces acting on each atom, DFT is used to find electronic configurations and potential energy of the

system. Newton's law of motion can then be applied to move atoms with a timestep.

Since force is also related to the first derivative of the potential energy:

$$F_i = -\frac{\partial U}{\partial r_i} \quad (2.9)$$

Therefore from the potential energy, a new set of coordinates and velocities can be derived by integration of Newton's second law:

$$\frac{\partial^2 r_i}{\partial t^2} = \frac{\partial v_i}{\partial t} = -\frac{1}{m_i} \frac{\partial U}{\partial r_i} \quad (2.10)$$

An essentially similar approach to solving the equations of motion, is to define the *Lagrangian*, L , as [69]:

$$L = K - U = \frac{1}{2} \sum_i^{3N} m_i v_i^2 - U(r_1, \dots, r_{3N}) \quad (2.11)$$

Where the L relates the coordinates to velocities by:

$$\frac{\partial}{\partial t} \left(\frac{\partial L}{\partial v_i} \right) = \frac{\partial L}{\partial r_i} \quad (2.12)$$

An imperative factor for the calculations is that some parameters are usually inherently fixed such as number of atoms, system volume and total energy. Temperature is an important parameter in any real system of which other properties can be derived from. The temperature is related to the velocity of atoms through the Maxwell-Boltzmann distribution:

$$\frac{k_B T_{MD}}{2} = \frac{1}{6N} \sum_i^{3N} m_i v_i^2 \quad (2.13)$$

Since the velocity of atoms is not fixed, the temperature of the system during a MD simulation fluctuates. To fix the temperature, an extra term is added to the *Lagrangian* and the *Lagrangian* equations of motion include a term, which can keep the T fixed by raising or reducing velocities [70].

$$\frac{\partial^2 r_i}{\partial t^2} = \frac{\partial v_i}{\partial t} = -\frac{1}{m_i} \frac{\partial U}{\partial r_i} - \frac{\xi}{m_i} v_i \quad (2.14)$$

In summary, classical MD of nuclei is combined with DFT-calculated electronic structure and interparticle forces to integrate the equations of motion in AIMD simulations. During an AIMD simulation, the potential energy is calculated by DFT. In other words, the ground state energy of the system is first calculated. With a given time-step and energy, equations of motion are used to calculate new coordinates for atomic nuclei from which new trajectories are calculated. This process is continued until a sufficient amount of trajectories is collected.

2.4. Transition State Theory (TST)

Developed in the 1930's [71], TST is a reliable theory for the study of elementary reactions occurring on surfaces. The theory divides the potential energy surface (PES) into two regions of reactant region (more reacting area) and product region (final product area). The transition state therefore, lies in the boundary of the two regions. As such, initial and final states refer to the minimum energy configurations of the reactant and product regions, respectively.

TST is based on two assumptions. First, the reactant is thermally equilibrated. This assumption implies that atoms in the initial state have Boltzmann distributed

energies. Second, once the system overcomes the energy barrier towards the final state, it will not reverse towards the initial state.

2.4.1. Harmonic Transition State Theory (HTST)

In HTST, the potential energy is expanded to the second-order Taylor approximation to make harmonic expansion of the PES possible [72]. The harmonic expansion is applied to both the initial state and the [first order] transition state. First order transition state implies that only one eigenmode (vibration) is negative, hence the presence of a single imaginary vibrational frequency at transition state. Following this theory, the HTST rate constant is derived as [73]:

$$r = A \exp\left(-\frac{\Delta E_a}{k_B T}\right) \quad (2.15)$$

Where A is the pre-exponential factor, ΔE_a is the activation energy, k_B is the Boltzmann factor and T is temperature.

2.4.2. Vibrational Frequency Calculations

Following HTST, the pre-exponential factor, A , can be calculated by the use of vibrational frequencies. For a system of N atoms, the ratio of the products of $3N$ vibrational frequencies of initial $\nu_i^{initial}$ and the $3N - 1$ vibrational frequencies (here, the imaginary frequency at the transition state is excluded) of transition states $\nu_i^{transition}$ yields A [72, 74]:

$$A = \frac{\prod_i^{3N} \nu_i^{initial}}{\prod_i^{3N-1} \nu_i^{transition}} \quad (2.16)$$

The pre-exponential factors are typically on the order of $10^{12} - 10^{13} \text{ s}^{-1}$. Variations in vibrations from one system to another are very small. On the other hand,

small changes in reaction activation energies, lead to major changes in $\exp(-\frac{E_a}{k_B T})$. Since such changes are much more significant than the vibrational changes, in most cases using the typical values is sufficient.

2.5. Kinetic Monte Carlo (KMC)

Molecular dynamics (MD) is a very useful method in determining the dynamics (time evolution) of a system. However, some processes of interest can occur very infrequently or rarely, as once over a long time scale, which MD cannot efficiently cover. Precisely for this reason, kMC algorithms were designed to focus on the crossings of barriers of the interesting events and coarse-grain all others [75]. To this end, transition state theory (TST) is used to explain the statistics of events and barrier crossings (transitions). A major assumption in TST is that reactant and transition states are at a quasi-equilibrium state. Thus, statistical mechanics laws can be used to derive rate constants which will provide a statistical description of the transition.

KMC can simulate the change in number and locations of species on a catalyst surface, represented as a lattice. Species can adsorb and diffuse on, react with another and desorb from the lattice.

For any state i , the probability that the system remains in this state is:

$$P_{ii}(t) = \exp(-k_{tot}t) \quad (2.17)$$

From this, the probability of the system leaving the state can be deduced as $1 - P_{ii}(t')$. k_{tot} is the rate constant that defines the probability of leaving of a particular state and $k_{tot} = \sum_j k_{i \rightarrow j}$. This rate constant can be readily deduced from first-principles calculations.

The probability of a system at state i changing to state j at the same time, t , is then given as:

$$P_{ij} = \frac{k_{i \rightarrow j}}{k_{tot}} \exp(-k_{tot}t) \quad (2.18)$$

The time Δt for a transition to occur, can easily be found from equations (2.17) or (2.18) and:

$$\Delta t = -\ln(RN) \frac{1}{k_{tot}} \quad (2.19)$$

Where RN is a random number and $RN \in [0,1]$. The rate at which the probability of being in state i is changed, is given by the probability of entering state i from j , and exiting state i to another state j .

$$\frac{dP_i}{dt} = \sum_{j \neq i} k_{j \rightarrow i} P_j(t) - \sum_{j \neq i} k_{i \rightarrow j} P_i(t) \quad (2.20)$$

Equation (2.20) is defined as the Markov chain Master equation. P_i is the probability of being in state i . The system is given an initial trajectory from which is allowed to evolve from one state to another. Given transitions and their rate constants, $k_{i \rightarrow j}$ and $k_{j \rightarrow i}$, solving equation (2.20) would yield the evolution of the system.

2.5.1. Lattice Kinetic Monte Carlo

Lattice kMC was developed to simulate adsorption, desorption, diffusion and reactions taking place on a lattice surface [76]. The simplest model of this class of kMC assumes single sites of adsorption/desorption and a maximum of two sites for elementary reactions. This simplistic model becomes inadequate for complex systems where species are large and may involve multiple dentate and adsorption sites.

Recently, a graph-theoretical kMC methodology was devised in the Vlachos research group [77] where events and lattice structure are represented by graphs. An advantage of this methodology is that it allows the inclusion of coverage effects where the activation of an event depends on the event neighboring.

The energy profile of a reaction is shown in **Figure 2.1**. The rate of the forward reaction can be calculated for a certain surface coverage θ by:

$$r_{fwd} = A_{fwd} \exp\left(-\frac{\Delta E_{a,fwd}(\theta)}{k_B T}\right) \quad (2.21)$$

And the reverse reaction by:

$$r_{rev} = A_{rev} \exp\left(-\frac{\Delta E_{a,rev}(\theta)}{k_B T}\right) \quad (2.22)$$

The reaction energy based on microscopic reversibility for θ surface coverage is:

$$\Delta E_{rxn}(\theta) = \Delta E_{a,fwd}(\theta) - \Delta E_{a,rev}(\theta) \quad (2.23)$$

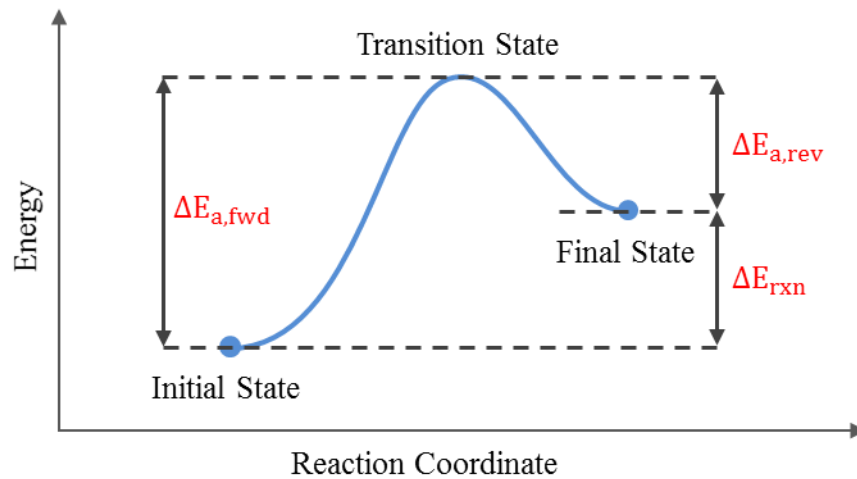


Figure 2.1 Energy profile of a reaction initial state \leftrightarrow transition state \leftrightarrow final state. Forward reaction activation $\Delta E_{a,fwd}$, reverse reaction activation $\Delta E_{a,rev}$ and reaction ΔE_{rxn} energies are noted.

However, it can be calculated from the energetics that are input to the system (cluster expansion Hamiltonian) obtained *a priori* from DFT calculations.

The forward activation energy is then parameterized via the BEP relationship:

$$\Delta E_{a, fwd}(\theta) = \max\{0, \Delta E_{rxn}(\theta), \Delta E_{a, fwd}(0) + \omega[\Delta E_{rxn}(\theta) - \Delta E_{rxn}(0)]\} \quad (2.24)$$

Accordingly, the reverse activation energy can be obtained from equations (2.23) and (2.24). Here, $\Delta E_{a, fwd}(0)$ and $\Delta E_{rxn}(0)$ refer to zero coverage limit forward activation and reaction energies and ω is the proximity factor ranging from 0 (initial-state-like transition state) to 1 (final-state-like transition state).

2.5.2. Graph-Theoretical KMC algorithm

The procedure for a graph theoretical kMC simulation of a system starts by defining simulation parameters (time, temperature, pressure, etc....) and setting up the lattice and connectivity of sites and adsorption configuration of adsorbates to the lattice and their dentates (segment of an adsorbate specie that binds to a certain surface site). The energetics of each adsorbate and intermediate specie obtained from DFT calculations is entered. Reaction mechanisms describing all possible events are also entered. The kMC algorithm (see **Figure 2.2**) then follows the master equation statistics (**Equation 2.20**) where a process is chosen and executed; the time change is calculated and advanced; all structures and information are updated and thus, kMC is proceeded to the next step. This process is repeated until the set time is reached.

KMC calculations in this dissertation were carried out using *Zacros*, a Fortran2003 software package developed by Michail Stamatakis at University College London [78].

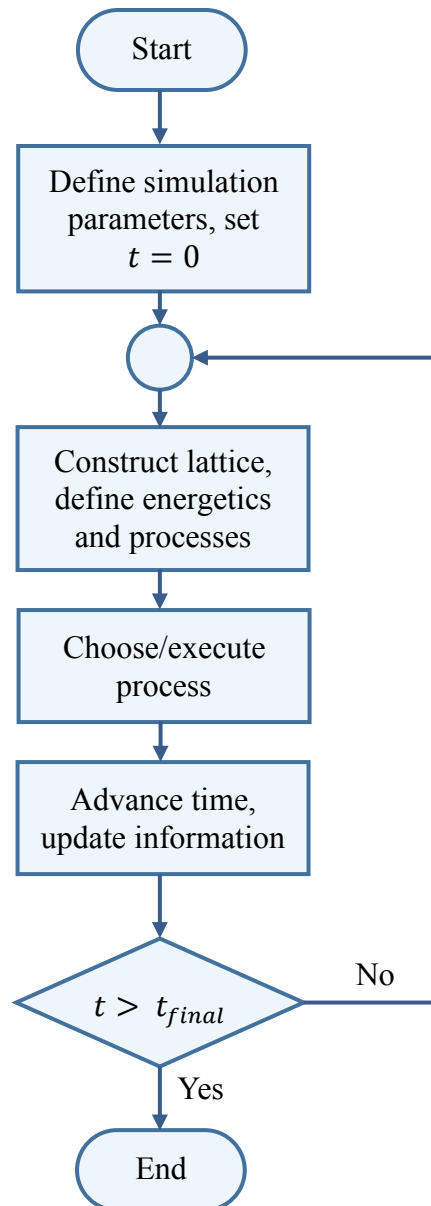


Figure 2.2 The lattice (graph theoretical) kMC algorithm described in section 2.5.2.

3. HYDROCARBON DECOMPOSITION ON COPPER SURFACES: REACTION MECHANISMS

3.1. Summary

First-principles DFT calculations are carried out to evaluate the thermodynamics of CH₄ decomposition on the clean surface of Cu (111). Energy barriers and pre-exponential factors of reactions involved in the decomposition are calculated. This information is then fed into kMC simulations to combine the kinetics and spatio-temporal factors along with the thermodynamics to evaluate the decomposition pathway and its evolution with time.

3.2. Introduction

Graphene has the potential to transform and impact many industries. However, implementation of this material in current or new technologies has been hampered at a very fundamental stage by the inability to produce it in large scales and high qualities. The CCVD method is the most common method of growth in which a carbon-containing precursor gas is vaporized on the surface of a transition metal such as Cu, Ni, Ir and Pt used as the catalyst. Among them, Cu has emerged as the most promising catalyst [79-81] although graphene growth is also achieved on the other aforementioned transition metals. In the CCVD method, the mechanism of growth is described as: 1) adsorption and dissociation of the carbon (C) precursor gas, 2) dissociation and dehydrogenation, 3) diffusion, and 4) nucleation and growth [5, 15]. Owing to the low C solubility in Cu and weak bonding between C and Cu, the growth mechanism on Cu has been described as

surface-mediated [15]. On other transition metals, C solubility is higher and it can dissolve into the bulk of the catalyst, forming a carbide. Rapid precipitation/segregation of a C network upon cooling results in a graphene sheet [15, 82]. Regardless of the type of transition metal, the decomposition of the C precursor gas on the surface of the catalyst is the first step of the CCVD growth process.

Common C precursor gases of graphene and carbon nanotubes (CNT) are carbon monoxide (CO), ethanol (C₂H₅OH), and alkanes such as methane (CH₄), acetylene (C₂H₂) and ethylene (C₂H₄). Alkanes exhibit very low reactivity due to their strong C-H bonds. Alkane dehydrogenation studies especially that of CH₄, which involves C-H bond scission, has been well established on clean metallic [83-86] surfaces. In addition, bi-metallic [83, 87, 88] and stepped metallic [89, 90] surfaces have also been investigated and found to be more preferable for the dissociation of CH₄ [91]. In fact step edges have been recognized as dynamic growth sites for graphitic networks where alkanes such as CH₄ dissociate on the transition metal catalyst surface, successively lose their H's and transform into C networks.

In many studies CH₄ [79, 92-95] is the most common precursor gas and is flown into the chamber alongside H₂. Compared to other C precursor gases, CH₄ requires higher temperatures to induce dissociation [96]. Graphene has also been synthesized without H₂ [97], since active H is provided by the pyrolysis of CH₄, if it were to play a role in precursor gas dissociation and graphene nucleation and growth [98]. The role of H₂ in the graphene growth process has been varyingly described in the literature as etching of carbon networks [98, 99], etching only when accompanied by other impurities

[100], activator of surface C [101] and passivating of graphene island edges [102] for bi- or multi-layer graphene formation, and facilitating/inhibiting the decomposition of precursor gas [98, 103]. In CNT growth, hydrogen is believed to play an important role in determining the CNT structure and its effect has been studied based on its source. On the one hand, it is believed that the catalyst precursor is reduced to the catalyst by the hydrogen formed from the initial dissociation of the hydrocarbon in the CVD chamber [104]. On the other hand, H₂ gas accompanying the C-precursor gas in the feedstock has been shown to activate the catalyst. Excessive H₂ amounts lead to amorphous carbon nanofibers [105, 106]. In both cases, any effect that hydrogen may have on CNT growth is linked to its effect on the catalyst.

The dissociation path of the C precursor gas and its end product plays a major role in growth rate, quality and morphology of the produced graphene. This dissociation on transition metals has been studied in detail using theoretical methods. Studies indicate that in the case of CH₄ as the precursor gas, CH is the most stable species of the dissociation path on Cu (111) and (100) [85, 107]. However, a recent study conducted over several different transition metals including Cu, Ni and Co showed that the decomposition product of CH₄ depends on the transition metal surface that catalyzes this decomposition [84]. In all of these DFT approaches, CH₄ adsorption on the catalyst surface is carried out in the absence of any other species such as H₂ that are actually almost always present in experimental settings. In fact, the existence of such species arise from the dissociation process of the C precursor gas itself. A theoretical study utilizing *ab initio* molecular dynamics simulations of pure CH₄ on Cu at a temperature of

1300K, found no adsorption or dissociation of CH₄ on Cu for the extremely short 3.63ps that the simulation was allowed to proceed [108]. Inevitably, these observations point to the much less known role of such species on the catalyzed precursor gas adsorption and dissociation.

In this chapter, the atomistic processes involved in the transformation of C precursor gas (CH₄) to C needed for growth is investigated. The activation energy barriers and pre-exponential factors for the decomposition reactions on the clean surface of Cu (111) are calculated using DFT. This information is then fed into a KMC simulator, where the temperature and spatial factors are also entered into the study and dissociation pathways are allowed to compete to yield a more realistic dissociation mechanism. The effect that accompanying H₂ with the C precursor gas in the feedstock gas may have on the dissociation pathway is also studied.

3.3. Computational and System Details

DFT calculations were performed using the Vienna Ab initio Simulation Package [58, 109, 110] with the PBE functional within the generalized gradient approximation GGA method for the electron-electron interactions [56] and the projector-augmented wave (PAW) pseudopotentials for the electron-ion core interactions [57, 58, 111]. Dispersion forces were accounted for by using the DFT-D3 correction method of Grimme et al [63]. The surface of Cu (111) is represented by a slab consisting of a $p(3 \times 3)$ supercell arranged in four atomic layers of which the top two were allowed to fully relax during all calculations. Periodically repeated slabs were separated by a vacuum of 10 Å thickness to avoid interactions of the slab with its upper/lower periodic images. A 3×3

$\times 1$ k-point mesh with a plane wave energy cutoff of 400 eV was selected for the sampling of the Brillouin zone.

The minimum energy path for reactions were calculated using the climbing-image nudged elastic band (CI-NEB) method [68], reaching convergence when the force normal to the reaction path was less than $0.05\text{eV}/\text{\AA}$. Between 3-9 images were considered for these calculations.

As described in Chapter 2, vibrational frequency calculations in DFT were performed to estimate pre-exponential factors. Pre-exponential factors and activation barriers obtained from DFT were then used in the GT-kMC, as implemented in the software package Zacros [78].

3.4. Results

3.4.1. Adsorption of CH_4 and intermediate Species

The first step in determining reaction energy barriers is to find the lowest-energy (most thermodynamically favorable) adsorption sites, adsorption energies and configurations of CH_4 and intermediate species. DFT calculations were used for this purpose and thus, initial and final states of reactions were found. The adsorption energy for any CH_x specie was calculated as:

$$E_{ads} = E_{\text{Cu-CH}_x} - E_{\text{Cu}} - E_{\text{CH}_x} \quad (3.1)$$

Here, $E_{\text{Cu-CH}_x}$, E_{Cu} and E_{CH_x} are the energies of the Cu-adsorbed CH_x specie, the Cu (111) slab and the CH_x specie in the gas phase, respectively. **Figure 3.1** depicts the configurations and adsorption energies. The weakly-bound CH_4 (-0.25 eV) does not in fact adsorb to the surface. All other species adsorbed most favorable to hollow-*fcc* sites.

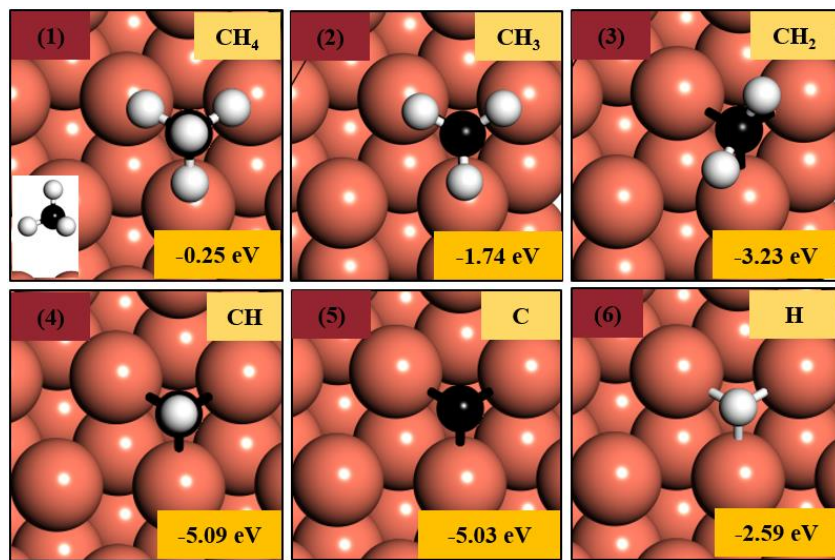


Figure 3.1 Most thermodynamically favorable adsorption configurations and energies of CH₄ and intermediate species on Cu (111). Cu, C and H atoms are shown in orange, black and white.

The highest adsorption energies belong to the C monomer and CH with energies of – 5.03 eV and –5.09 eV, respectively. The high stability of these species on the Cu (111) surface has been observed in the literature [85, 107, 112].

3.4.2. Dissociation Energy Barriers

The dissociation reactions of CH₄ to C involves dehydrogenation/hydrogenation reactions. The structures depicted in **Figure 3.1** serve as a guide for the initial and final states of all reactions. The H in these dehydrogenation/hydrogenation reactions which is desorbed/co-adsorbed from/with a CH_x specie, was placed at the most stable site (*fcc*) some distance away from the CH_x specie and the system was relaxed. NEB calculations were performed for each reaction to find transition states and reaction energy barriers. **Figure 3.2** shows all possible reactions and their energy barriers involved in the dissociation of CH₄. Energy profiles of all reactions can be found in **Appendix A**.

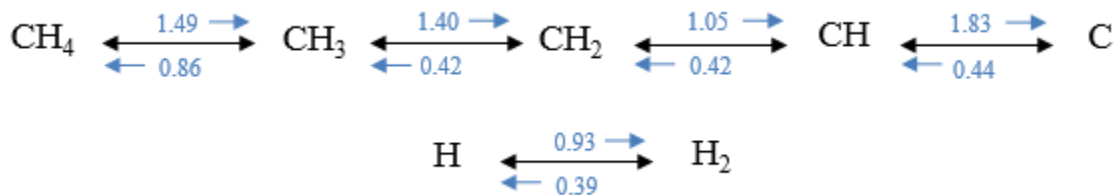


Figure 3.2 Energy barriers for reactions involved in the dissociation of CH₄.

Hydrogenation reactions involving C have lower energy barriers compared to dehydrogenation reactions. However, the dehydrogenation reaction of $H_2 \rightarrow H + H$ has a lower barrier than its reverse, and therefore the formation of atomic H, from H₂ gas, on the Cu (111) surface may be very likely. One of the most important features of CH₄ dissociation on Cu (111) is its highest energy barrier (1.83 eV) which belongs to the $CH \rightarrow C + H$ reaction. This high energy barrier coupled with the high adsorption energy of CH (-5.09 eV) found in the previous subsection (see **Figure 3.1**), points to the high stability of CH species and the less likeliness of finding C monomers on the Cu (111) surface, although C adsorption energy is quite high. This has been confirmed in studies elsewhere [107, 113-115]. The defining characteristic of the Cu surface compared to other transition metals, may well be its low tendency for carbon solubility and monomer formation from hydrocarbon on the one hand but high tendency of C dimer and generally C-C bond formation, on the other. In addition, the energy barrier corresponding to H₂ dissociation are comparable to those of CH₄ dissociation. Therefore these reactions and their products are likely to compete on the Cu (111) surface and for available adsorption sites and require further investigation using KMC.

3.4.3. Pre-Exponential Factors

Vibrational frequencies of initial, transition and final states of all reactions were calculated. The pre-exponential factors, A_{fwd}^{calc} (forward reaction) and A_{rev}^{calc} (reverse reaction), were then calculated using the procedure described in Chapter 2. Results are shown in **Table 3.1** for CH₄. It is noted that the factors for reaction 1 are not calculated since CH₄ adsorbs very weakly to the surface and vibrational frequency is hardly detected.

3.4.4. Diffusion

One of the advantages of lattice KMC is the inclusion of spatial effects which is not possible with DFT. Species are allowed to diffuse on the lattice and react with one another. NEB calculations were performed to find the energy barriers for the diffusion of species (see **Table 3.2**). Since H and all CH₄ dissociation intermediates adsorb favorably onto only one site (hollow-*fcc*), diffusion was considered to occur from the hollow-*fcc* to the hollow-*hcp* site and the reverse. Evidently, the energy barrier for the diffusion of H and all CH_x species are very low. Therefore these species are highly mobile on the Cu (111) surface and diffusion is not likely to be limiting. Although, lower pre-exponential factors for diffusions may impede their easy diffusion.

Table 3.1 Energy barriers and pre-exponential factors for the forward (dehydrogenation) and reverse (hydrogenation) reactions involved in the CH₄ dissociation on Cu (111).

	Reaction	$A_{fwd}^{calc} [s]^{-1}$	$\Delta E_{a,fwd}$	$A_{rev}^{calc} [s]^{-1}$	$\Delta E_{a,rev}$
1	CH ₄ → CH ₃ + H	–	1.49	–	0.86
2	CH ₃ → CH ₂ + H	7.0×10^{13}	1.40	3.4×10^{13}	0.42
3	CH ₂ → CH + H	1.0×10^{13}	1.05	1.0×10^{13}	0.42
4	CH → C + H	2.4×10^{13}	1.83	2.3×10^{13}	0.44
5	H + H → H ₂	1.5×10^{13}	0.93	3.2×10^{13}	0.39

Table 3.2 Diffusion energy barriers and pre-exponential factors of intermediates in the dissociation of CH₄ on Cu (111).

Specie	$A^{calc} [s]^{-1}$	$\Delta E_{a,diff}$
CH ₃	1.0×10^{12}	0.18
CH ₂	4.5×10^{12}	0.19
CH	4.1×10^9	0.13
C	4.5×10^{13}	0.12
H	1.2×10^{12}	0.14

3.4.5. KMC

To understand the kinetics involved in the dissociation process of interest here, it is necessary to evolve the system in time. KMC also makes possible the consideration of all competing mechanisms and pathways in the dissociation process.

3.4.5.1. Surface Lattice Grid and Adsorbed Species

The Cu (111) surface can be represented by a lattice of interlocking triangles and circles at intersection points where the triangles represent the hollow (*fcc* and *hcp*) sites

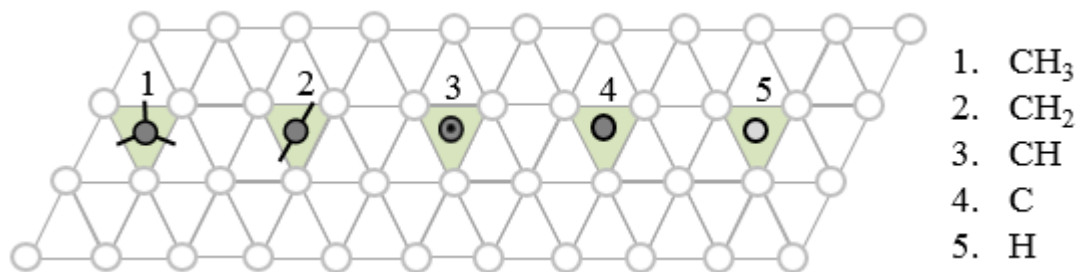


Figure 3.3 The mapping of adsorbed species involved in the dissociation of CH_4 onto the Cu (111) surface lattice grid. Here, green sites indicate hollow-*fcc* sites.

and circles represent *top* sites. The total lattice surface was chosen as approximately $50 \times 50 \text{ \AA}^2$. **Figure 3.3** shows a segment of the mapping of **Figure 3.1** adsorption configuration of species onto the KMC lattice grid. Similarly, reactions can also be described and mapped onto this lattice. An example of a reaction occurring on the lattice grid is shown in **Figure 3.4**. Other reactions are similarly described in KMC. In this study, simulations were initiated on an empty lattice.

3.4.6. CH_4 Dissociation Pathway

3.4.6.1. Effect of Temperature

Typical temperatures used in the CCVD growth of graphene and CNT on Cu using CH_4 are in the range of 1000 –1500 K [5, 116]. Generally, ultra-high vacuum (UHV) and low pressures in the range of 0.5–50 Torr [5, 79, 95, 97] are used however

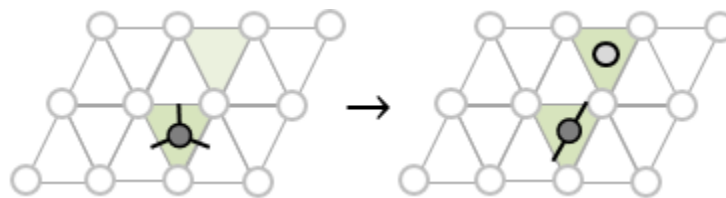


Figure 3.4 The dehydrogenation of CH_3 ($\text{CH}_3 \rightarrow \text{CH}_2 + \text{H}$) on the lattice grid.

atmospheric pressures have also been variedly used throughout the literature [92, 97, 116]. Here, the effect of temperature on the dissociation of CH₄ was studied by considering two temperatures of 1200K and 1500K. The pressure was kept at a constant 0.03 mTorr. Results are illustrated in **Figure 3.5**. After the adsorption of CH₄, CH₃ is produced first. At 1200K (**Figure 3.5a**), CH₂ production is so fast that it is not observed however, the production of CH is seen. Clearly, there is no production of C. The occurrence of these dehydrogenation reactions, increases the amount of H on the surface. However, seemingly the temperature is not high enough to overcome the 0.93 eV barrier to form H₂ and desorb to the gas phase.

At 1500K (**Figure 3.5b**), CH₃ is produced up to a certain amount, after which it is consumed to produce immediate CH₂ followed by CH. At this higher temperature, C is very fast and is simultaneously produced with CH. It is clear that the higher temperature helps in overcoming the large energy barrier (1.83 eV) for $CH \rightarrow C + H$

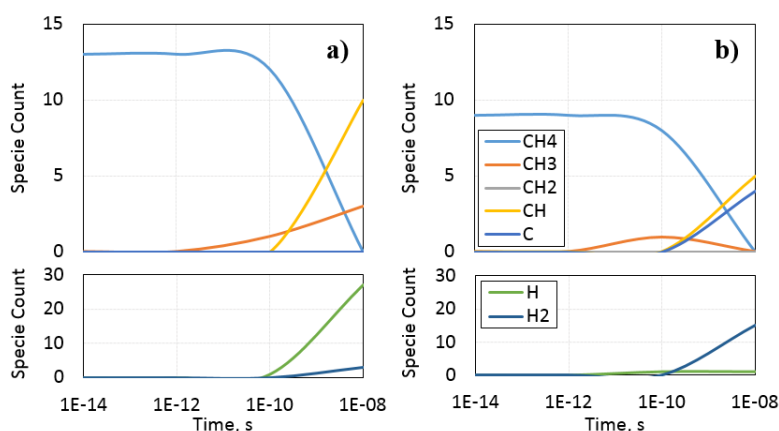


Figure 3.5 Results obtained from KMC of the CH₄ dissociation on Cu (111) at a) 1200K and b) 1500K temperature and 0.03 mTorr pressure. Bottom curves correspond to the H and H₂ species of their top figures.

reaction leading to the production of C and H. With the dehydrogenation reactions taking place, the amount of H is increased and due to the high temperature, the 0.93 eV energy barrier is overcome and H₂ is produced to the gas phase, as seen in the figure below **Figure 3.5b**. The decrease in H on the surface, prevents re-hydrogenation reactions, which in fact have low energy barriers, of taking place. Therefore, C production is able to take place.

3.4.6.2. Effect of Pressure

To study the effect of pressure, the temperature was kept a constant 1200K. **Figure 3.6** depicts the CH₄ dissociation studied at three pressures of 0.03 mTorr (UHV), 0.5 Torr and 1 Torr. With the increase in pressure from UHV to 0.5 Torr and 1 Torr, the production of CH declines. On the other hand, when the amount of H on the surface begins to decline, CH and CH₂ begin to form, and the production of H₂ increases which indicates the conversion of H to H₂(g) through $2H \xrightarrow{0.93eV} H_2$. With little to no H

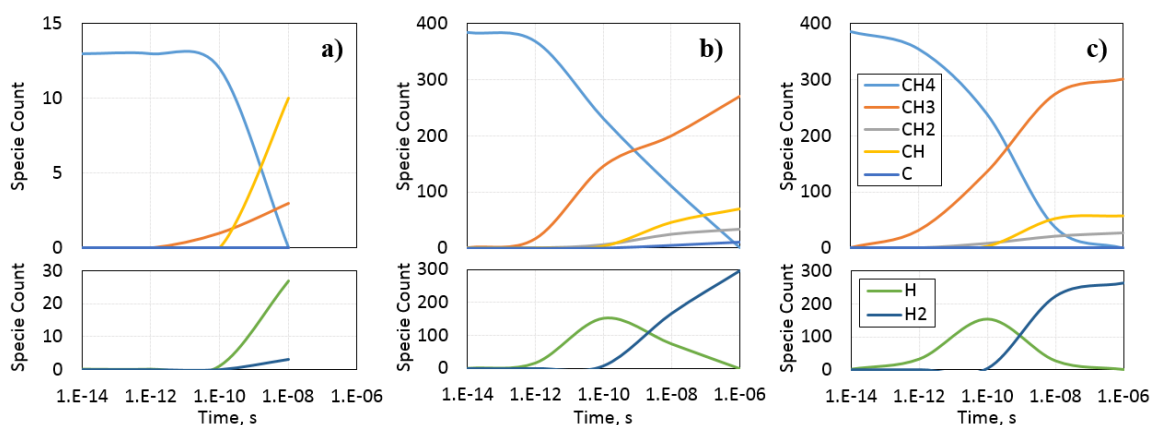


Figure 3.6 Results obtained from KMC of the CH₄ dissociation on Cu (111) at 1200K temperature and a) 0.03 mTorr b) 0.5 Torr c) 1 Torr pressure. Bottom curves correspond to the H and H₂ species of their top figures.

remaining on the surface, re-hydrogenation reactions do not take place and dehydrogenation reactions resume. It can be concluded that higher pressures increase the adsorption of CH_4 and slow down dehydrogenation reactions.

3.4.6.3. Effect of H_2 in the Feedstock Gas

The effect of H_2 was studied by increasing the H_2 molar fraction in the feedstock gas from 0 to 0.5. As seen in **Figure 3.7**, it is clear that with the increase in H_2 in the feedstock gas, dehydrogenation is accelerated and with 0.5 molar fraction of H_2 , C has begun to produce. The hydrogen curves indicate that with 0.5 molar fraction of H_2 , the amount of H species are very low and with the production of CH and C, an increase in H_2 is observed. This indicates the immediate conversion of H to H_2 as H is formed from CH_4 dehydrogenation. With less H species on the surface, re-hydrogenation reactions are impeded and CH_4 dissociation is directed towards CH and C production. In conclusion,

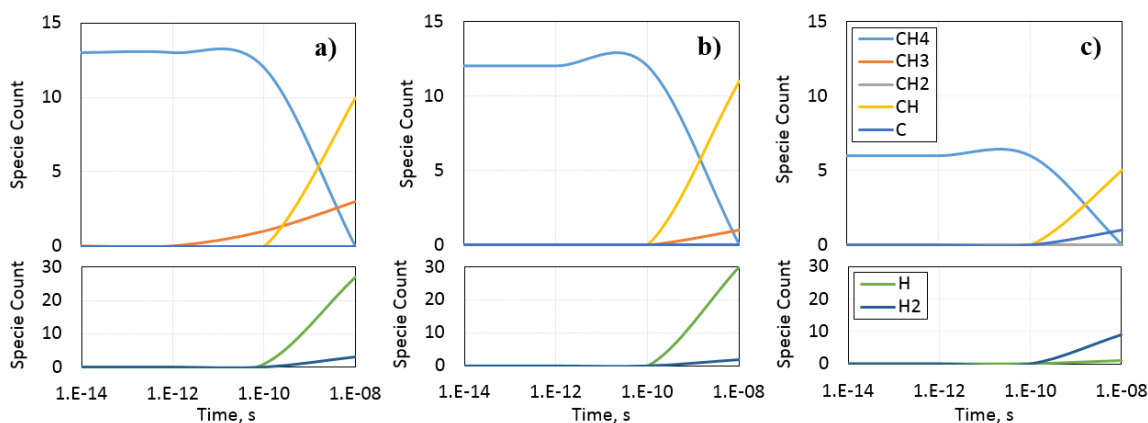


Figure 3.7 Results obtained from KMC of the CH_4 dissociation on Cu (111) at 1200K temperature and 0.03mTorr pressure and a) 0% H_2 b) 10% and c) 50% H_2 molar fraction, in feed. Bottom curves correspond to the H and H_2 species of their top figures.

flowing H₂ along with CH₄ into the reaction chamber in the CCVD method, increases H species on the surface which are very mobile and cause the formation and production of H₂(g) (reaction barrier of 0.93 eV), thereby depleting the surface of H species and impeding re-hydrogenation, but encouraging dehydrogenation, of CH_x species.

3.5. Conclusions

The dissociation of CH₄, a very common C precursor gas in the CCVD growth of graphene and CNT, on the Cu (111) surface was studied by first obtaining all reaction energy barriers and pre-exponential factors from DFT calculations. This data only presents thermodynamic information regarding the dissociation. KMC simulations were then performed to take into account temperature, pressure, diffusion, the kinetics and evolution of the system with time, and also the competing of the pathways. One competing reaction is the dehydrogenation/hydrogenation of H₂/H which is less accounted for in the literature.

The barrier for this reaction is comparable to that of CH_x dehydrogenation/hydrogenation reactions, therefore it must be considered as a competing pathway in the dissociation process. H species are also highly mobile on the Cu (111) surface as deduced from low diffusion barrier found from DFT. The H in the system can either be a result of the dehydrogenation of CH_x species or the in-flow of H₂ along with CH₄ which is a common practice. Experimental studies report that adding H₂ to the in-flow gas facilitates the dissociation of the C precursor gas. These observations are confirmed and explained in this Chapter by a first-principles based kinetic modeling method. The H₂ in the feedstock gas dissociates to H species (low energy barrier of 0.39

eV). These H species along with those of the dehydrogenation of CH₄, diffuse on the surface and form H₂ that is desorbed to the gas phase, thereby depleting the surface of H species that can otherwise re-hydrogenate CH_x species. As such, the reaction pathway is led towards CH_x dehydrogenation reactions. Generally, CH and C species were found to be the most stable and abundant species in the kMC simulations studied here, which confirms reports based on DFT from the literature. Therefore, it seems that CH and C species may well be the building blocks of graphene and CNT growth.

4. HYDROCARBON DECOMPOSITION ON COPPER SURFACES: OXIDATION EFFECTS*

4.1. Summary

DFT and AIMD are used to study the effect of pre-adsorbed O on C adsorption on both (100) and (111) facets of Cu. Results show that on both surfaces, an incoming carbon atom has the ability to replace and completely desorb a previously surface-adsorbed oxygen atom producing CO and CO₂ molecules in the gas phase. By comparison, the (111) surface is better suited for oxygen desorption, and an incoming carbon atom can more easily bond to and desorb oxygen atoms even at low oxygen coverages. The effect of temperature on this mechanism is also examined. An implication of this process is the experimentally proven cleaning effect of pre-dosing copper surfaces with oxygen before graphene growth in the chemical vapor deposition (CVD) process.

Such observations regarding the effect of surface O on atomic C, motivate the investigation of this effect on the C precursor gas, e.g. CH₄, itself. Therefore, DFT calculations are carried out to evaluate energy barriers and mechanisms for the dehydrogenation reactions of CH₄ on oxygen (O) covered surfaces of Cu (111) and Ni (111) with low and moderate O coverages. Results obtained agree with previous findings showing that O promotes CH₄ dissociation on Cu (111) and hinders that on Ni (111). In

* Parts of this chapter are reprinted with permission from Behnaz Rahmani Didar and Perla B. Balbuena. "Adsorption of Carbon on Partially Oxidized Low-Index Cu Surfaces". *Langmuir* 2018, 34(4), 1311-1320. Copyright (2018) American Chemical Society

addition, results show that energy barriers decrease furthermore on Cu with higher O coverages. However, the increase in O coverage did not show any favorable effect for CH₄ dissociation on Ni (111). The findings are explained through some electronic factors such as charge analysis and density of states.

4.2. Introduction

The CCVD is the most widely used method for the synthesis of graphene and single-walled carbon nanotubes (SWCNTs). As the catalytic substrate, Cu has garnered much attention among other transition metals because of its ability to yield high-quality graphene [5]. It is believed that the presence of residual C on the surface of Cu can foster the environment for nucleating graphene. However, too many residual C atoms would lead to a greater number of nucleation sites and subsequently, grain boundaries, which alter the properties of graphene. Reducing the number of grain boundaries in graphene produced on the Cu substrates remains a major challenge [93, 97]. A number of methods [94, 117-122] have been suggested to tackle this issue, one of which is to prepare Cu substrates with as few C residues as possible. To this end, several experimental studies have shown the advantageous effect of pre-dosing O on Cu. Through such experiments, it has been established that the presence of O on the surface of Cu or in the form of copper oxide can “clean” the copper surface of residual carbon, thereby reducing the number of nucleation sites and hence producing much larger graphene domains [121-124]. However, the exact atomistic mechanism by which O atoms are removed from the surface in the presence of C precursor gas has not yet been fully elucidated. Understanding this mechanism and the statistics associated with it can guide us toward

the amounts of oxidation that are sufficient to clean the surface and anticipate products and outcomes of the involved reactions.

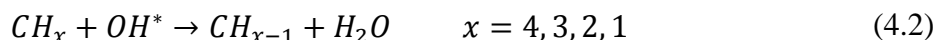
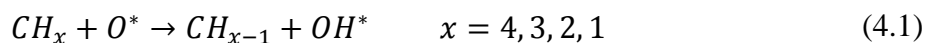
Oxidation of the Cu surface takes place through the adsorption of O₂ molecules and dissociation into two O atoms. It can also happen through dissociation of, for example, a CO₂ molecule on the clean Cu surface. In this chapter, regardless of the source and origin of O atoms, atomic O has been used to oxygenate Cu surfaces. Although, the oxidation of low-index Cu surfaces has been previously studied and described elsewhere [125, 126], this oxidation is revisited here. Currently, graphene growth using the CCVD process is predominantly achieved on copper foils which are polycrystalline [127, 128]. Both single- and multilayered graphene have been successfully produced on many facets of Cu including (100), (111), (110), and (210). However, the (100) and especially (111) facets have shown greater quality of the produced graphene [15]. These two facets have been chosen for this study.

Temperature has a significant effect on the stability of the adsorbed species. To study this effect, AIMD simulations of a C atom adsorbing onto oxygenated Cu surface at elevated temperatures, is also carried out in this chapter. On one hand, this study provides theoretical evidence of the cleaning and purifying effect that oxygen has on a copper surface. However, it also hints at the possibility of inducing termination effects on the growth of carbon nanostructures which would be an important consideration in the SWCNTs synthesis.

Gaining a more complete picture of the effect that O may have on graphene and SWCNT nucleation, requires that in addition to atomic C, the C precursor gas, *e.g.* CH₄,

be studied. The latter part of this chapter studies the effect that O may have on an earlier stage in graphene and SWCNT growth, which is the dissociation of CH₄.

The dissociation of alkanes such as CH₄ as the C precursor gas, entails the activation and breakage of C-H bonds. C-H bond breakage can be achieved at high temperatures. However, in applications where high temperatures are undesirable, other methods such as catalytic methods involving oxidation have become more attractive. Experimental studies [129] and more recently theoretical calculations have elucidated the influence of O* (surface-bound O) and OH* (surface-bound OH) on CH₄ dehydrogenation via the routes:



In this process, electronegative O* and OH* species on transition metals induce and cause the activation of acidic C-H bonds, thereby facilitating C-H bond scission. Theoretical investigations show that the effect of O* and OH* on C-H bonding varies with respect to the transition metal surface to which the alkane is bound [130-134]. For example, O* and OH* on coinage metals (Cu, Ag and Au) promote C-H bond activation, whereas this effect is hindered on Fe, Ni, Pt, Pd. This has been explained by the O–surface binding energy, charge analysis and the chemical nature of O*. O* on certain transition metals such as Cu are found to possess greater negative charges and hence greater electronegativity and basicity that is required to activate acidic C-H bonds. Furthermore, weakly-bound O* on transition metals such as Cu are more capable of activating C-H bonds. Whereas on transition metals such as Ni, O* is strongly bound to

the surface and possesses less basicity. Such insightful theoretical studies have investigated this process at relatively low O coverages of no greater than $\frac{1}{4}$ monolayer (ML) (via $p(2 \times 2)$, $p(3 \times 3)$ and $p(4 \times 4)$ supercells). However, it is reasonable to investigate this effect at higher O coverages where any effect of O may be amplified.

In the latter part of the chapter, the effect of low-coverage pre-adsorbed O and OH species on the dehydrogenation of methane via the aforementioned routes is revisited and the effect thereof at higher O coverage is studied.

4.3. Computational and System Details

DFT calculations were performed using the Vienna Ab initio Simulation Package [58, 109, 110] with the GGA-PBE method for the electron-electron interactions [56] and the PAW pseudopotentials for the electron-ion core interactions [57, 58]. For the first part of the chapter, the two Cu surfaces were constructed in Materials Studio [135] by cleaving along the (100) and (111) planes. To allow the direct comparison, both slabs composed of 64 Cu atoms making up four atomic layers of which the two bottom layers were fixed and the remaining layers were allowed to relax. In this setup, possible adsorption sites for the (100) surface are bridge, hollow, and subsurface interstitial and for the (111) surface are bridge, *fcc*-hollow, *hcp*-hollow, and subsurface interstitial (**Figure 4.1**). The initial structures were allowed to relax. For the adsorption of oxygen atoms, all possible sites were tested. Atoms were added sequentially to all possible sites, and the system was relaxed after each addition. At each addition step where all sites were tested, the most energetically favorable of all was selected and the adsorption energy was calculated. This energy was calculated as the energy variation caused by

bringing an O atom from the gas phase to the surface of the Cu slab per the number of O atoms in the system:

$$E_{ads,O} = \frac{E_{tot} - n_O E_O - E_{Cu_{slab}}}{n_O} \quad (4.3)$$

Here, E_{tot} , E_O , and $E_{Cu_{slab}}$ denote the total energy of the system after relaxation, energy of an O atom in the gas phase, and energy of the pristine Cu slab.

This was followed by the adsorption of a single C atom to each oxygen adsorption step, and the adsorption energy per O atom was calculated as:

$$E_{ads,C} = \frac{E_{tot} - E_C - E_{Cu_{O}}}{n_O} \quad (4.4)$$

where, E_C and $E_{Cu_{O}}$ are the energies of an isolated spin-polarized C atom in vacuum and O-adsorbed Cu slab, respectively. The above definitions of adsorption energy for both cases mean that adsorption is exothermic and stable if the values are negative. To map and

analyze electronic charge density differences using the Bader charge analysis scheme

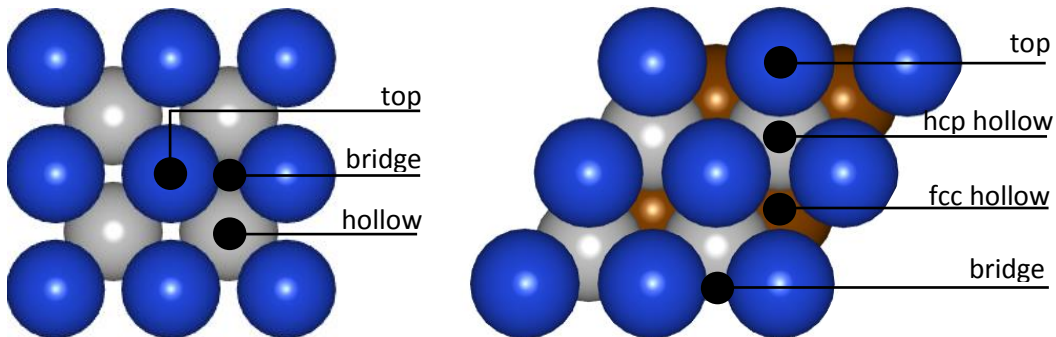


Figure 4.1 Adsorption sites of a) Cu(100) and b) Cu(111) surfaces. Grey and brown atoms are Cu atoms on the 2nd and 3rd layer from top.

[136, 137], the charge density difference for the oxygenated Cu surfaces was defined as:

$$\Delta\rho_{O/Cu} = \rho_t - \rho_{Cu} - \rho_O \quad (4.5)$$

and for the carburized oxygenated Cu surfaces as:

$$\Delta\rho_{C/O/Cu} = \rho_t - \rho_{O/Cu} - \rho_C \quad (4.6)$$

where ρ_t , ρ_{Cu} , ρ_O , $\rho_{O/Cu}$, and ρ_C denote charge densities of the total system, Cu slab, O atom/s, oxygenated Cu surface, and C atom/s, respectively.

For the second part of this chapter, dispersion forces have also been accounted for by using the DFT-D3 correction method of Grimme et al [63]. Both Cu and Ni slabs consisted of $p(4 \times 4)$ supercells of the (111) facet of face-centered cubic crystals (*fcc*) arranged in four atomic layers of which the top two were allowed to fully relax during all calculations. The $p(4 \times 4)$ supercell slab which is chosen here, is large enough to accommodate not only one surface O atom (representing 1/16 ML O coverage) but also 6 surface O atoms which represent 6/16 (=0.38) ML of O coverage, hence allowing direct comparison between low and rather more moderate coverages. It is noted that Cu and Ni undergo surface reconstruction and bulk oxide formation at O coverages of greater than 0.5ML [126, 138, 139].

The minimum energy path for the dehydrogenation reactions of CH₄ on the surfaces were calculated using the climbing-image nudged elastic band (CI-NEB) method [68], reaching convergence when the force normal to the reaction path was less than 0.05eV/Å.

The Bader charge analysis scheme [136, 137] was again used to map and analyze electronic charge density differences defined for the oxygenated Cu and Ni surfaces as:

$$\Delta\rho_{O/M} = \rho_t - \rho_O - \rho_M \quad (4.7)$$

where $\rho_{O/M}$, ρ_t , ρ_O and ρ_M denote charge densities of the oxygenated metal surface, total system, O atoms and the metal surface, respectively.

4.4. Results

4.4.1. Part 1

4.4.1.1. Adsorption of Oxygen onto Cu(100) and Cu(111) Surfaces

The first oxygen atom was added to all possible adsorption sites on both (100) and (111) surfaces. As shown in **Table 4.1**, the resulting adsorption energies showed that the hollow and *fcc*-hollow sites on the (100) and (111) surfaces, respectively, are energetically highly favorable for the adsorption of O. The calculated energies agree well with the literature theoretical and experimental values [140, 141]. Each subsequent oxygen atom was sequentially added into the gas phase and allowed to relax and adsorb onto each Cu surface. At each sequence, all possible adsorption sites were tested. Adsorption energies of the oxygen adsorption sequence are shown in **Figure 4.2**. As deduced from the negative energy values, oxygen adsorption is favorable on both Cu surfaces. The resulting curves of O adsorption energy show that adsorption is stronger on the (100) surface than that on the (111) surface. Thus, the (100) surface is more favorable for the adsorption of O atoms. This is explained by the close-packed lattice structure of the (111) surface that harbors greater repulsion between adsorbed O atoms. The close-packed lattice of the (111) surface results in an increased repulsion among adsorbed O atoms, and this repulsion extends to an incoming adsorbing O atom. The incremental decrease in the energy of adsorption becomes more noticeable from 0.25

Table 4.1 Adsorption sites and energies for adsorption of single O and C atoms on clean Cu (100) and (111) surfaces. Preferred adsorption sites and energies are marked in bold.

	Cu (100)		Cu (111)	
	Site	Eads, eV	Site	Eads, eV
O	top	-2.63	top	-2.43
	bridge	-4.16	bridge	-4.03
	hollow	-5.25	fcc-hollow	-4.45
	interstitial	-	hcp-hollow	-4.20
			interstitial	-3.89
	Site	Eads, eV	Site	Eads, eV
C	top	-2.96	top	-2.89
	bridge	-4.27	bridge	-4.77
	hollow	-6.16	fcc-hollow	-4.85
	interstitial	-	hcp-hollow	-4.82
			interstitial	-5.28

ML coverage onward. On both surfaces, the thermodynamically favorable path of step-by-step O adsorption results in a geometric arrangement among O atoms as can be seen from the top views shown in **Appendix B (Figures B1-B2)**.

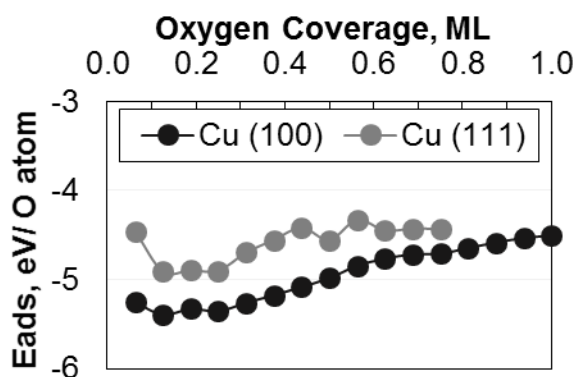


Figure 4.2 Diagram of the O adsorption energy per O atom calculated using DFT (at 0K) for Cu (100) and (111) surfaces. Dashed lines between data points are to aid in visualization.

However, the (100) surface undergoes a major reconstruction induced by O atoms after 0.5 ML O coverage. Surface reconstruction manifests in peaks seen in the curves of **Figure 4.2**. The (111) surface experiences major reconstruction after approximately 0.44 ML coverage (**Figure B2** of **Appendix B**). It can be concluded that consistent with other studies, the (111) surface undergoes oxidation easier than the (100) surface [126]. **Figure 4.2** shows that after approximately 0.56 and 0.44 ML for (100) and (111) surfaces, no significant variation is seen in the O adsorption energies. Other studies observe similar findings and have shown that further oxidation of the Cu surface, if possible, would lead to a major surface reconstruction and formation of a bulk oxide [126, 138].

4.4.1.2. Adsorption of Carbon onto Oxygenated Cu(100) and Cu(111) Surfaces

The effect of oxygen on the adsorption of a single C atom onto Cu surfaces is studied here. First, the adsorption of a C atom was tested for all possible surface and subsurface sites in the absence of any O atoms. On the (100) surface, a hollow site slightly lifted from the surface was found to be the most stable site for C adsorption. On the (111) surface, however, the C atom is most favorably absorbed in the subsurface in an octahedral interstitial site. This is in agreement with the findings of other studies [102, 142]. Values of adsorption energy are listed in **Table 4.1**. By comparison, the C adsorption is more favorable than O adsorption, for both clean surfaces of Cu. Nevertheless, it is assumed that some O atoms have somehow found their way onto the surface, while or before C atoms were adsorbed (e.g., Cu surface is predosed with oxygen). Note that this may occur, for example, during the synthesis of SWCNTs by

CVD processes, where a C-containing precursor is catalyzed and may produce oxygen or oxygen-containing species during or previous to carbon nanostructures growth or from the presence of other additives such as water. Besides, in some cases, the catalyst synthesis takes place simultaneously with the C nanostructure synthesis. In such cases, sometimes oxides of transition metals such as Co, Ni, or Fe are used as precursors of the metal catalyst, where the oxides are reduced by C and are produced by the decomposition of a C-containing species [143, 144]. If such reduction is not complete, partially oxidized surfaces may exist. Results show that the adsorption of the first C atom is more favorable on the (100) surface than on the (111). Then, this procedure was repeated for both Cu surfaces in the presence of an adsorbed O atom. On the (100) surface, the C atom prefers to adsorb onto a hollow site that is farther away from the hollow site preoccupied by an O atom with a weaker adsorption strength compared to the case with no O. On the (111) surface, however, the C atom remains favorable to “absorb” into the interstitial site adjacent to the O occupied *fcc*-hollow site with a stronger adsorption strength compared to the case with no O. The C adsorption on the two Cu surfaces of various O coverages was studied. Images and computational results are shown in **Figures 4.3-4.5**.

As shown in **Figure 4.3**, on the (111) surface, the C atom is no longer stable in an interstitial site but is surface-adsorbed and able to desorb an O atom even at a very low coverage of 0.1 ML and form a C–O bond which is attached to the surface by the C end.

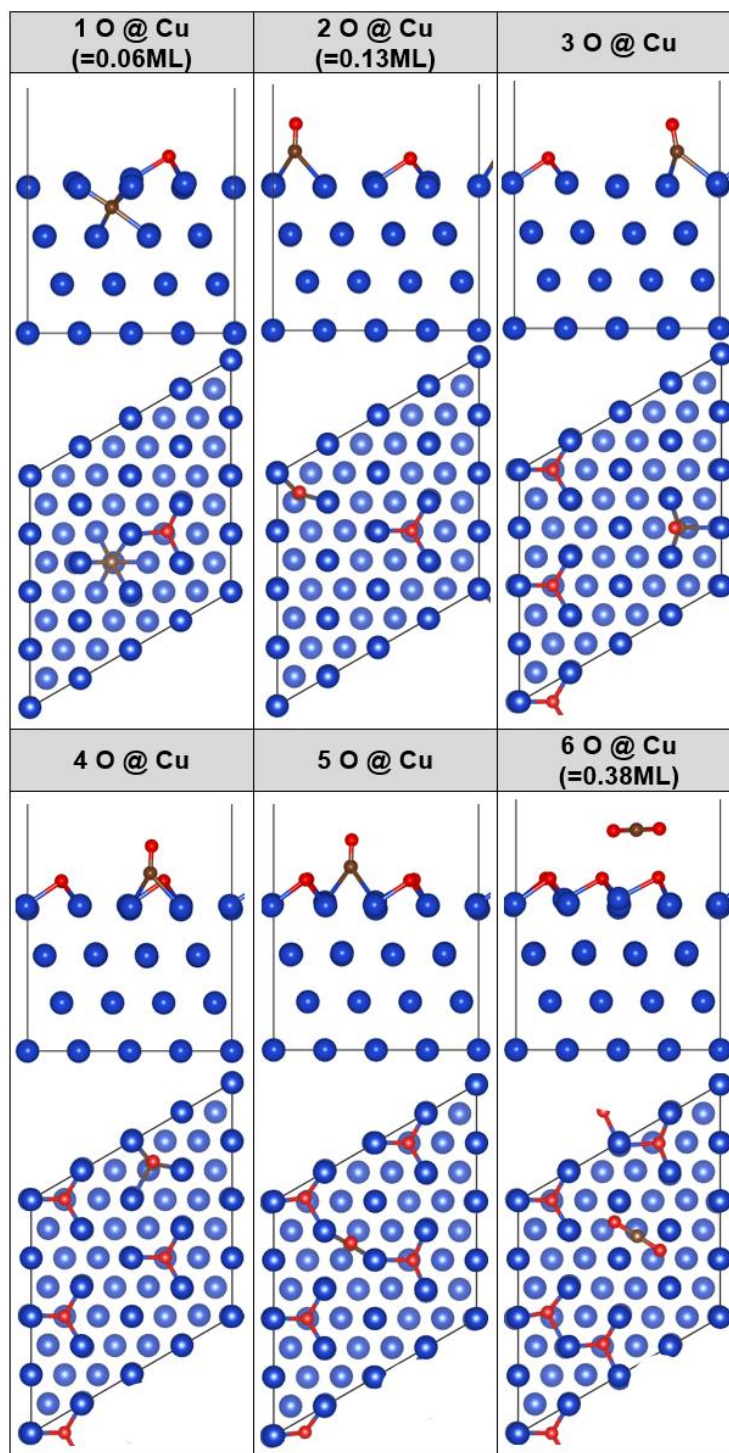


Figure 4.3 Side (upper panels) and top (lower panels) view images of a single C atom adsorbed onto Cu (111) at various O coverages, as a result of DFT relaxation at 0K. Cu, O and C atoms are shown in blue, red and brown, respectively.

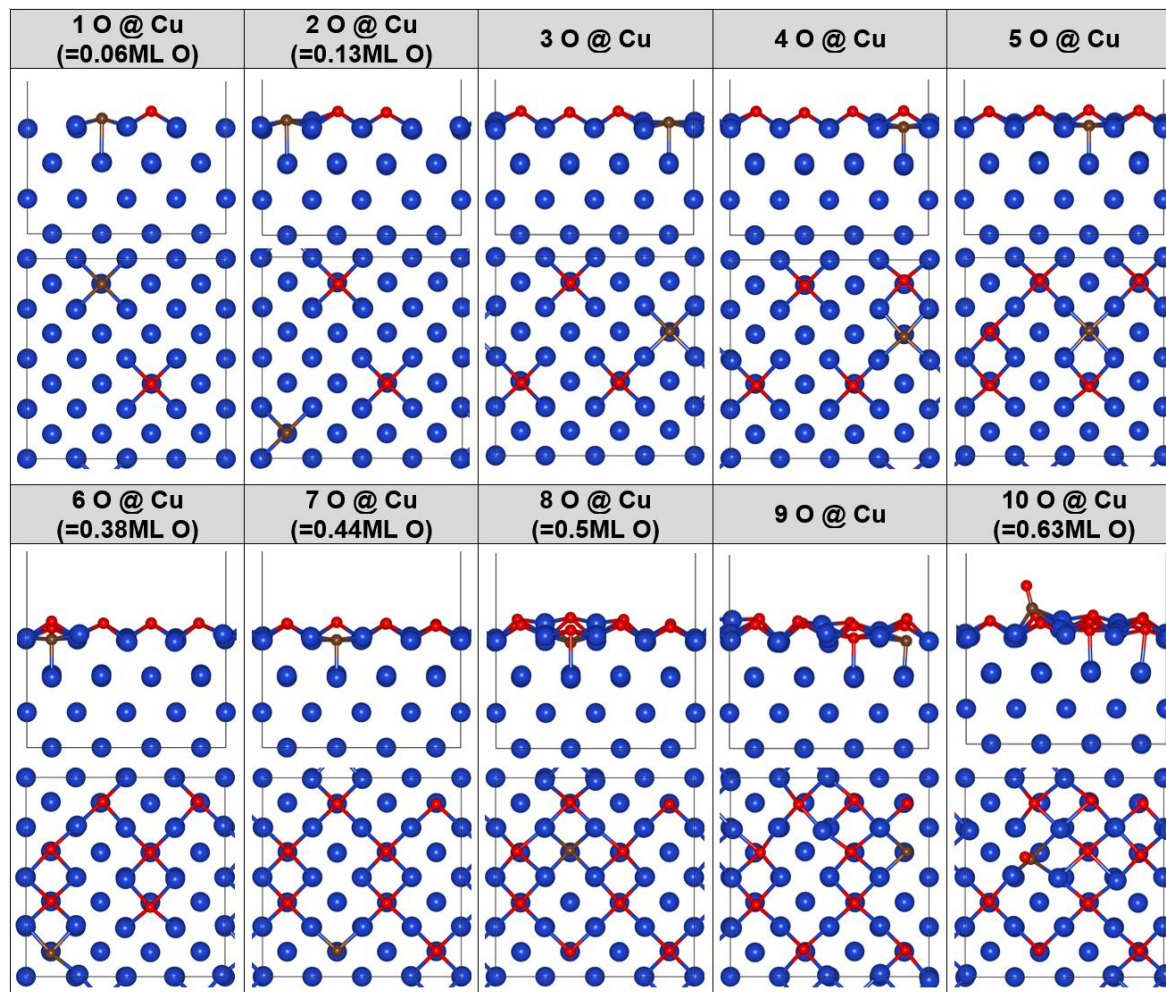


Figure 4.4 Side (upper panels) and top (lower panels) view images of a single C atom adsorbed onto Cu (100) with various O coverage, as a result of DFT relaxation at 0K. Cu, O and C atoms are shown in blue, red and brown, respectively.

This “reductive power” of C occurs for all higher coverages; finally at 0.38 ML, the C atom induces desorption of two O atoms from the Cu surface into the gas phase, consequently bonding to them and forming a CO₂ molecule. However, this is not the case for the more open (100) surface, as shown in **Figure 4.4**. The C atoms on this surface continue to adsorb onto the hollow sites even after noticeable surface reconstruction has occurred. Only at 0.63 ML coverage, the C atom is found to desorb an O atom and form a C–O bond, which is still attached to the surface by the C end. Unlike the (111) surface, the complete desorption of O atom/s into the gas phase was not observed even at 1 ML O coverage for the (100) surface. **Figure 4.5** shows that C adsorption is slightly more favorable on the (111) surface as evident from the more negative adsorption energies. On the same figure, termination points of both curves are defined as the instance where the C atom is able to desorb O atom/s from the Cu surface. As discussed above, this happens at a much lower O coverage for the (111) surface than

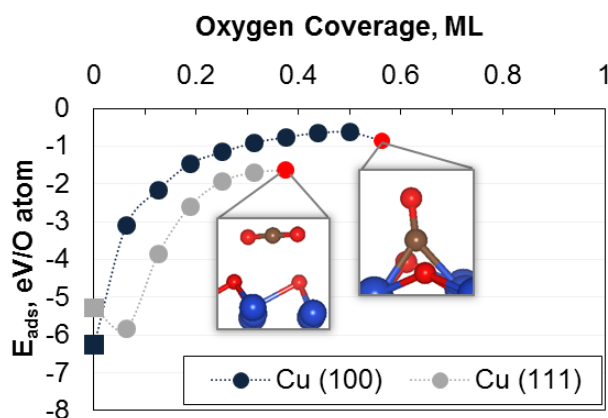


Figure 4.5 C adsorption energy per O atom calculated using DFT for Cu (100) and (111) surfaces. Cu, O and C atoms are shown in blue, red and brown, respectively. Dashed lines between data points are to aid in visualization.

that for the (100) surface. Reduction of the surface by carbon is indirectly shown in **Figure 4.5**, where we observe that the C adsorption energy strength decreases dramatically with O coverage because of the resistance of the oxidized surface to receive a reductive agent. However, the reduction takes place and is manifested in the removal of O from the surface, especially in the (111) surface (**Figure 4.3**). The more open (100) surface offers less resistance to C adsorption but eventually the removal of O also takes place along with the surface reconstruction.

To shed light on the underlying cause of this phenomena, charge density maps were obtained and are presented in **Figure 4.6**. It is apparent that on the (111) surface, neighboring negatively charged regions of O atoms that are shown in blue are close enough to give rise to repulsion between adsorbed O atoms. Whereas, on the (100) surface, these regions are farther apart, and the repulsion is less felt.

4.4.1.3. AIMD Study of C Adsorption onto Oxygenated Cu(100) and Cu(111) Surfaces

To study the effect of temperature on reactivity of C on oxygenated Cu surfaces, each of the Cu(100) and (111) surfaces with 0.5 ML O coverage were taken and a C monomer was added into the gas phase of the computation cell. The addition of a C monomer in the gas phase of the Cu(100) and Cu(111) cells corresponds to pressures of 140 and 200 atm, respectively. These rather high pressure values are due to the small size of the computational cells that have been chosen here. These high pressures are used

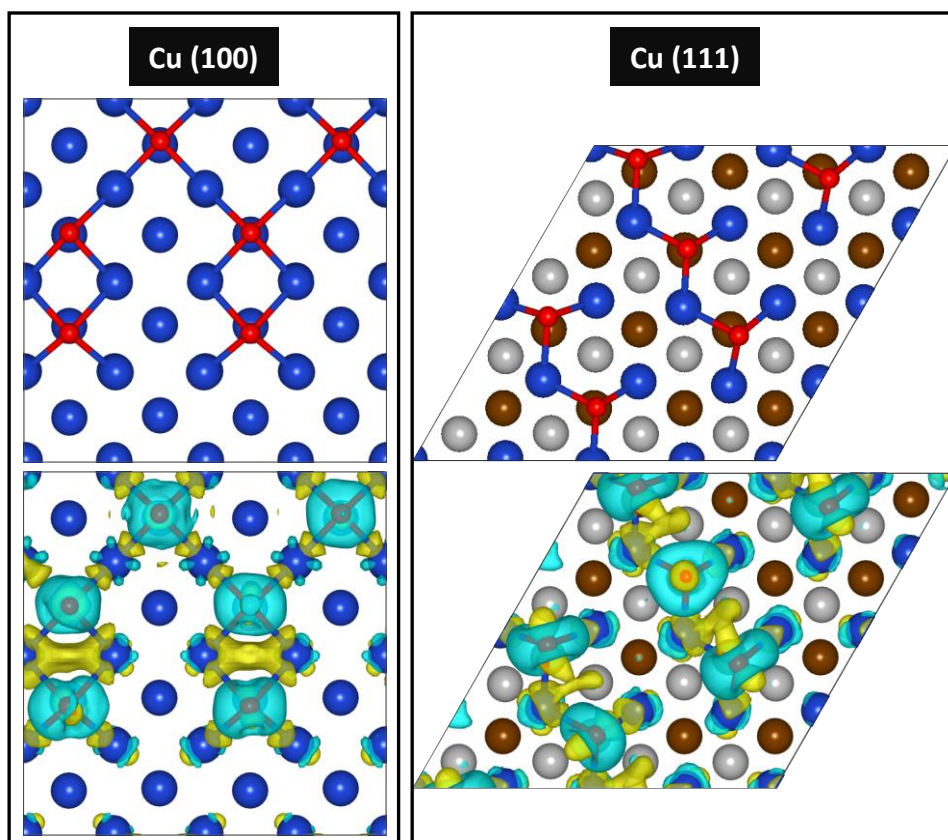


Figure 4.6 Optimized structures (top) and their charge density difference maps (bottom) at 0.38ML O coverage on Cu (100) and Cu (111). Light-blue and yellow clouds represent charge accumulation (negative) and depletion (positive), respectively. O atoms are shown in red, while Cu atoms are shown in blue, grey (2nd layer from top) and brown (3rd layer from top). Grey and brown atoms are also *hcp*-hollow and *fcc*-hollow sites, respectively. The maps are plotted in isosurface level of $0.005 \text{ e}/\text{\AA}^3$.

in some of the CVD synthesis processes of SWCNTs, for example, the HiPCO process [145, 146]. The geometry of both oxygenated surfaces with the C monomer in the gas phase were optimized before performing AIMD simulations. Two temperatures of 1200 and 600 K, were chosen for the investigation.

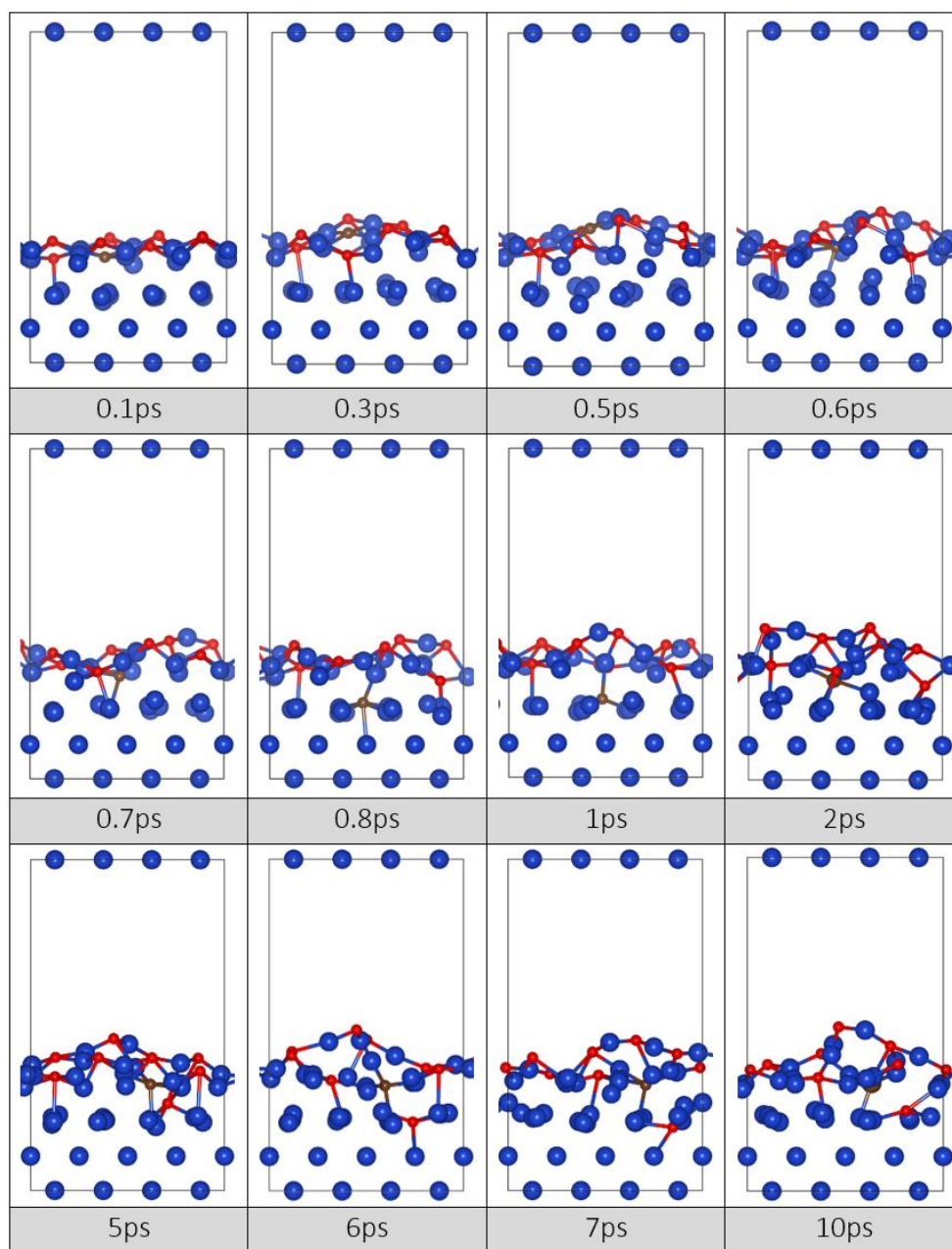


Figure 4.7 Time evolution of adsorbed C (in brown) on Cu (100) with 0.5ML O coverage obtained from AIMD simulations at 1200K temperature.

As stated in the earlier section, on the (100) surface, the C atom initially added to

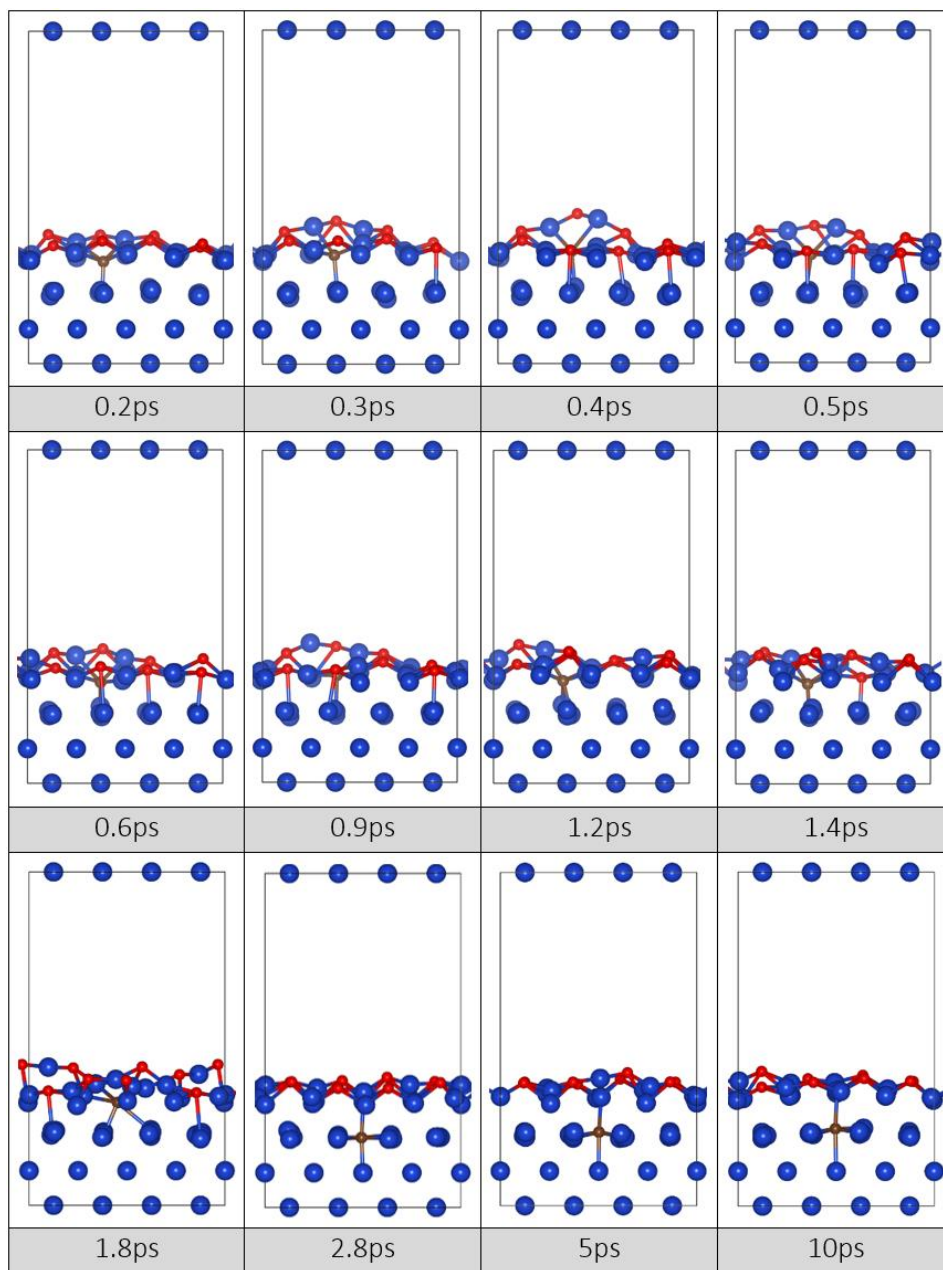


Figure 4.8 Time evolution of adsorbed C (in brown) on Cu (100) with 0.5ML O coverage obtained from AIMD simulations at 600K.

the gas phase relaxed and adsorbed into a hollow site (**Figure 4.4**). AIMD results obtained for the (100) surface showed that at a high temperature of 1200 K (**Figure 4.7**),

a major surface reconstruction occurs at the surface, and the C atom initially adsorbed onto the surface is lifted along with the O atoms on the surface and pushed back into the surface and then deeper into the subsurface. At a lower temperature of 600 K (**Figure 4.8**), the surface reconstruction is much less, and the C atom hovers at roughly around the location where it first relaxed onto. In addition, our simulations of up to 10 ps showed that the adsorbed C was unable to break away from the surface or bond to any O atom. This provides an idea of the amount of energy needed for these processes to occur.

Results obtained for the Cu(111) surface showed a somewhat different picture. Initially, the C atom in the gas phase relaxed onto the Cu surface by desorbing a surface-bound O atom, bonding to the surface Cu on one side and that desorbed O atom on another.

At 1200 K (**Figure 4.9**), the C atom bonded to O was able to eventually (roughly 0.5 ps later) desorb from the surface and enter the gas phase as a CO molecule. This was not possible at the lower temperature (**Figure 4.10**), at least for the 10 ps time interval that was studied. Note that the surface reconstruction on the (111) surface is major and greater than that on the (100) surface for all three temperatures.

Both DFT and AIMD results show that the (111) surface better facilitates desorption of oxygen by carbon through CO or CO₂ bond formation. In the next part of the chapter, the effect of pre-adsorbed oxygen on the dissociation of CH₄ to atomic C is studied. Cu (111) is taken as the metal surface, however for a comparison, Ni (111) is also studied.

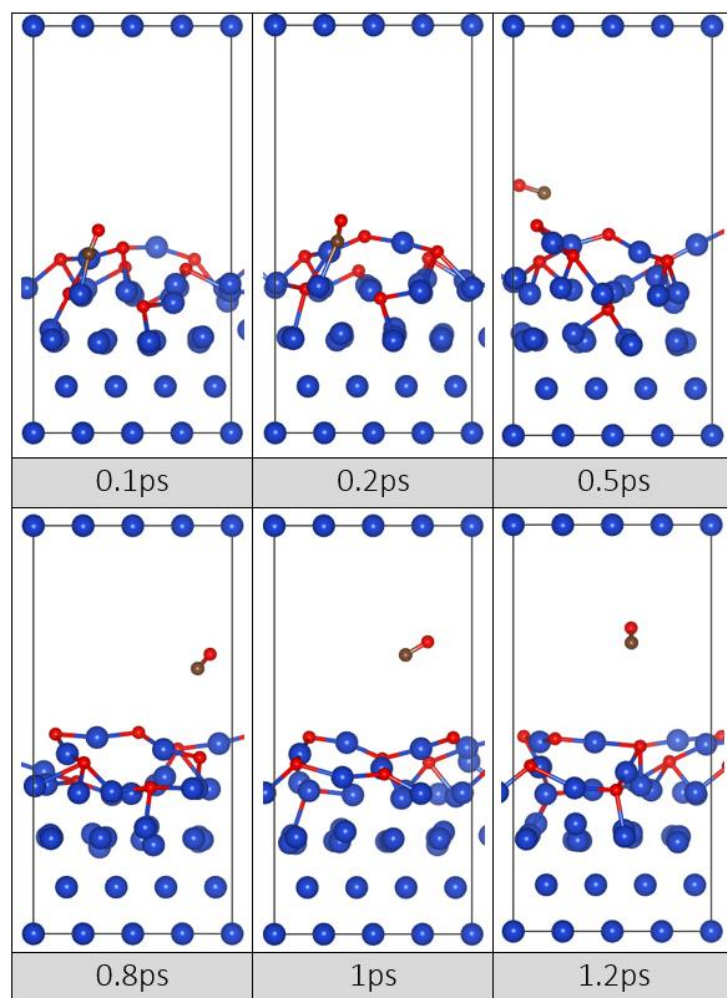


Figure 4.9 Time evolution of adsorbed C on Cu (111) with 0.5ML O coverage obtained from AIMD simulations at 1200K temperature.

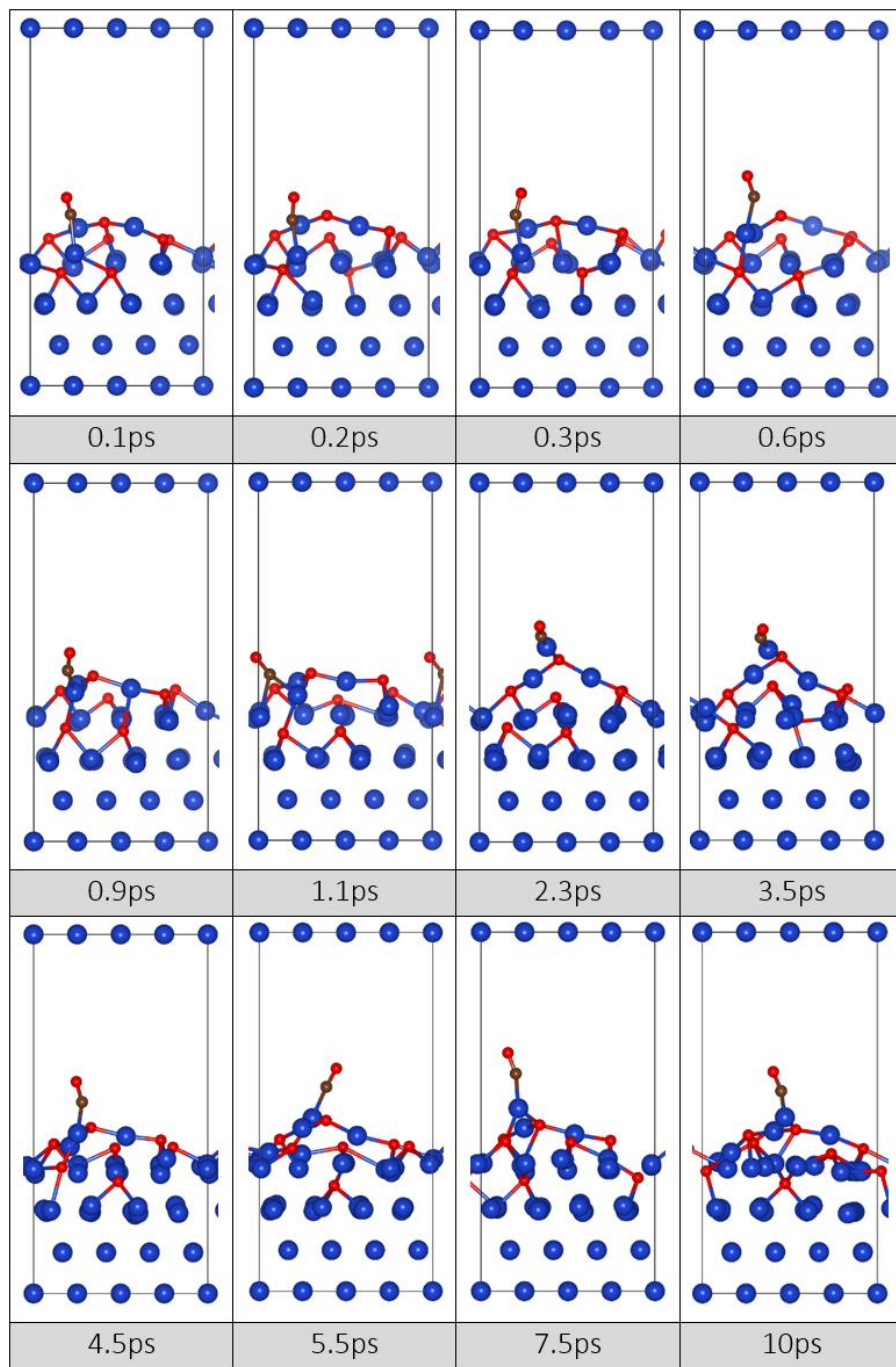


Figure 4.10 Time evolution of adsorbed C on Cu (111) with 0.5ML O coverage obtained from AIMD simulations at 600K temperature.

4.4.2. Part 2

4.4.2.1. CH₄ Dehydrogenation on Clean Cu (111) and Ni (111) Surfaces

The NEB calculations for obtaining transition states and energy barriers of reactions require initial (reactant) and final (product) state of those reactions. DFT calculations were performed for both surfaces to find the most favorable adsorption (for initial state) and co-adsorption (for final state) of all possible species (CH₃^{*}, CH₂^{*}, CH^{*}, C^{*}, CH₃^{*}+H^{*}, CH₂^{*}+H^{*}, CH^{*}+H^{*}, C^{*}+H^{*}) involved in the dehydrogenation process. The results of these calculations form the initial and final states of reactions for the NEB calculations. Thus, the energy profile for the sequential dehydrogenation (CH₄ → CH₃ → CH₂ → CH → C) of free CH₄ to adsorbed C was constructed from the NEB calculations. Initial, transition and final states of the reactions involved are shown in the **Appendix B (Figure B3-B4)**. The energy profiles for Cu (111) and Ni (111) can be seen

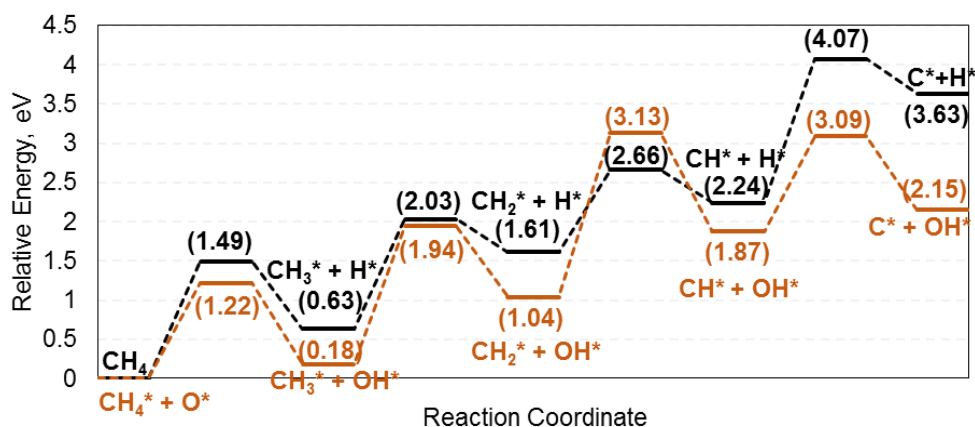


Figure 4.11 Energy profile for CH₄ dehydrogenation on clean (black) and 1/16 ML Oxygen covered (orange) Cu (111) surfaces. The numbers in parenthesis at the maxima are the energy barriers for each step, and the values at the minima are the reaction energies.

in **Figures 4.11** and **4.12** and serve as benchmarks for the remainder of the study of the two metal surfaces with pre-adsorbed O. Energy barriers for both Cu (111) and Ni (111) agree well with the literature [84, 85]. Energy barriers for CH₄ dissociation on Ni (111) are remarkably lower than those on Cu (111). As in Cu (111), the energy barrier for CH dehydrogenation on Ni (111) is the highest among other barriers.

4.4.2.2. CH₄ Dehydrogenation on Cu (111) and Ni (111) with 1/16ML O Coverage

For the case of metal surfaces with pre-adsorbed O, first the adsorption of atomic O on the Cu (111) and Ni (111) surfaces was examined. For the surface of *p*(4x4), the adsorption of only one atomic O leads to a coverage of 1/16 ML. The 1/16ML O covered Cu and Ni (111) surfaces were prepared by testing all possible sites for the adsorption of O on both metals and choosing the most thermodynamically favorable site. The most favorable adsorption site of O for both surfaces was found to be the *fcc* site. This is confirmed in the first part of this chapter. The adsorption energy of an atomic O on Cu

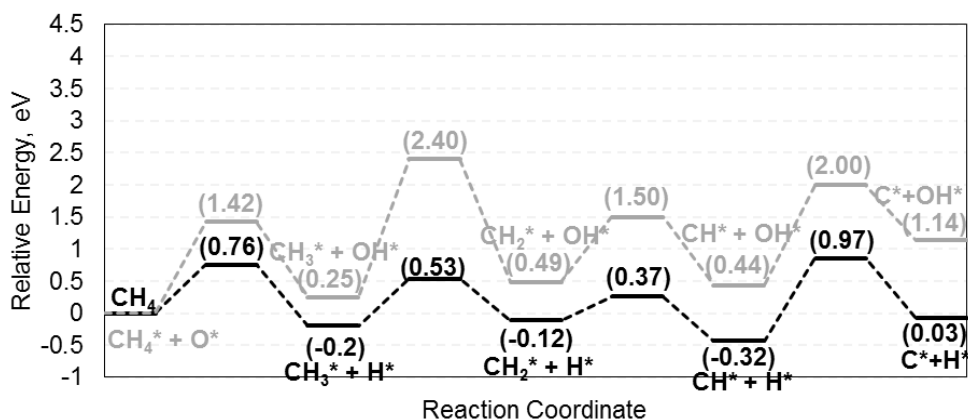


Figure 4.12 Energy profile for CH₄ dehydrogenation on clean (black) and 1/16 ML Oxygen covered (grey) Ni (111) surfaces.

(111) is weaker than on Ni (111). Bader charge analysis was performed to investigate the charge of the O atom on both the surfaces. The charge of O on Cu (111) is more negative than on Ni (111) (reported in **Table 4.2**), which indicates a higher electron transfer from the surface to the adsorbed O atom on the Cu surface. After preparing the O-adsorbed Cu and Ni (111) surfaces, the same procedure discussed for clean surfaces was carried out to find the initial/final states of each reaction step.

Here, the co-adsorbed species are CH_4+O^* , CH_3^*+O^* , CH_2^*+O^* , CH^*+O^* , $\text{CH}_3^*+\text{OH}^*$, $\text{CH}_2^*+\text{OH}^*$, CH^*+OH^* and C^*+OH^* . NEB calculations were then performed to find the energy barriers of **reaction 4.1**. Initial, transition and final states of the reactions involved are shown in **Appendix B (Figures B5-B6)**. Energy profiles depicting the energy barriers for all four dehydrogenation steps of CH_4 on 1/16 ML O covered Cu (111) and Ni (111) alongside clean surfaces are shown in **Figures 4.11 and 4.12**, respectively. The figures clearly show that the presence of O on Cu (111) reduces energy barriers for dehydrogenation and therefore promotes CH_4 dehydrogenation. On Ni (111) however, dehydrogenation energy barriers are increased in the presence of O.

Table 4.2 Adsorption energies and electronic charge of 1 and 6 O atoms on Cu (111) and Ni (111) surfaces, referring to 1/16 and 6/16 ML O coverages.

	1 O*			6 O*		
	Site	$E_{\text{M-O}}$ eV/O	Charge e	Site	$E_{\text{M-O}}$ eV/O	Charge e
Cu (111)	<u>fcc</u>	-4.60	-0.91	<u>fcc</u>	-4.37	-0.85(avg)
Ni (111)	<u>fcc</u>	-5.52	-0.82	<u>fcc</u>	-5.24	-0.77(avg)

The inhibiting role of O on CH₄ dehydrogenation on metals such as Ni has been attributed to the blocking of surface sites available for adsorption by strongly bound O atoms [147, 148]. In addition, the dehydrogenation of CH_x involves the breaking away of H in a C-H bond and its adsorption to a pre-adsorbed O atom, thereby forming an OH* group. This adsorption on a 1/16 ML O covered Cu (111) and Ni (111) is calculated as -3.19eV and -2.7eV, respectively. Therefore, OH* is more strongly bound to and stable on the Cu (111) surface. The strong binding of the OH* group to Cu surface may imply the facilitated breaking of C-H bonds. As such, the effect of OH* on CH₄ dissociation (via **reaction 4.2**) was also studied at the same coverage of 1/16 ML. The energy profiles and configurations are depicted in **Appendix B (Figures B7-B8)**. Compared to O*, OH* appears to have an even greater promoting effect on CH₄ dissociation on Cu surfaces, while the opposite effect is observed in Ni (111) surfaces.

4.4.2.3. CH₄ Dehydrogenation on Cu (111) and Ni (111) with 6/16ML O Coverage

For the chosen surface of $p(4 \times 4)$, the adsorption of six atomic O would lead to a higher coverage of 6/16 ML. On both Cu and Ni (111), these six O atoms were adsorbed one O atom at a time, optimizing the structures and finding the most favorable adsorption site at each O adsorption step, *i.e.* at each adsorption step all possible sites were tested and the most favorable site was chosen to proceed with. The arrangement of the 6 O atoms on Cu and Ni are equivalent (as seen in **Figure 4.13c,d**). As with 1 O atom, the binding energy of 6 O atoms onto Cu (111) is weaker than on Ni (111) (seen in **Table 4.2**) and therefore surface O atoms are weakly bound and more active on Cu (111) than on Ni (111).

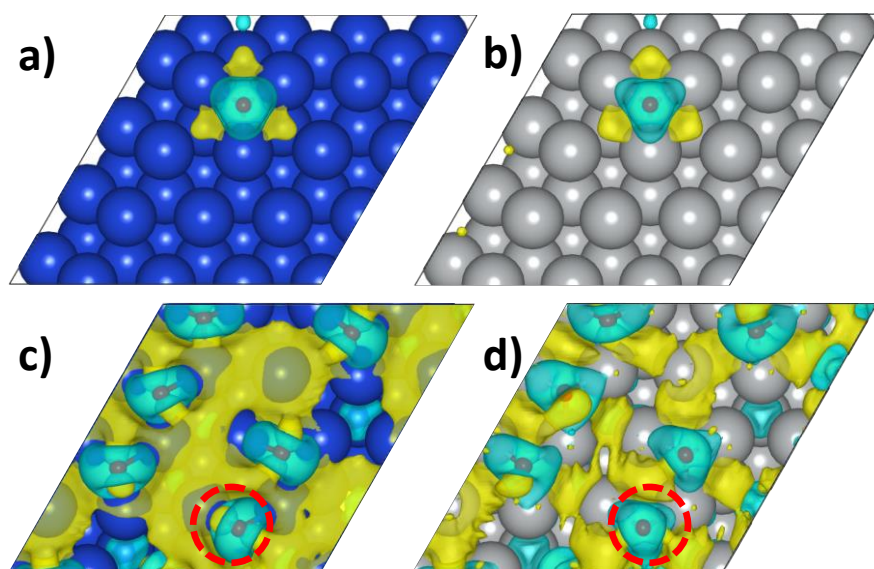


Figure 4.13 Charge density difference maps of a) 1 O* on Cu (111) b) 1 O* on Ni (111) c) 6 O* on Cu (111) and d) 6 O* on Ni (111). Yellow and blue colors represent areas with charge depletion (positive) and accumulation (negative), respectively. (Isosurface level = $0.002 e/\text{\AA}^3$)

Bader charge analysis shows that the charges of O atoms on the Cu (111) and Ni (111) surfaces average at $-0.85|e|$ and $-0.77|e|$, respectively. Hence, the six O atoms on Cu (111) are more electronegative than on Ni (111). **Figure 4.13** depicts the charge density difference maps of the 1 and 6 pre-adsorbed O atoms on Cu (111) and Ni (111). For the higher O coverage (6 O atoms), Cu (111) shows greater areas of charge transfer compared to Ni (111). The production of OH* is an important aspect to consider in our evaluation of reaction (1) on Cu and Ni as it forms part of the final state and it can be bonded to any of the 6 O atoms pre-adsorbed on the surface. Also shown in **Figures 4.13c** and **4.13d** are the red circles which designate the most favorable adsorption site for H to bond to O* and form OH*. As with 1/16 ML O coverage, this adsorption is considerably more favorable on the 6/16 ML O covered Cu (111) (-3.53eV/O atom) than

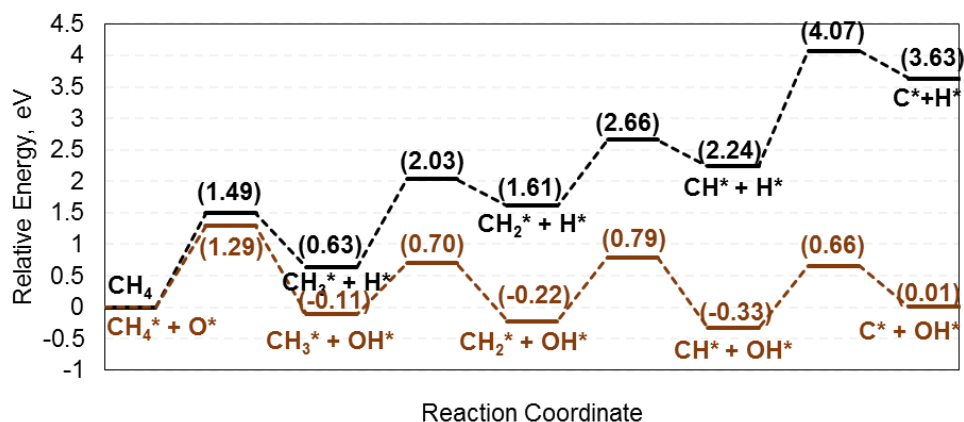


Figure 4.14 Energy profile for CH₄ dehydrogenation on clean (black) and 6/16 ML Oxygen covered (brown) Cu (111) surfaces.

on its Ni (111) counterpart (-2.89eV/O atom). The same procedure discussed in the previous sections was carried out to find initial and final states of **reaction 4.1** for the new coverage. Initial, transition and final states of the reactions involved are shown in **Appendix B (Figures B9-B10)**. CI-NEB calculations were then performed to obtain

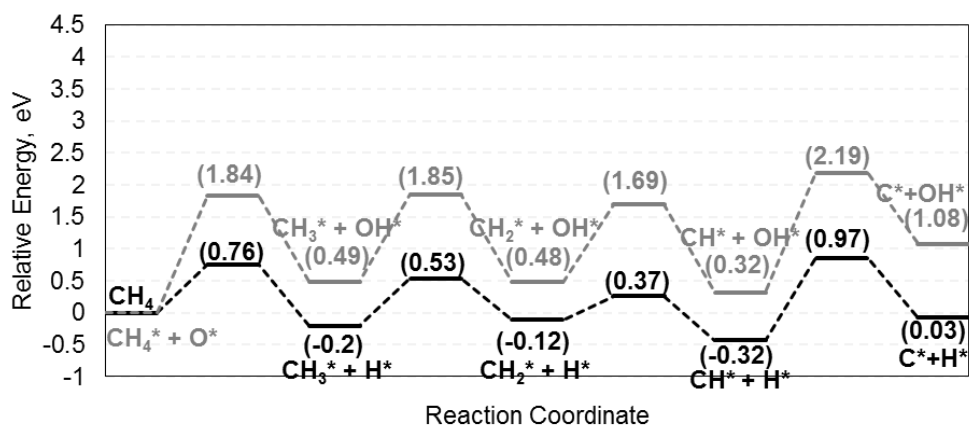


Figure 4.15 Energy profile for CH₄ dehydrogenation on clean (black) and 6/16 ML Oxygen covered (dark grey) Ni (111) surfaces.

energy barriers for each reaction step. Energy profiles depicting the energy barriers for all four dehydrogenation steps of CH₄ on 6/16 ML O covered Cu (111) and Ni (111) alongside clean surfaces are shown in **Figures 4.14** and **4.15**, respectively. **Figure 4.14** shows significant decrease in energy barriers for all dehydrogenation steps on 6/16 ML O covered Cu (111). Furthermore, dehydrogenation on 6/16ML O covered Cu (111) becomes slightly exothermic. The energy barriers for 6/16ML O coverage on Ni (111) slightly increase with respect to its 1/16 ML O coverage.

4.4.2.4. Electronic Factors

The reactivity of a metal surface can be defined by the distribution of its electronic states in the valence band [149]. In this work, we analyze the reactivity differences between Cu (111) and Ni (111) can be analyzed through their density of states (DOS).

Due to the presence of fully and partially filled localized 3d orbitals and the resulting repulsion among d orbital electrons on both metal surfaces, we have used the DFT+U method to plot the DOS. The DFT+U method incorporates additional energy factors for delocalization of the d orbitals. The formalism of Dudarev et al [66] with U-J values of 7 eV [150] and 6 eV [151] were used for Cu and Ni, respectively.

First, a discussion of clean and O adsorbed Cu and Ni surfaces is in order. **Figure 4.16** shows the DOS projected onto the d-orbitals of the clean and O adsorbed surfaces of Cu and Ni. For Ni, the d-band lies well on the Fermi level energy for its clean and O adsorbed surfaces, whereas this is not the case for Cu. Nonetheless for Cu, the d-band is not entirely empty at the Fermi level. However, the main focus of these plots is the d-

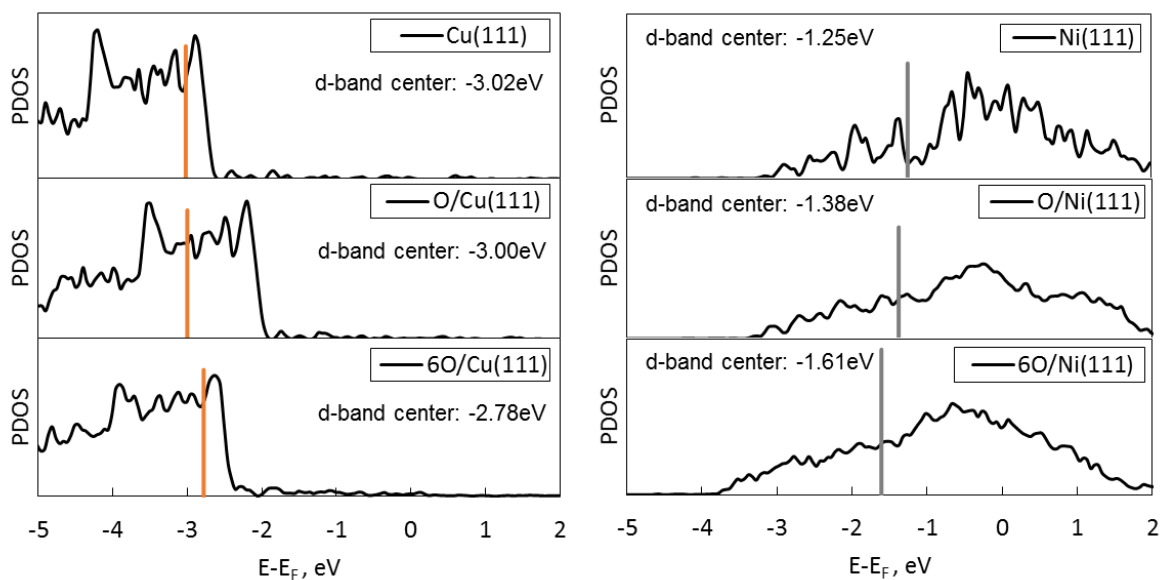


Figure 4.16 Projected density of states (PDOS) onto the d-orbitals of the metal atoms in clean, 1/16 ML and 6/16 ML O pre-adsorbed Cu (left) and Ni (right) surfaces. The vertical lines indicate d-band centers.

band center shift with the adsorption of O atoms. The closer the d-band center is to the Fermi level, the higher is the reactivity. For Cu, the d-band center shifts towards the Fermi level – from -3.02 eV on clean to -3.00 eV on 1/16 O ML and to -2.78 eV on 6/16 O ML – indicating the increase in reactivity of the surface with the increased adsorption of O. Whereas for Ni, the d-band center shifts away from the Fermi level with the addition of O to its surface (from -1.25 eV on clean to -1.38 eV on 1/16 O ML and to -1.61 eV on 6/16 O ML).

This is consistent with the decrease seen in energy barriers for CH dissociation on Cu and the increase seen thereof on Ni.

To obtain insight into the effect of O on the reactivity of the metal surfaces towards CH adsorption, the DOS projected onto the CH₃ molecule as in the final state of

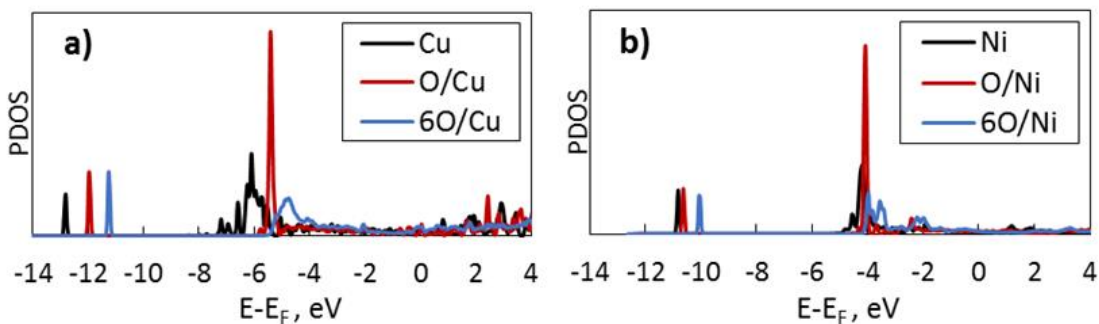


Figure 4.17 PDOS onto CH_3 molecules in the final state on clean and 1/16 ML and 6/16 ML O pre-adsorbed Cu (left) and Ni (right) surfaces.

reaction (1), were calculated. It is noted that since CH_4 adsorption onto both metal surfaces is very weak, the reactivity change of surfaces towards its adsorption is also weak and unobservable on PDOS. Therefore, the study of CH_3 was chosen. As shown in **Figure 4.17**, the HOMO peak of the CH_3 molecule gradually shifts towards the Fermi level with the adsorption of more O on Cu. This is less of a case for Ni. These observations are also consistent with the decrease seen in energy barriers for CH dissociation on Cu but the increase seen thereof on Ni.

Both **Figures 4.16** and **4.17** indicate difference in properties of the two surfaces in the presence of oxygen and explain the facilitating effect of surface O on CH_4 dissociation path on Cu (111), and hindrance thereof on Ni (111).

4.5. Conclusions

Adsorption of C onto the oxygenated (100) and (111) surfaces shows some differences which can be attributed to the lattice structure and charge distribution. Results show that on the more open (100) surface, C atoms tend to adsorb deeper into the subsurface, whereas on the (111) surface, C atoms adsorb on the surface. Also

because of its more open structure, higher O coverage is required for a C atom acting as a reducing agent to desorb an O atom from the (100) surface compared to the (111) surface.

In AIMD simulations which were used to evaluate the dynamic and temperature-dependent nature of adsorption, both surfaces showed a distinctive behavior with respect to the effect of O on adsorbed C. On the (111) surface, the C atom is able to desorb an O atom and enter into the gas phase as a CO molecule.

This study shows evidence of the cleaning effect of oxygen on Cu surfaces in the presence of carbon with applications to graphene synthesis. These results can also be extrapolated to nanoparticle surfaces used in the synthesis of carbon nanotubes. It can be speculated that partially oxidized facets may exist on the nanoparticle catalyst because of the dissociation of oxygen containing gases (e.g., H₂O or an oxygenated precursor gas) in the CVD chamber; may bond to C atoms later on, after being exposed to carbon-containing precursor gases (e.g., C₂H₂); and may form CO and CO₂ molecules in the gas phase. In this case, the surface of the nanoparticle catalyst being cleaned of any residual oxygen can then foster the environment for carbon surface and bulk diffusion before CNT nucleation and growth. On the other hand, if the precursor gas is itself an oxygen containing gas (e.g., CH₃OH), then the oxygen atoms desorbed to the gas phase by bonding to carbon are likely to be constantly replaced by other oxygen atoms dissociated from the precursor gas, so long as the synthesis process is allowed, thereby moderating the rate of carbon nanostructures growth, but also hindering dissociation and surface diffusion of carbon atoms necessary for the CNT nucleation and growth. Such

desorption of carbon as CO or CO₂ in partially or totally oxygenated surfaces may be one of the reasons for the termination of CNT growth.

A more complete study is one in which rather than atomic C, a C precursor gas provides C atoms for graphene growth. Therefore, the effect of pre-adsorbed O on the adsorption and dissociation path of CH₄ on Cu (111) and Ni (111) surfaces was also investigated. This dissociation exhibits high energy barriers on clean Cu (111) and lower less energy barriers on clean Ni (111). However the presence of surface O significantly changes the behavior of these surfaces; promoting the dissociation on Cu (111) and inhibiting that on Ni (111). This behavior persists at higher O coverage of these surfaces. Charge analysis shows higher electronegativity and therefore basicity of O atoms on Cu (111) surface than on Ni (111) which induces the activation of acidic C-H bonds. PDOS plots show that the surface O increases the reactivity of the Cu (111) surface, while reducing that of Ni (111). Such plots also reveal that HOMO peaks of CH₃ shifts closer to Fermi level on Cu (111), and farther away from it on Ni (111). This information indicates the activation of the C-H bond by O on Cu (111) and the inhibition thereof on Ni (111).

Overall, compared to clean Cu, surface oxygenated Cu greatly facilitates the C precursor gas dissociation to atomic C. However, in the presence of further surface O, atomic C can bond to O and form CO or CO₂ and desorb from the catalyst surface. Therefore, for Cu as the catalyst, oxygenating its surface prior to growth but maintaining an anoxic environment during growth may well be the best approach for graphene and CNT growth.

5. CARBON STRUCTURES NUCLEATION AND GROWTH*

5.1. Summary

Repeated thermal cycling by using an organic precursor has shown to be a successful technique for growing graphene on metal substrates. Having control on this process is of vital importance in producing large areas of high quality graphene with well-ordered surface characteristics, which leads to the investigation of the effect of temperature on the microscopic mechanisms behind this process. Apart from being an important factor in the dissociation of the organic precursor and promoting the reactions taking place on the surface of the catalyst, temperature also plays a major role in the structure of the catalyst surface. In the experimental part of this chapter, conducted by Prof. Homa Khosravian at Texas A&M University, eight thermal cycles to successfully grow graphene on the surface of Cu (111) were used. Then, AIMD simulations were employed to study graphene island alignment evolution at two temperatures. The results shed light on experimental observations and those reported in the literature of the effectiveness of controlled thermal cycling in producing high quality graphene sheets on transition metal catalyst surfaces.

5.2. Introduction

Ni, Ir and Cu are three of the most common transition metals that are used as catalyst substrate for graphene growth [6]. Growth mechanism on these substrates are

* Reprinted with permission from Behnaz Rahmani Didar, Homa Khosravian and Perla B. Balbuena. "Temperature effect on the nucleation of graphene on Cu (111)". RSC Advances 2018, 8, 27825-27831 – Published by The Royal Society of Chemistry

shown to be highly dependent on temperature [152]. Among these substrates, copper has become one of the most widely used catalysts for the synthesis of graphene using the CVD method. Large high-quality graphene films were grown on copper, which exhibit transferability and unique plasmonic characteristics [5, 153, 154]. Low carbon solubility [155, 156] and weak Cu–C interactions [157, 158] along with low surface diffusion energy barrier of C atoms on Cu [159] all contribute to surface-driven mechanisms present in the nucleation and growth of graphene domains [5, 15, 160]. These factors may also explain why Cu produces predominantly single layer graphene [5, 161]. Low surface diffusion energy barrier contributes to highly mobilized carbon atoms that can travel freely on the Cu surface and attach to existing graphene islands. Surface Cu atoms have high mobility at high temperatures which can facilitate the mobility of C atoms and graphene islands at such temperatures and lead to defect healing [160, 161]. Therefore, surface morphology of Cu substrate at elevated growth temperatures is an important issue.

Reported research aimed at improving the quality of graphene grown over Cu surface have focused on several aspects of this process. As an example, Wassei *et al.* investigated how the type of organic precursor may affect graphene growth and dictate its structure [162]. In other studies, environmental conditions such as temperature, pressure and hydrogen that may have effect on graphene growth were investigated [152, 163, 164]. The copper catalyst surface has also been subject to many studies as the surface plays a major role in the epitaxial graphene growth and achieving a perfectly clean surface prior to growth is highly desirable [102, 121, 122, 165]. Yu *et al.* reported

their simple approach of preparing the copper surface by growing it on single-crystal sapphire. The resulting copper layer is reported to be extremely flat, chemically clean and can be easily peeled off to use for graphene growth. The graphene grown on such a copper surface exhibited very large domain sizes [166].

High resolution electron microscopy provides valuable insights into Moiré patterns, defects and domain (grain) boundaries in graphene produced from the CVD method. Moiré patterns are regular patterns that result from overlaying two regular lattices one on top of another [167]. Lattice parameters and the angle at which the two lattices overlay, give rise to various periodicities and patterns which are always observable in epitaxial graphene growth. Domain boundaries have been subject to intense studies and may hold the key to understanding the growth mechanism. In this regard, two main mechanisms have been proposed for the growth of graphene on transition metal surfaces: segregation growth (Ni, Ru, Ir), and surface growth (Cu) [5, 15]. In the surface-driven mechanism of growth on copper, it is shown that graphene islands grow when temperature is high enough to facilitate the diffusion of islands. At such temperatures some islands may ‘stitch’ together to form larger graphene domains [80, 97, 168-170]. Consequently, the overarching hypothesis is that defects observed in the graphene overlayer arise from the misalignment of graphene islands constituting a domain; various islands nucleate and grow with different rotational alignments across the catalytic substrate. Several studies have been aimed at investigating what dictates these island orientations. Studies in this area have concluded that domain shapes and sizes themselves are controlled by growth conditions such as temperature [119, 171].

Upon closer examination, two possible routes have been identified that would lead to the transition of islands to domains; either the islands migrate and coalesce into larger islands, or islands progressively grow in size and form domains through addition of C atoms [142, 170, 172]. In the former, with the foregoing discussion, temperature would have great influence on rotation and migration of islands and domain growth, as well as on nucleation density, as evidenced earlier [171, 173]. While in the latter case, surface diffusion of C adatoms would be most likely to have a greater impact on growth of domains. Thus, the identification of the prevailing case will help in optimizing growth parameters. Although this may be a challenge since many factors are involved in the competition including carbon source gas decomposition rate, nucleation rate, surface diffusion and growth rate from carbon adatom addition.

The main interest of this chapter is to understand the role of nucleation and growth parameters, such as temperature, on graphene domain orientation. In this regard, the catalyst surface may have a more active role than thought in the determination of domain boundaries. Experimental and *ab initio* methods are employed in this investigation to understand how temperature and time cycles (annealing and source gas exposure cycles) may affect the alignment between the Cu lattice and a pre-existing graphene fragment. The focus is to study the interplay of the Cu substrate and the graphene overlayer in conjunction with temperature at early stages of growth.

5.3. Experimental Details

All the experiments were carried out in an ultrahigh vacuum system (base pressure approximately 1×10^{-10} mbar) equipped with a variable temperature scanning

tunneling microscope (VT-STM, Omicron NanoTechnology GmbH, Taunusstein, Germany) chamber, and a separate preparation chamber, which includes an ion sputter gun for sample cleaning, a LEED (Low Energy Electron Diffraction) system, and a directional gas doser. The Cu (111) single crystal (Marketech International, Port Townsend, WA) was polished on one side and mounted on a standard tantalum sample plate from Omicron with an 8 mm diameter hole on its rear end to facilitate electron bombardment heating. Cu (111) was cleaned by 8 cycles of sputtering (4×10^{-6} mbar Ar, 1.0 keV, 1 μ A, 20 minutes) and annealing (1000 °C, 10 minutes, *in vacuo*). Temperature above 600 °C (873 K) was monitored by a pyrometer (model OS3708; Omega Engineering Inc., Stamford, CT). Successful cleaning of the sample was confirmed by STM and LEED. Large continuous graphene islands were produced on Cu (111) surface through exposing the clean Cu (111) substrate to 1×10^{-5} mbar C₂H₄ at room temperature for 5 minutes, with subsequent annealing at 1000 °C (1273 K) for 5 minutes. This cycle was repeated 8 times. Successful graphene preparation was confirmed by scanning tunneling microscopy (STM). All STM images were collected at room temperature by using electrochemically etched tungsten homemade tips with a sample bias of 0.7 V and a constant tunneling current of 0.4 nA. All the post annealing images were generally acquired 2 hours after the experiment to ensure that the sample had returned to room temperature. To ensure that the images shown here are consistent across the crystal face, for any given surface condition, images were collected at multiple locations (usually 4 or 5) on the surface. All the STM data were processed using WSxM 5.0 software [174].

5.4. Computational and System Details

DFT calculations were performed using the Vienna Ab initio Simulation Package [58, 109, 110] with the PBE exchange-correlation functional and in the GGA formulation [56]. The electron-ion core interactions were treated by using the PAW pseudopotentials [57, 58] available in the VASP database. The Cu surface was constructed as a four atomic layer thick p (7×7) slab in Materials Studio [135] by cleaving along the (111) plane. A vacuum of 20 \AA thickness was applied on the slab along the z direction to prevent interactions of the slab with its upper/lower periodic images. The bottom layer was kept fixed and the remaining three layers were allowed to relax. Conjugate gradient algorithm with a Gaussian smearing width of 0.05 eV was used for all relaxations. Convergence tests were carried out, and a $1 \times 1 \times 1$ k -point mesh with a plane wave energy cutoff of 400 eV was selected for the sampling of the Brillouin

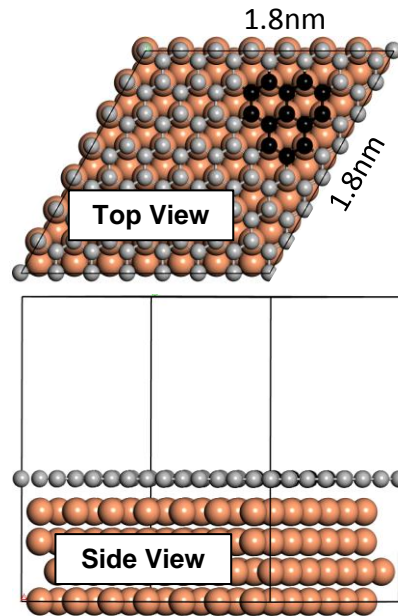


Figure 5.1 The Cu slab and the single graphene overlayer from which the fragments were extracted.

zone. The graphene fragments used in this study consist of three neighboring hexagonal rings, initially taken from Materials Studio structures database and then relaxed. Relaxed structures were then used on the Cu surface. **Figure 5.1** depicts the constructed Cu slab and a single graphene overlayer of which the graphene fragments were extracted. *Ab initio* molecular dynamics (AIMD) were performed using VASP with the foregoing computational details. AIMD simulations were carried out in the NVT ensemble with a 1 fs time step and at two temperatures of 900 K and 1200 K.

5.5. Experimental Observations

One promising approach to prepare large graphene sheets with low defects on metal substrates is by thermal dissociation of an organic precursor on the metal surface [97, 175-177]. Gao et al showed that epitaxial growth of graphene on Cu (111) by thermal decomposition of ethylene (C_2H_4) at 1000 °C results in formation of single-layer graphene platelets and sheets [97]. Similarly, to produce large continuous graphene islands on Cu (111) surface, we undertook a controlled thermal cycling approach using the organic precursor, (C_2H_4). Successful preparation of large continuous graphene film over Cu (111) surface was confirmed by STM as shown in **Figure 5.2**. Since different moiré patterns could be observed under specific tunneling conditions, it was difficult to capture all moiré patterns in one single image. Thus, more than one method was needed to interpret the STM data and to conclude whether we had a full coverage graphene/Cu (111).

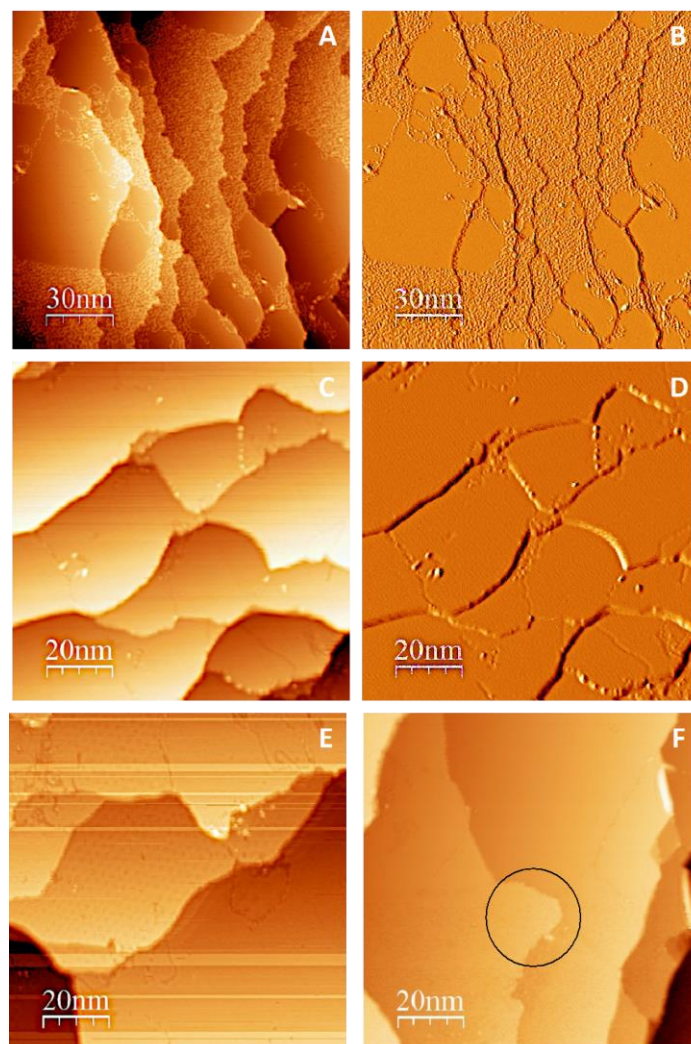


Figure 5.2 Topographical and differential conductance (dI/dV) STM images of graphene growth on Cu (111), provided by Prof. Homa Khosravian. (A) Graphene islands and C atoms are both observed in one single image before final controlled annealing. (B) Differential conductance (dI/dV) image of the STM image shown in A. Graphene islands look smoother and darker in differential conductance images. (C) Complete graphene coverage over Cu (111) after final annealing. The domain boundaries are visible in this STM image. (D) Differential conductance (dI/dV) image of STM image shown in C. The entire image has the same color, which indicates either all the terraces are Cu (111) or graphene/Cu (111). Other parts will support that the latter is true. (E) Moiré pattern was observed on some terraces. (F) Graphene films grown through the controlled thermal cycling method terminated at Cu (111) step edges but changed their shape (the area inside the black circle shows such a shape change).

Figure 5.2A (topographical image), and **Figure 5.2B** (differential conductance (dI/dV) image) were captured after the 7th cycle of thermal annealing. As shown in these two images, graphene islands and C atoms are both observed in one single image before final controlled annealing. Note that graphene islands look smoother and darker in differential conductance images. However, as shown in **Figure 5.2C** (topographical image) and **Figure 5.2D** (differential conductance (dI/dV) image), after final cycle of thermal dissociation of C_2H_4 (8th cycle), complete graphene coverage over Cu (111) was observed. The domain boundaries are visible in these STM images. Note that the entire differential conductance image has a uniform color, which indicates that either all the terraces are Cu (111) or graphene/Cu (111) and **Figure 5.2E and 5.2F** support that the latter is true. Moiré pattern was observed on some terraces of **Figure 5.2E and 5.2F** shows the shape changes of Cu (111) terrace, which is a result of successful preparation of graphene [97]. As shown in **Figure 5.2E and 5.2F**, graphene films grown through this method terminated at Cu (111) step edges but changed their shape (the area inside the black circle in **Figure 5.2F** shows such a shape change).

5.6. Results

5.6.1. Adsorption of C_6 rings and graphene islands on Cu (111)

5.6.1.1. Rings

The adsorption of C_6 rings and graphene islands on different adsorption sites has been studied elsewhere using DFT [7, 178]. Compared to these earlier studies, the cell used here is larger to accommodate end effects, and a GGA functional used (PBE) which is more accurate than the local density approximation (LDA). Using DFT

optimizations, a C₆ ring was allowed to relax onto the Cu (111) surface. Three main possibilities were tested; (a) the ring surrounds a top Cu atom and the C atoms of the ring occupy *fcc* and *hcp* hollow sites (*fcc-hcp*), (b) the ring surrounds an *hcp* site and the C atoms occupy *fcc* and top sites (*fcc-top*), and (c) the ring surrounds an *fcc* site and the C atoms occupy *hcp* and top sites (*hcp-top*), alternately. Results, illustrated in **Appendix C (Figure C1)** showed that the *fcc-hcp* is the most thermodynamically favorable site. This arrangement also allows for perfect matching of the Cu (111) lattice and the honeycomb structure of the hexagonal ring, whereas other arrangements cause slight stress in the hexagonal ring. Also inferred from the figure is that the adsorption energy differences between the possible adsorption sites are less than 0.05 eV per C atom. Furthermore, figures found in **Appendix C (Figures C2-C3)** illustrate the energy barriers obtained from NEB calculations for the diffusion of the *fcc-hcp* arrangement to the *fcc-top* and *hcp-top*. These barriers are approximately 0.45 eV which is quite low. Therefore it can be concluded that a single hexagonal ring, once formed, can travel on the Cu surface at a low energy cost. The perfect match between the ring and Cu lattice is only limited to a small number of rings. With an increase in the number of rings, the mismatch between the lattices of graphene and Cu will eventually lead to moiré patterns.

5.6.1.2. Graphene Fragments

In addition, we also allowed a pre-relaxed graphene fragment, composed of 13 C atoms constituting 3 rings, to relax on the Cu surface. We studied 7 different orientations of the fragment with respect to the Cu lattice. These orientations were from 0° to 60° with 10° increments. Results are illustrated in **Appendix C (Figure C4)**. The energy

required for the adsorption of various rotations is slightly greater than a single ring. Nevertheless, similar to a single hexagonal ring, a strong preference towards a certain alignment of a graphene fragment with Cu is not apparent, although the 40° is slightly less favorable than others. The most energetically favorable graphene orientation on Ir (111), Au (111) and Cu (111) has been identified and reported elsewhere [171, 179, 180]. Here, the focus was to determine the most favorable orientations of a graphene fragment rather than a graphene sheet on the Cu surface. This represents the initial nucleation stages observed experimentally on the Cu (111) terraces as discussed in relation to **Figure 5.2**.

5.6.2. Effect of Temperature on the Rotation and Orientation of an Isolated Fragment

In the experimental part of this work, the technique of low and high temperature cycles was applied to grow the graphene sheet. Reportedly, graphene coverage can be controlled by the number of thermal cycles. Here, several aspects of this process were emulated by using AIMD simulations to understand the effect of these cycles on the stability of the graphene fragments with respect to the underlying substrate. First, the motion and rotation of an isolated fragment at two temperatures of 900 K and 1200 K were studied. The selection of temperatures was largely dictated by other experimental studies [97] as well as our own. Prior to running AIMD simulations, the fragment was relaxed onto the Cu surface with an initial misalignment of 24° with respect to the Cu (111) lattice as shown in **Figure 5.3**. The relaxed system was then allowed to evolve for 10 ps while rotation and alignment of fragment was checked every 1 ps.

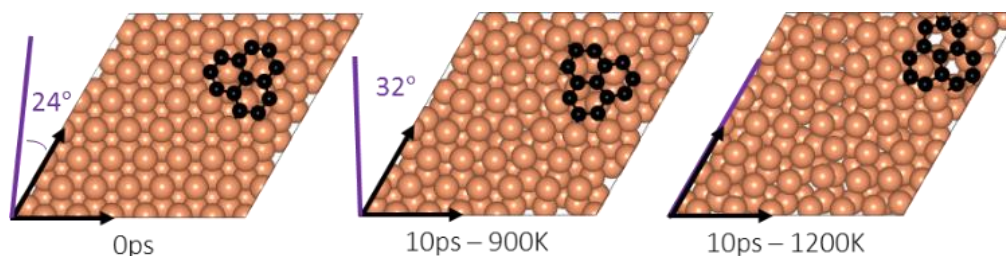


Figure 5.3 An isolated graphene fragment adsorbed on the Cu (111) surface before AIMD (0ps) and after 10ps at temperatures of 900K and 1200K. The initial orientation (24°) of the fragment with respect to Cu lattice is shown in purple at 0ps. The final orientations are 32° for 900K and zero for 1200K.

Clearly, the fragment does not remain stationary but is rather in coordinated motion with the underlying surface Cu atoms as they reorder and reconstruct the surface (shown in **Figure 5.4**). We observed the fragment to rotate in both clockwise and anti-clockwise directions. At the higher temperature of 1200 K and within 10 ps, the fragment had rotated to the extent of completely aligning with the Cu (111) lattice. At the lower temperature of 900 K, the same relaxed fragment was less mobile and was not able to correct the initial 24° misalignment with the Cu lattice. What is apparent from the images is that the surface Cu

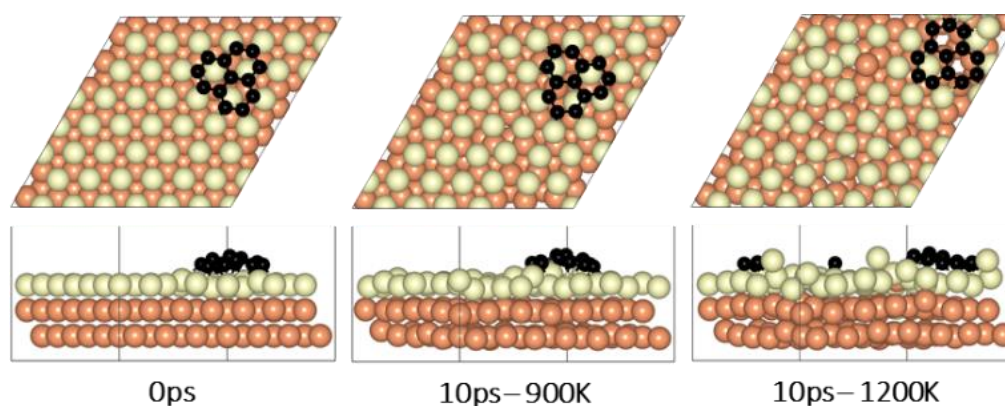


Figure 5.4 Surface reconstruction observations of the Cu slab in the presence of a graphene fragment taken from 10ps of AIMD simulations performed at temperatures of 900K and 1200K. Light green atoms depict surface Cu atoms.

atoms are more disordered at the higher 1200 K temperature. The ability of the graphene fragment to correct the misorientation at the higher temperature of 1200 K may therefore be linked to the elevated mobility of surface Cu atoms at higher temperatures.

The relaxed system was then allowed to evolve for 10 ps while rotation and alignment of fragment was checked every 1 ps. Clearly, the fragment does not remain stationary but is rather in coordinated motion with the underlying surface Cu atoms as they reorder and reconstruct the surface (shown in **Figure 5.4**). We observed the fragment to rotate in both clockwise and anti-clockwise directions. At the higher temperature of 1200 K and within 10 ps, the fragment had rotated to the extent of completely aligning with the Cu (111) lattice. At the lower temperature of 900 K, the same relaxed fragment was less mobile and was not able to correct the initial 24° misalignment with the Cu lattice. What is apparent from the images is that the surface Cu atoms are more disordered at the higher 1200 K temperature. The ability of the graphene fragment to correct the misorientation at the higher temperature of 1200 K may therefore be linked to the elevated mobility of surface Cu atoms at higher temperatures.

5.6.3. Effect of Temperature on the Rotations and Alignments of a Pair of Fragments

To understand the effect that neighboring graphene fragments may have on a single fragment, a second fragment was added to the vicinity of the isolated fragment of the previous section. Although, the orientation of the second fragment with the first fragment was not set arbitrarily.

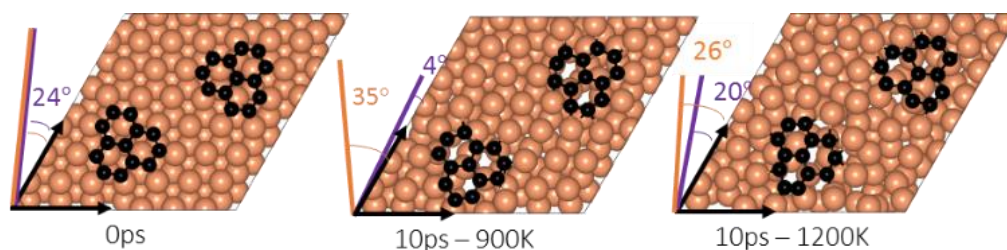


Figure 5.5 A pair of graphene fragments adsorbed on the Cu (111) surface (distance between centers of mass = 1nm) before AIMD (0ps) and after 10ps at temperatures of 900K and 1200K. The initial orientations (24°) of both of the fragments with respect to Cu lattice is shown in purple at 0ps. The final orientations at 900K are shown as 35° for the left fragment (in orange) and 4° for the right (in purple). The final orientations at 1200K are 26° for the left fragment (in orange) and 20° for the right (in purple).

Four different orientations of 0° , 30° , 60° and 90° between the two fragments. The most energetically favorable was found to be the 60° orientation. This structure resulted in 24° misalignment of both fragments with the Cu (111) lattice and the AIMD simulations were started with this initial structure. **Figure 5.5** shows results of AIMD simulations.

As in the isolated fragment, we observed rotations of fragments in both directions.

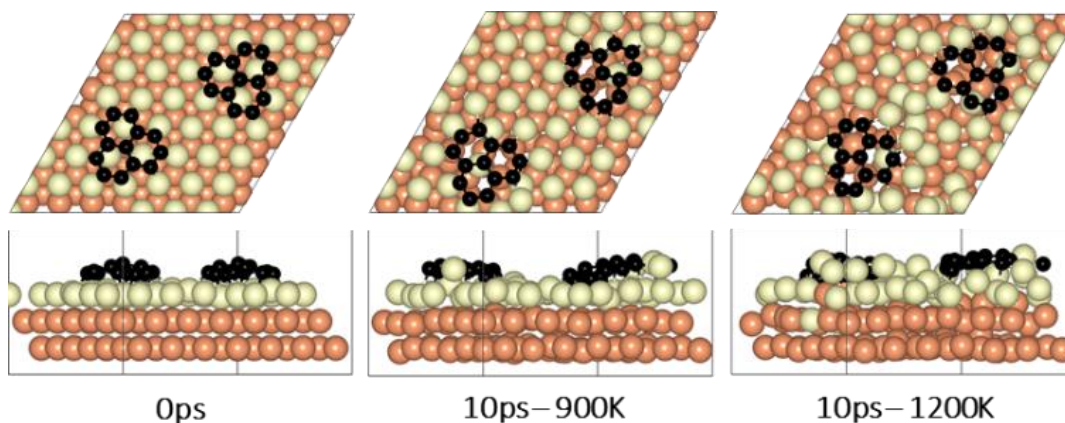


Figure 5.6 Surface reconstruction observations of the Cu slab in the presence of a pair of graphene fragments taken from 10ps of AIMD simulations performed at temperatures of 900K and 1200K. Light green atoms depict surface Cu atoms.

Rotations of the two fragments were also observed to oppose each other. At the higher temperature of 1200 K and at the end of 10 ps, neither of the fragments were observed to align with the Cu lattice. The disordering of the surface Cu atoms, shown in **Figure 5.6**, was also quite significant. At the lower temperature of 900 K, the misalignments with Cu lattice were less and one of the fragments succeeded in gaining close alignment with the Cu lattice. As evident from the figures, surface reconstruction of Cu atoms is low at this temperature. Therefore, while the higher 1200 K temperature was effective in mobilizing surface Cu atoms and aligning the isolated fragment with the Cu lattice, in the presence of a second fragment, this surface disordering is even more intense and may perhaps hinder the correction of the misalignment. Therefore, it is found that once small graphene fragments are formed, the more moderate temperature of 900 K, may be more effective in achieving alignment with the Cu lattice.

5.6.4. Effect of Fragments Proximity on the Rotation and Alignments of Fragments

To study the effect of proximity on additional graphene islands in the vicinity of the first one, the second graphene fragment of the previous section, was placed closer (by 0.2 nm) to the initial fragment and relaxed the structure before running AIMD simulations. Results are shown in **Figure 5.7**. As such, at 1200 K, the pair fragments were able to align with the Cu lattice. In the majority of times, the two fragments rotated in the same direction. At 900 K, however, the misalignment decreased but persisted throughout the 10 ps of simulation time. The Cu surface reconstruction (shown in **Figure 5.8**) was also considerably lower than when fragments were farther away from each other. The greater degree of disorder seen in the case of fragments farther apart from each other is in fact the surface Cu atoms being raised

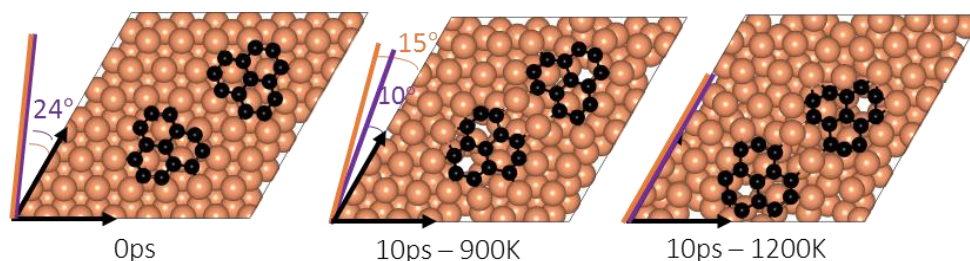


Figure 5.7 A pair of graphene fragments adsorbed on the Cu (111) surface at close vicinity to each other (distance between centers of mass = 0.8nm) and after 10ps at temperatures of 900K and 1200K. The initial orientations (24°) of both of the fragment with respect to Cu lattice is shown in purple at 0ps. The final orientations at 900K are 15° for the left fragment (in orange) and 10° for the right (in purple). The final orientations of both fragments at 1200K are zero.

with unsuccessful attempts to create bridges between the two fragments. Note that this is a periodic cell. Considering neighboring images to the depicted two fragments, the raising of surface Cu atoms is occurring in all directions. However, the fragments are not as close for bridging to occur. When the fragments are in close proximity, the bridging is achieved on the side that fragments are closer to each other, while the remaining area in the cell is not close enough to any fragment (even in periodic images) for surface Cu atom to rise.

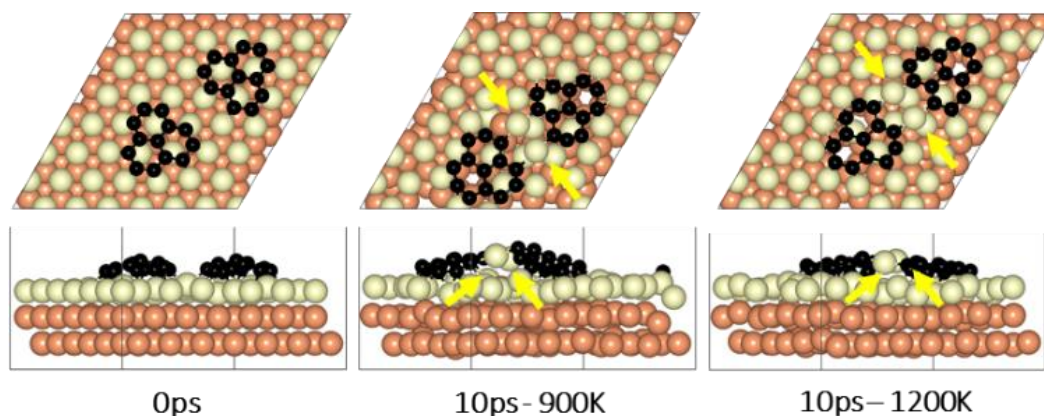


Figure 5.8 Surface reconstruction observations of the Cu slab in the presence of a pair of graphene fragments at close vicinity taken from 10ps of AIMD simulations performed at temperatures of 900K and 1200K. Light green atoms depict surface Cu atoms.

The bridging-metal structure previously reported for Cu [114, 181, 182], Fe [183] and Ni [183, 184] surface atoms in graphene growth was clearly observed in this part of the work. Both fragments were able to bond to two surface Cu atoms situated between the two fragments and by doing so, raise those atoms from the surface (seen in **Figure 5.8**). Inevitably, the two metal atoms bridging between two graphene fragments, lead to the equaling of fragments orientations with respect to each other and unifying their rotations and movements on the Cu surface. In comparison with the case of two fragments farther away from each other, graphene fragments located in close proximity of each other, *i.e.* high density of graphene fragments on the Cu surface, seems to accentuate the ability of higher temperatures to correct graphene/Cu misalignment. Once greater number of graphene fragments/islands are formed at lower temperatures, increasing the temperature, may help coalesce the fragments into a larger fragment that is well-aligned with respect to the Cu lattice. It is suspected that at higher graphene island densities, these bridging metal atoms will eventually be suppressed down to the rest of the metal catalyst surface as graphene islands are brought into contact with each other. This hypothesis can be observed in the STM images (**Figure 5.2**). The density of independent graphene fragments is large enough just before the final annealing after which a complete graphene layer is formed. The graphene layer does not show major moiré patterns and holds a certain alignment with the Cu substrate. The moiré patterns observed are especially located on some terraces. This observation was also reported elsewhere [94, 97].

5.7. Conclusions

In this chapter, the effect of temperature and thermal cycles on the alignment of graphene islands in the early stages of epitaxial growth of graphene on Cu(111) surface and when only small graphene islands have been formed, is studied. Hereafter, the islands may align with respect to one another and form a uniform graphene sheet or each may grow about their own specific alignment with the Cu lattice and produce various domains. The effect that temperature may have in choosing either of these paths was closely examined. It is found that higher temperatures generally lead to the alignment of an island on the Cu surface. An isolated graphene pallet at high temperatures (above 900 K) is able to correct an initial misalignment and align itself perfectly with the Cu surface. This is attributed to the higher mobility of the Cu catalyst surface layer which allows graphene to rotate freely. As growth proceeds at lower temperatures and the number of graphene fragments increases, metal-bridging of surface Cu atoms which was observed, unifies graphene islands. Therefore, increased growth rate at lower temperature combined with increased mobility at higher temperatures lead to the production of large high quality graphene films with the perfect alignment of graphene islands with Cu lattice.

6. HYDROCARBON DECOMPOSITION ON SUPPORTED NANOPARTICLES*

6.1. Summary

In this chapter, DFT is used to study some aspects of the growth of SWCNT on Cu as a potential non-traditional catalyst. Several parameters of nucleation and growth such as C precursor gas dissociation, C dissolution and catalyst morphology evolution during reaction are investigated. The effect of doping the MgO support with Mo on C₂H₂ dissociation is evaluated for Cu nanoparticles and compared alongside Co nanoparticles. Doping the MgO support, resulted in the decrease of the energy barrier for dehydrogenation on both catalysts, but the increase in energy barrier for CH-CH bond scission on the Cu nanoparticle catalyst. Results also show that the activation energy barrier for C₂H₂ dissociation (dehydrogenation and CH-CH bond scission) is consistently greater for Cu than for Co on the three MgO supports studied here. Although in general, dehydrogenation of C₂H₂ was found to be less energy consuming than CH-CH bond scission.

Regarding C dissolution, results show very low carbon solubility for both supported and unsupported Cu nanoparticles, although bigger Cu nanoparticles exhibit slightly higher C solubility. Generally, the interacting carbons are found to be localized on the surface of the Cu nanoparticles, hinting at the surface-mediating nature of Cu. In

* Parts of this chapter are reprinted with permission from Behnaz Rahmani Didar and Perla B. Balbuena. "Growth of Carbon Nanostructures on Cu Nanocatalysts". The Journal of Physical Chemistry C 2017, 121 (13), 7232-7239. Copyright (2017) American Chemical Society

the case of supported Cu nanoparticles, nanoparticle–support adhesion energies indicate weak Cu–O bonding that allows the nanoparticle to remain nearly spherical on the support. In turn, this may facilitate the separation of the nanoparticle from the support, once the SWCNT has formed. Growth of curved carbon structures is examined by placing a graphene fragment in contact with the supported Cu nanoparticle.

6.2. Introduction

Traditional catalysts of choice for SWCNT growth (Fe, Co, and Ni and their alloys) have the tendency to form strong bonds with carbon and nascent CNT, maintain the nanotube open-end structure, and allow lengthening of the CNT [185]. Studies suggest that CNT nucleation and growth is possible to take place via different mechanisms [4, 186, 187]. It is believed that the mechanism of graphene growth on Cu is surface-mediated and different from that on other traditional catalysts such as Fe, Co, and Ni [6, 15]. On the Cu surface, reports show growth to begin simultaneously with C precursor gas dissociation, indicating the absence of intermediate steps such as penetration of carbon into the subsurface and formation of carbides as seen in, for example, Ni [188].

In order to optimize graphene and SWCNT growth, it is crucial to understand the underlying atomistic details of nucleation and growth. A knowledge of the C precursor gas dissociation pathway, and its active species and their evolution, can provide valuable insights required for tuning growth conditions. Many studies focus on the growth mechanism *after* the C precursor has dissociated on the catalyst, where C atoms begin to form networks. However, one of the crucial roles of the catalyst is to decompose the C

precursor gas. C_2H_2 is a commonly used C precursor gas in the growth of graphene and SWCNTs. The dissociation process of C_2H_2 has been investigated using first-principles calculations on Fe and Ir surfaces [134, 189-191]. Reportedly, on both Fe and Ir surfaces, C_2H_2 dissociates by breaking the C-C bond and forming CH species. CH species then dehydrogenate and form C monomers. To date, such detailed atomistic information is not available for the decomposition of C_2H_2 on the Cu catalyst surface. Studies devoted to this area are scarce and therefore information is limited. This is also the case for catalysts that are supported and the system of catalyst/support catalyzes the decomposition.

One such system is used in the CoMoCAT process. Since its first introduction by Resasco and co-workers [192], many studies have reported the promoting effect of adding Mo to the usual Co catalyst [37, 193, 194] that is supported by SiO_2 . The C precursor gas in the CoMoCAT process is CO. While the role of Mo is not fully understood, it has shown positive effects on the carbon yield (catalytic activity) and structure (chirality and SWCNT:MWCNT selectivity) of CNT. Narrow chirality distribution is obtained from the grown SWCNT. Many researchers in the SWCNT community have adopted the method with some variations from its original format [37, 144, 195-198], for example by substituting SiO_2 with MgO. In this method, as reported by Picher et al [144], a Co-Mo/MgO catalyst powder is used to prepare the catalyst and catalyst support and C_2H_2 is used as the C precursor gas. Reportedly, as seen from environmental scanning transmission electron microscope (ESTEM) videos, the resulting catalyst nanoparticles of CoO phases transition to Co_xC upon the introduction

of C_2H_2 . Further C deposition on the nanoparticles lead to nucleation of SWCNT. However, although Mo is used in the preparation, no Mo is detected in active catalyst nanoparticles. As such, the exact role of Mo in this method remains unknown.

Nevertheless, Mo addition, as a catalyst promoter to other catalysts such as Fe and Ni has been reported to improve the yield of the grown SWCNT [199, 200]. In fact the role of Mo is such that in the absence of Mo in the CoMoCAT process, almost no SWCNT can be grown and Mo on its own cannot grow any form of CNT. The aforementioned findings have largely been obtained from experimental investigations. Therefore, it seems reasonable to analyze and understand the role of Mo from an atomistic point of view.

On the other hand, perhaps one of the most important and common attributes of metal oxide supports to catalysis, is their ability to transfer charge to overlying metal particles in contact with them. Supported catalytic metal particles have indeed shown greater catalytic reactivity owing to the presence of charge transfer from the support [201-204]. Doping of metal oxides has become a common route for tuning and manipulating the interaction between a metal oxide and a metal particle. The removal of a cation of the metal oxide and substitution with another metal is one type of doping. In this Chapter, the effect of Mo-doping of the support on the activity of the catalyst (Cu and Co) towards the initial steps of C_2H_2 dissociation is studied.

The general mechanism of CNT nucleation and growth on traditional catalysts such as Fe, Co and Ni has been roughly described as follows [205, 206]: The C precursor gas dissociates on the surface of the catalyst particle, producing C atoms. C

atoms dissolve inside the nanoparticle where they may or may not form stable carbides with the metal atoms. The addition of C atoms continues until saturation of the catalyst is reached. C atoms diffuse and precipitate to the surface of the catalyst and form nascent CNT structures. C solubility is an important factor in determining the deposition mechanism [207]. Due to the low solubility of Cu toward C, dissociated C atoms remain on the surface of Cu via weak Cu–C bonding and contribute to graphene growth. Solubility of carbon in noble metals such as Cu is orders of magnitude lower than that in other transition metals, and no carbides have been observed for the systems of these metals and carbon [156, 159]. In addition, the energy barrier for surface diffusion of carbon on Cu is low, which can contribute to carbon network growth. As such, it seems that CNT nucleation and growth is possible to take place via different mechanisms and that formation of carbides may not be necessary [4, 186, 187]. In addition, while extensive theoretical literature is available for SWCNT growth on early transition metals, there exists less for the case of noble metals. In one of the few studies of SWCNT growth on noble metal catalysts, Cu has been reported as a superior catalyst on the basis of catalytic activity for decomposing carbon feedstock gas and, low carbon solubility and also Cu's weak interaction with the substrate [158]. While the former is addressed in the first part of the Chapter, the latter motivates the investigation of the potential of Cu in SWCNT growth in terms of C solubility and interactions with the substrate and the nascent nanotube.

The Chapter starts by studying the dissociation of C_2H_2 on supported Cu and Co nanoparticle catalysts. For the support, a rock-salt metal oxide, namely MgO, is used.

Rock-salt metal oxides are known to be good catalysts, catalyst supports, and adsorbents [208, 209]. MgO, is most common due to its easier removal process from the catalyst and CNT after growth [37]. Two facets of MgO, namely (100) and (105)–which is a stepped surface– are chosen. To evaluate the effect of Mo, the dissociation is also studied for the case of Cu and Co supported by Mo-doped MgO (100). In all cases, while the focus is Cu, Co is also studied for comparison.

In the latter part of this Chapter, the structure and evolution of unsupported carburized Cu nanoparticles in three sizes (38-, 55-, and 68-atoms) are first studied. Here, carburized particles can be defined as those that contain a certain concentration of C atoms in their interior, without necessarily having a carbide structure. At this point, the energetics, interactions, and positions of C in/on the nanoparticle clusters are of interest. Then, the procedure is repeated for MgO-supported carburized Cu nanoparticles in two sizes (32 and 38 atoms). Two facets of MgO – (100) and (111) – are studied. For all cases, charge densities are mapped to find regions of charge accumulation and depletion and, in general, to identify the charge transfer direction. Finally, results of the energetics of carbon incorporation into the nanoparticles in supported and unsupported clusters are compared to understand the effect of the support on the catalyst nanoparticle and eventually on the growth of carbon nanostructures.

6.3. Computational and System Details

The Vienna ab initio Simulation Package (VASP) was used to perform DFT calculations [58, 109, 110]. The electron exchange and correlation effects were treated with the GGA-PBE method [56]. The electron–ion core interactions were treated with

the PAW pseudopotentials [57, 58]. For geometry relaxations, the conjugate gradient algorithm with an energy stopping criterion of 10^{-4} eV was used. The smearing scheme used for relaxations was Gaussian with a width of 0.05 eV. In all relaxations, a gamma-point Brillouin zone sampling for integration in the reciprocal space was used. To map and analyze charge densities the Bader charge analysis scheme was employed [136, 137].

For Part 1, the MgO (100) slab consisted of a p (4×4) supercell arranged in four atomic layers of which the top two were allowed to fully relax during all calculations. A $3 \times 3 \times 1$ k-point mesh with a plane wave energy cutoff of 400 eV was selected as the most appropriate for the sampling of the Brillouin zone. Periodically repeated slabs were separated by a vacuum of more than 10 Å thickness to avoid interactions of the slab with its upper/lower periodic images. The (105) facet of MgO was chosen to represent a stepped MgO surface. The MgO (105) consisted of a p (1×2) supercell. A $1 \times 2 \times 1$ k-point mesh was selected for the sampling of the Brillouin zone.

For Part 2, two facets of MgO were studied; the (100) and oxygen-terminated (111) facet, which is more active than Mg-terminated (111) facet. The alternating layers of oxygen and magnesium cause the (111) facet to become polarized. To prevent the cluster from spreading on the MgO(111) facet, the O on the surface of MgO(111) were hydroxylated with a monolayer of H. Thus, the OH layer stabilizes the polar surface [208, 210]. The (100) and O-terminated (111) MgO slabs each consisted of p (7×7) supercells. For both facets, a $1 \times 1 \times 1$ k-point mesh was selected for the sampling of the Brillouin zone. A vacuum of 20 Å thickness was used for both slabs.

6.4. Results

6.4.1. Part 1

6.4.1.1. Mo-Doping of the MgO Surface

Three possible Mo doping configurations (modifications) were investigated; the substitution of Mo for Mg (cation doping) on the top layer, the adsorption of Mo on the MgO surface (hollow, O-top and Mg-top sites) and the insertion of Mo in the MgO subsurface (seen in **Figure 6.1**). The formation energies of Mo substitution, adsorption and insertion were calculated, in order, by:

$$E_{sub} = (E_{sys} + E_{Mg}) - (E_{MgO} + E_{Mo}) \quad (6.1a)$$

$$E_{ads} = E_{sys} - (E_{MgO} + E_{Mo}) \quad (6.1b)$$

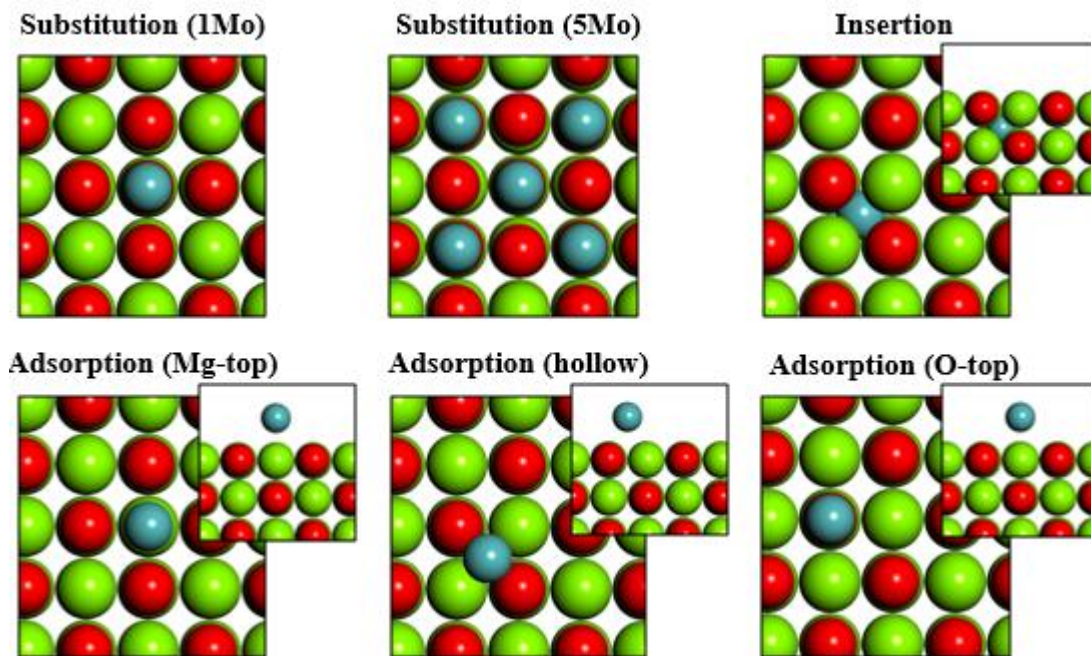


Figure 6.1 Modifications to the MgO (100) surface by substitution of Mo (1 and 5 atoms) for Mg on the top layer, adsorption of Mo on MgO and insertion of Mo in MgO subsurface. Mg, O and Mo atoms are shown in green, red and blue.

$$E_{ins} = E_{sys} - (E_{MgO} + E_{Mo}) \quad (6.1c)$$

where E_{sys} , E_{Mg} , E_{MgO} and E_{Mo} are the system total, atomic Mg, MgO slab and atomic Mo energies. Formation energies of modifying the MgO (100) surface with Mo calculated from **Equations 6.1a-c** are shown in **Table 6.1**. Substitution of Mo for Mg yields the most negative formation energies, hence doping the Mg surface by substitution Mo for Mg is the most thermodynamically favorable way of doping MgO with Mo. This type of doping will be used for the remainder of the study. Bader charge analysis reveals that the charge on the substituted single Mo atom for a single Mg atom is $+1.15|e|$. The average charges on the 5 Mo atoms for 5 Mg atoms is $+1.18|e|$.

6.4.1.2. Adsorption of Cu and Co Atoms and Nanoparticles on Pristine, Mo-Doped and Stepped MgO Surfaces

The adsorption of single Cu and Co atoms on the three types of MgO surfaces

Table 6.1 Formation energies of the three types of modifications of the MgO (100) by Mo; substitutional (cation doping), adsorption and insertion. For the substitution of 5Mo atoms for 5Mg atoms, the formation energy is normalized by the number of Mo atoms.

Modification	$E_{formation}, eV$
Substitution	
1Mo	-2.92
5Mo	-2.83
Adsorption	
hollow	-1.64
O-top	-1.77
Mg-top	-1.54
Insertion	0.12

(pristine, Mo-doped and stepped) was evaluated. **Figure 6.2** depicts the geometry optimized structures of most favorable adsorption configurations. Adsorption energies of Co to the MgO surfaces are also greater than those of Cu. The bond lengths of Co with any of the three MgO surfaces are all shorter than those of Cu. Therefore, Co is more strongly bound to the MgO surfaces than Cu. Charges of Cu, Co and Mo atoms are also shown on **Figure 6.2**. Adsorption on MgO (100), yields electronic charges of $-0.15|e|$ and $-0.14|e|$ for Cu and Co, respectively. On the stepped MgO surface, the charges of Cu

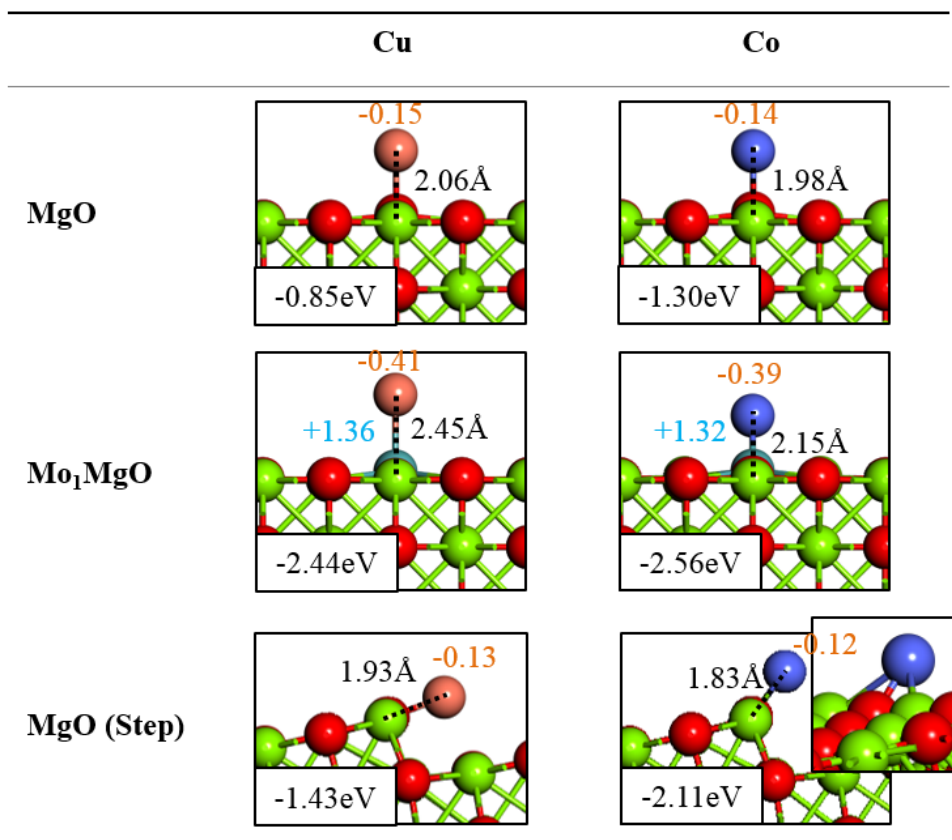


Figure 6.2 Most favorable adsorption configurations of Cu and Co atoms onto the three types of MgO surfaces. Adsorption energies, bond lengths and Bader charges (orange for Cu/Co and blue for Mo) are also indicated. Mg, O, Mo, Cu and Co atoms are shown in green, red, blue, orange and darker blue.

and Co are $-0.13|e|$ and $-0.12|e|$, respectively, and very similar to the charges on pristine MgO. The adsorption of Cu on Mo-doped MgO yields a charge of $+1.36|e|$ for Mo. As such, with the adsorption of a Cu atom, the electronic charge of Mo has increased from $+1.15|e|$ to $+1.36|e|$. Similarly, with the adsorption of Co on Mo-doped MgO, the charge of Mo increases to a more positive value of $+1.32|e|$. The charges of Cu and Co are both negative; $-0.42|e|$ and $-0.39|e|$, respectively. In comparison to their values on pristine MgO, this shows a considerable change in Cu and Co charges due to the presence of the Mo dopant. This indicates a charge transfer from the dopant Mo to Cu and Co upon their adsorption. Such charge transfers have been reported for other doped oxides [204]. Charge transfers are the basis of many phenomena such as oxidation, reduction and bond activation [211].

The building (growth) of Cu and Co nanoparticles was followed via a step-by-step path of one Cu or Co atom at a time, finding the most favorable adsorption site of the atom at each addition step. Here, to clearly see the effect of Mo, rather than 1 Mo, the case of 5 Mo dopants on the MgO surface was pursued. **Figure 6.3** shows the structures of 9 atom Cu/Co atom nanoparticles on the pristine and 10 atom Cu/Co atom nanoparticles on the Mo-doped and stepped MgO surfaces. Mo-doping of the MgO surface, has induced a certain crystal structure to the Co nanoparticle which involves the (111) facet seen from the top view of **Figure 6.3d** as opposed to the (100) facet seen from the top view of **Figure 6.3b**. Faceting on Cu nanoparticles however, seems to be more or less similar on the three MgO surfaces. More importantly, there exists a striking difference between the nanoparticles growth modes atop the three types of MgO surfaces.

The structures of the nanoparticles are 3D when grown on top of pristine and stepped MgO, but 2D on the Mo-doped MgO. This is in agreement with observations of nanoparticle growth on some Mo-doped oxides in the literature. The Mo dopant has been reported to change the growth mode of gold nanoparticles from 3D on pristine CaO surface to 2D on Mo-doped CaO surface [202]. This change has been attributed to the

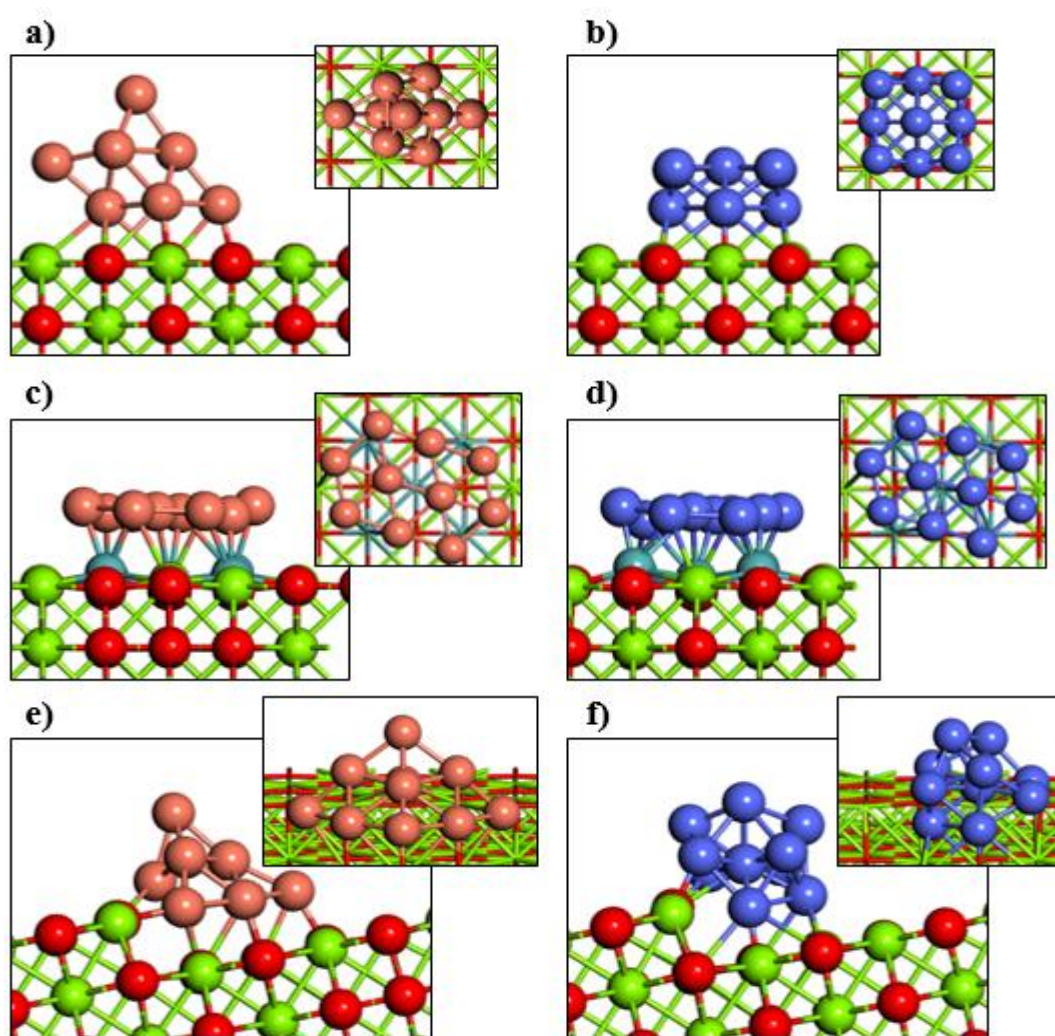


Figure 6.3 Structure of nanoparticles built by successive addition of atoms. a) and b) Cu₉ and Co₉ on MgO, c) and d) Cu₁₀ and Co₁₀ on Mo-doped, e) and f) Cu₁₀ and Co₁₀ on stepped MgO (i.e. MgO (105)).

charge transfer from the Mo to the gold nanoparticles and the gaining of negative charge by the gold nanoparticles. However, this behavior is dependent on the nature of the dopant and oxide [212, 213]. It is worth noting that the 2D structure is the case for the nanoparticle size of 10 atoms that was studied here. Perhaps this 2D structure can prevail with the addition of more atoms and therefore form a thin monolayer on the MgO surface.

The 3D structures of Cu nanoparticles are also different from those of Co nanoparticles which are more compact. The adsorption energies of Cu and Co to the MgO surfaces per each addition step are shown in **Figure 6.4**. This energy was calculated for each n addition step by:

$$E_{ads} = \frac{E_{sys} - (E_{MoMgO} + nE_{Cu\ or\ Co})}{n} \quad (6.2)$$

Where E_{sys} , E_{MoMgO} , $E_{Cu\ or\ Co}$ are the system total, Mo-doped MgO and free atomic Cu or Co energies. The adsorption of Co atoms to MgO surfaces is generally

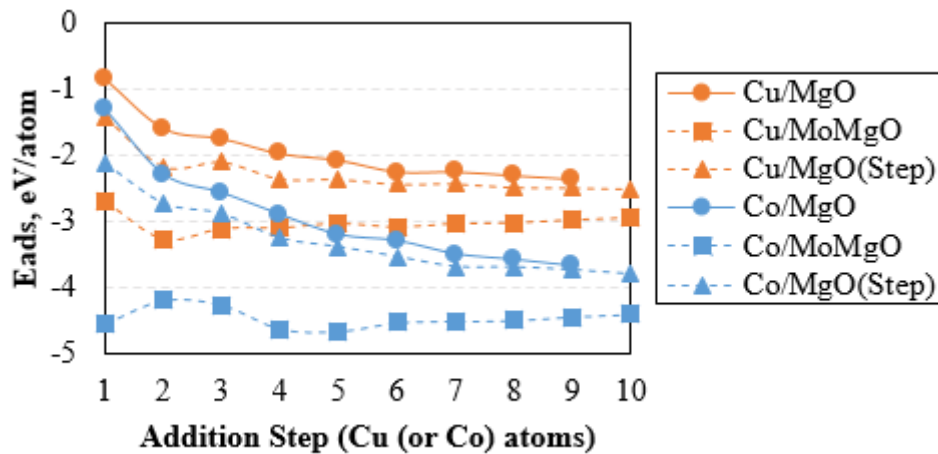


Figure 6.4 Adsorption energies of Cu and Co to the MgO surfaces per each addition step.

more thermodynamically favorable than Cu atoms, even as the nanoparticle grows. Stepped MgO and Mo-doping of MgO cause increase in adsorption energy for both Cu and Co nanoparticles, although the effect is more significant with Mo-doping. The cohesive energies of the Cu and Co nanoparticles were also evaluated at each addition step of the atoms by:

$$E_{coh} = \frac{E_{Cu\ or\ Co\ NP} - nE_{Cu\ or\ Co}}{n} \quad (6.3)$$

where $E_{Cu\ or\ Co\ NP}$ is the energy of the Cu or Co nanoparticle. Results are shown in **Figure 6.5**. The general trend is that Co nanoparticles have greater cohesive energy than Cu nanoparticles and are therefore more compact. However, Mo-doping of MgO decreases the cohesive energy of the Co nanoparticle while increasing that of the Cu nanoparticle. As a conclusion, Mo-doping the MgO surface forces a 2D structure to the nanoparticles of Cu and Co and increases the adsorption of these nanoparticles to the MgO surface.

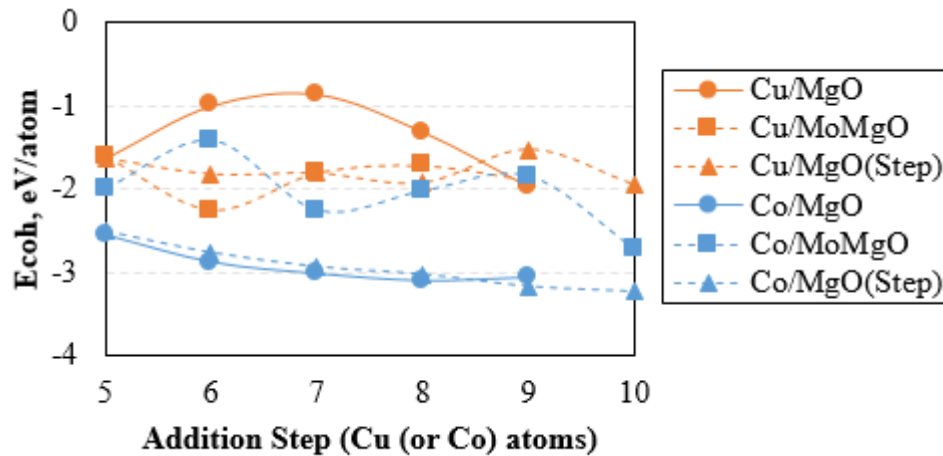


Figure 6.5 Nanoparticle cohesive energies on the MgO surfaces per addition of Cu or Co atoms.

6.4.1.3. The Adsorption and Dissociation of C₂H₂ on Supported Cu and Co Nanoparticles

6.4.1.3.1. C₂H₂ Adsorption

After preparing the Cu and Co nanoparticles on top of each MgO support, C₂H₂ was allowed to adsorb on the nanoparticles. Adsorption was tested for all possible sites. The most thermodynamically favorable adsorption configuration for each case and their energies are shown in **Figure 6.6-6.8**. In the same figures, charge density difference maps of the configurations before the adsorption of C₂H₂ are depicted. The charge density differences were found by subtracting the sum of the charge densities of nanoparticle and the support from the total charge density. From the adsorption energy point of view, on all three surfaces, C₂H₂ binds stronger to the Co than to the Cu nanoparticle. Also, stepped MgO surfaces cause stronger binding of C₂H₂ to the nanoparticles. This is followed by the Mo-doped MgO and lastly, the pristine MgO surface. Although, the weakest adsorption of C₂H₂ on a Cu nanoparticle seems to be that which is on the Mo-doped MgO surface. In addition, adsorption of C₂H₂, in almost all cases, occurs on the edges of the nanoparticles. From the electronic and charge point of view, firstly, prior to C₂H₂ adsorption, charge depletion on the surface and accumulation on the nanoparticle in all cases is very apparent. Therefore, transfer of charge happens from the surface to the nanoparticles. Seemingly, C₂H₂ adsorbs onto charge accumulated areas of the nanoparticles where it can accept charge. Accepting electrons from the nanoparticle, imparts upon C₂H₂ a Lewis acid nature and on the adsorbent part of the nanoparticle that of a Lewis base which increases the binding energy [214].

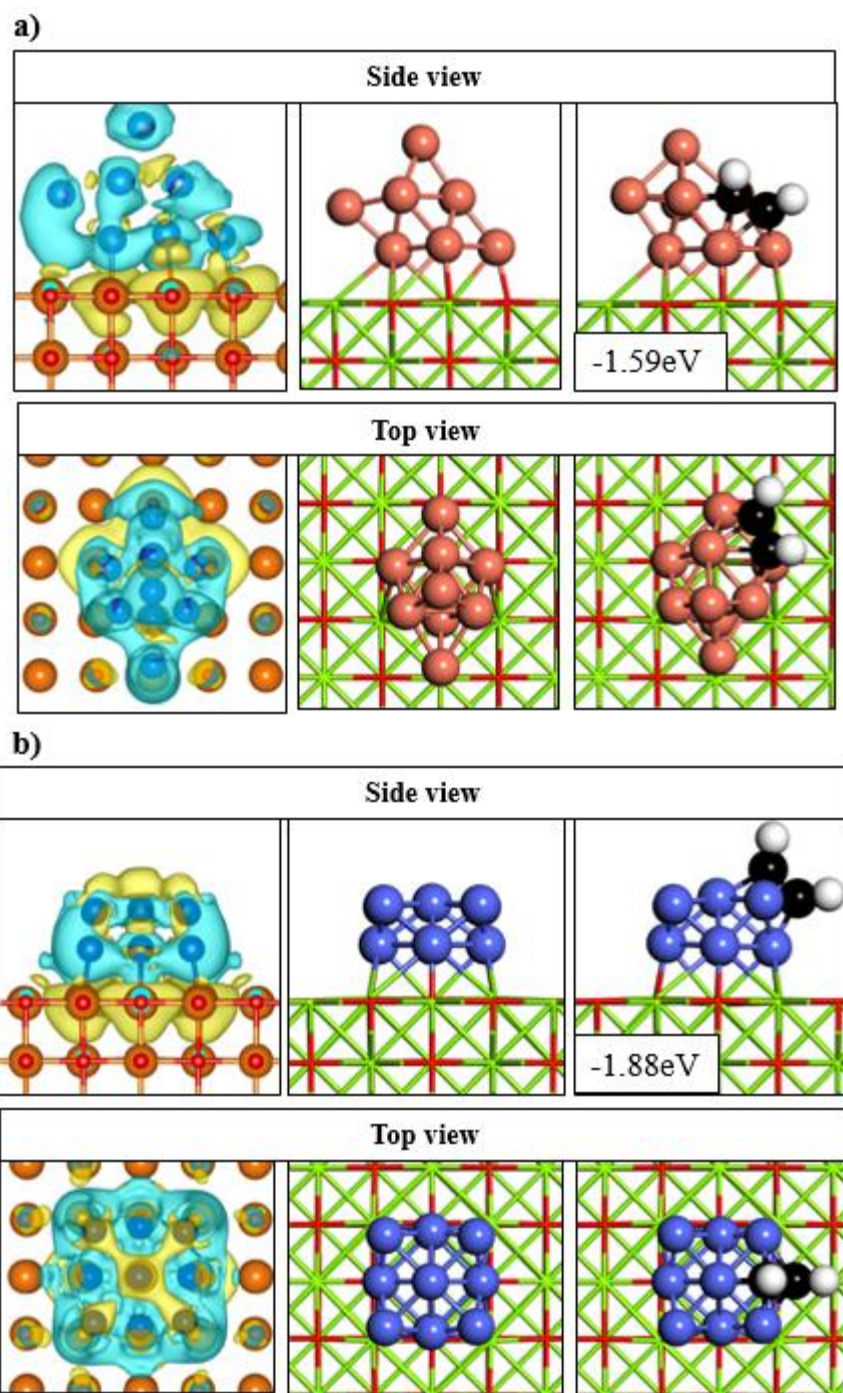


Figure 6.6 Side and top views of before and after C_2H_2 adsorption on a) Cu and b) Co, nanoparticles on pristine MgO (100) (shown in green (Mg) and red (O) sticks). Adsorption energies are also indicated. Charge density difference maps (isosurface level= $0.001 e/\text{\AA}^3$) before adsorption are also shown. Blue and yellow areas indicate accumulation (negative) and depletion (positive) of charge.

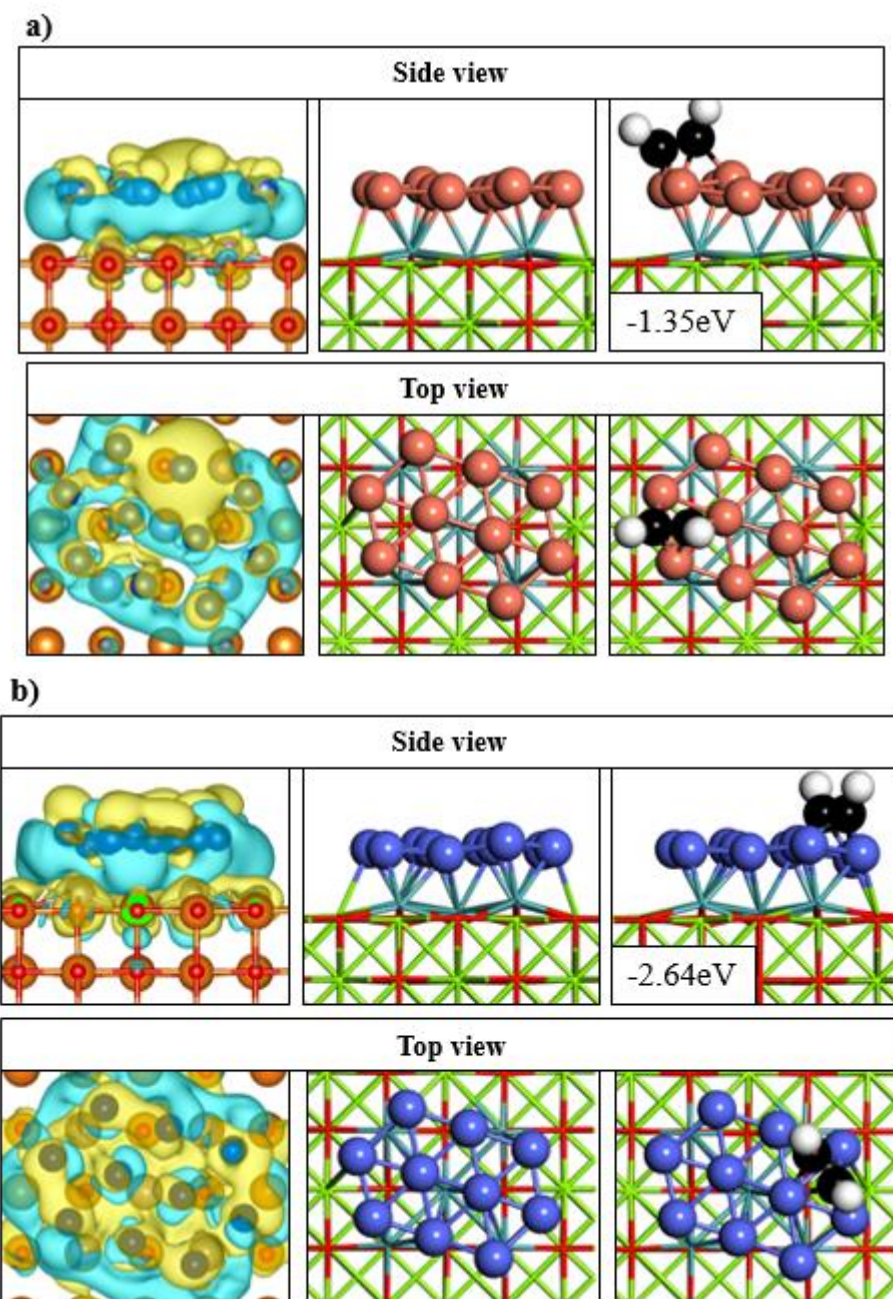


Figure 6.7 Side and top views of before and after C_2H_2 adsorption on a) Cu and b) Co, nanoparticles on Mo-doped MgO (100) (shown in blue (Mo), green (Mg) and red (O) sticks). Adsorption energies are also indicated. Charge density difference maps (isosurface level= $0.001 e/\text{\AA}^3$) before adsorption are also shown. Blue and yellow areas indicate accumulation (negative) and depletion (positive) of charge.

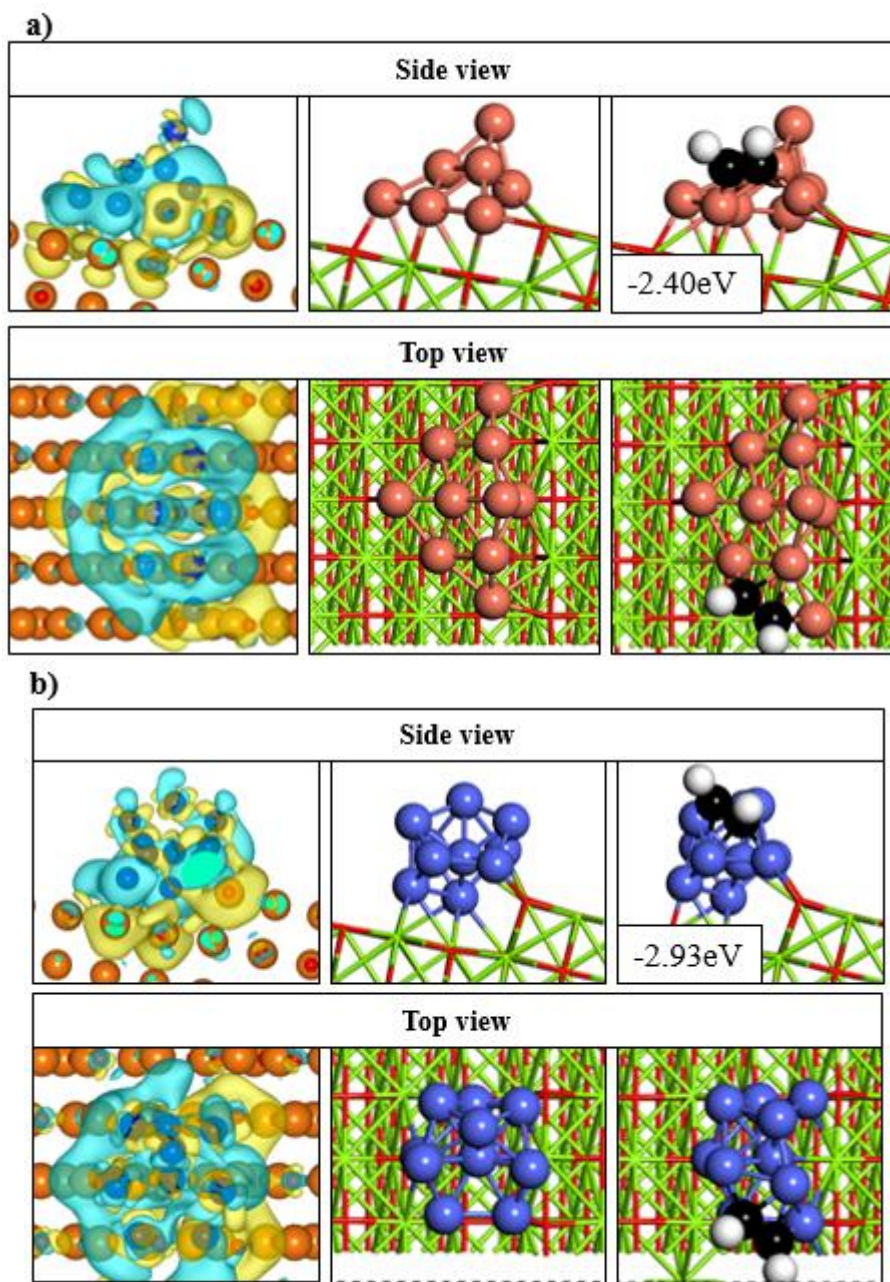


Figure 6.8 Side and top views of before and after C_2H_2 adsorption on a) Cu and b) Co, nanoparticles on Stepped MgO (i.e. MgO (105)). Charge density difference maps (isosurface level= $0.001 e/\text{\AA}^3$) before adsorption are also shown. Blue and yellow areas indicate accumulation (negative) and depletion (positive) of charge. Adsorption energies are also indicated.

6.4.1.3.2. C_2H_2 Dehydrogenation ($C_2H_2 \rightarrow CCH + H$)

NEB calculations were performed to find the energy barrier for the dehydrogenation of C_2H_2 on the Cu and Co nanoparticles adsorbed to the MgO surfaces. Between 3 to 5 images were used for the calculations. Prior to calculations, final configurations which involve the co-adsorption of CCH and H were identified by testing all possible co-adsorption sites. Results of the NEB calculations are shown in **Figure 6.9**. Initial, transition and final images can be found in **Appendix D (Figures D1-D3)**. Dehydrogenation of C_2H_2 has a consistently higher activation energy barrier on the Cu nanoparticles than on Co nanoparticles. Energy barriers for dehydrogenation on both nanoparticles are considerably reduced by Mo-doping of the MgO surface. In addition, configurations resulting from dehydrogenation show that the dissociation products CCH and especially H are drawn to the edges of the nanoparticles and close to the nanoparticle-support interface. However, larger nanoparticles would be needed to draw definitive conclusions in this regard.

6.4.1.3.3. C_2H_2 C-C Bond Scission ($C_2H_2 \rightarrow CH + CH$)

Energy barriers for the CH-CH bond breakage in C_2H_2 were also found from NEB calculations and are depicted in **Figure 6.9**. Initial, transition and final images can be found in **Appendix D (Figures D4-D6)**. On both nanoparticles, energy barrier for breaking of the CH-CH bond in C_2H_2 is clearly higher than for dehydrogenating it. However, while Mo-doping reduces the barrier for CH-CH bond breakage on Co, the effect is opposite on the Cu nanoparticle. This can be attributed to the raising of a Cu atom and its bridging between the two CH species during the CH-CH bond breakage

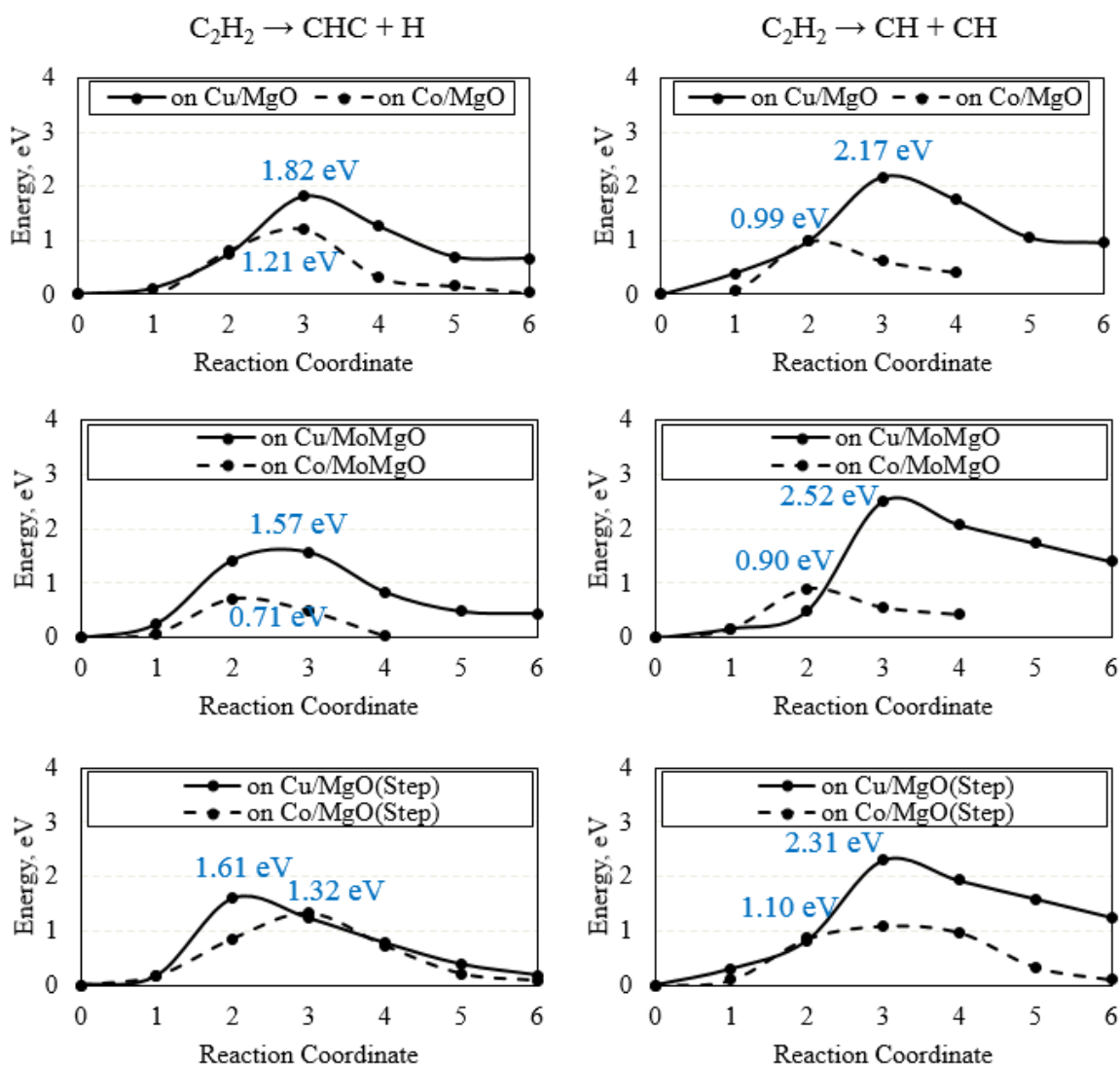


Figure 6.9 Energy profiles of left) $C_2H_2 \rightarrow CHC + H$ and right) $C_2H_2 \rightarrow CH + CH$ reactions happening on Cu and Co nanoparticles on the three MgO surfaces of study. Activation energy barriers are indicated in blue. The reaction coordinate has arbitrary units and is equivalent to the number of images used in NEB calculations.

(seen in **Figure D5a** of **Appendix D**). This Cu bridging feature is also seen in the literature [114] and in Chapter 5 on the flat surface of Cu in the presence of adsorbed C atoms. CH-CH bond breakage on Cu nanoparticles is also more considerably

endothermic than on Co nanoparticles. An important observation here is that the CH species resulting from the CH-CH bond breakage on the 3D nanoparticles, position most favorably along the edges of the nanoparticles and closer to the support. This has implications on nanotube growth where the cap may nucleate from these nanoparticle edges and begin to form the curved nanotube cap.

6.4.2. Part 2

In Part 2, it is assumed that the C precursor gas has dissociated and only C atoms are available.

6.4.2.1. Carbon Dissolution/Interaction in Unsupported Nanoparticles

The initial nanoparticle models, constructed in Materials Studio [135] consist of 38-atom (taken from the face-centered cubic crystal), 55-atom (taken from the icosahedral crystal), and 68-atom (taken from the *fcc* crystal) unsupported nanoparticles of Cu and are shown in **Figure 6.10**. The diameter of these nanoparticles are estimated as 0.8, 1, and 1.1 nm. All initial structures were relaxed. For each nanoparticle, C atoms were sequentially added to octahedral sites. The structures were allowed to relax after each addition of C. The interaction energy of C with the nanoparticle was calculated and

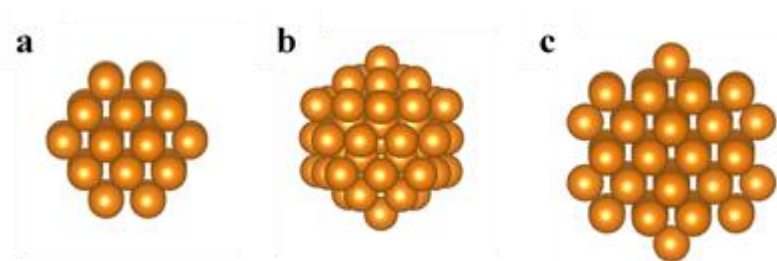


Figure 6.10 Initial structures of Cu nanoparticles: a) 38-atom *fcc*, (b) 55-atom icosahedral, and (c) 68-atom *fcc*.

normalized by subtracting both the energies of n C atoms (each individual C having an energy of E_C) and the nanoparticle without any C (E_M) from the total energy of the system (E_{MC_n}) and dividing by the total number of C's added (n):[215]

$$E_{int} = \frac{E_{MC_n} - (nE_C + E_M)}{n} \quad (6.4)$$

Carbon atoms were added in sequence to the 38-, 55-, and 68-atom relaxed nanoparticle models explained earlier. At each addition step, a single C atom was placed in an available octahedral position, and the system was relaxed. As such, for each addition step all possible positions were tested and the most thermodynamically favorable C location was chosen. **Figure 6.11** shows the resulting interaction energy, calculated from **Equation 6.4**, of each added C to the Cu nanoparticles studied here. Overall, the energy of interaction is negative, *i.e.* the addition of C atoms decreases the energy of the nanoparticle, which implies increased adsorption strength. However, with the addition of more C atoms, the graph shows an overall increase in energy. This rapid change in the rate of adsorption, which becomes weaker, indicates low C solubility in Cu nanoparticles.

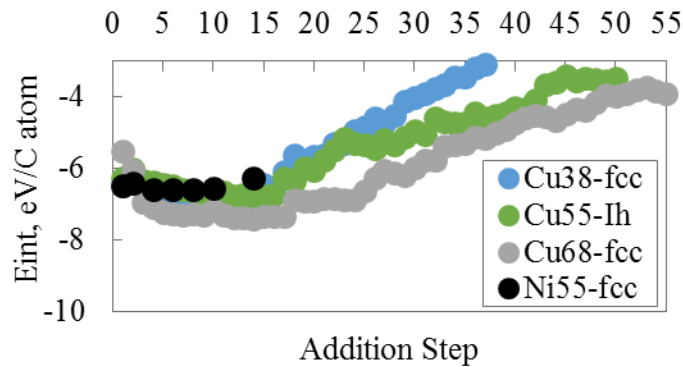


Figure 6.11 Energy of interactions for the successive addition of C atoms into 38-, 55-, and 68-atom Cu nanoparticles compared to 55-atom Ni nanoparticle.

The number of C atoms added before the steep incline in interaction energy hint at an approximate composition of Cu_xC , where $x > 3$. Note that M_3C is a typical composition of a stable or at least metastable metal (M) carbide such as Fe_3C , cementite.

A closer look into the mechanisms of C incorporation into carburized Cu nanoparticles reveals other interesting features. Focusing first on the 38-atom Cu nanoparticle, upon the addition of the 10th C atom, a C–C dimer forms on the surface. The aforementioned sudden increase seen in the interaction energy (**Figure 6.11**) is attributed to the formation of this dimer. The number of dimers forming within the nanoparticle increases gradually (**Figure 6.12**) until the 18th C addition. From this point until the 23rd C addition, no new C dimers are formed, and the nanoparticle is being covered with C atoms (**Figure 6.12**). In **Figure 6.11**, this period (18th to 23rd addition) is seen as a drop in the interaction energy, and it is therefore thermodynamically favorable. The effect of these dimer bonds on the overall interaction energy is not negligible and has therefore been accounted for in the interaction energy calculation. The addition of C atoms is continued until no octahedral sites are found. At this point, many dimers are visible on and within the nanoparticle (see **Figure 6.12**). Approximately 88% of the total C atoms remain on or in the immediate subsurface of the nanoparticle despite being initially placed in octahedral positions inside the nanoparticle. This is in agreement with the well-known fact that the dissolution of C in Cu is very low and interactions of Cu with C are surface-driven. Similar events take place on the 55-atom Cu nanoparticle. The first dimer appears upon the addition of the 10th C at which point the energy of interaction rises slightly. However, the magnitude of the interaction energies shows that

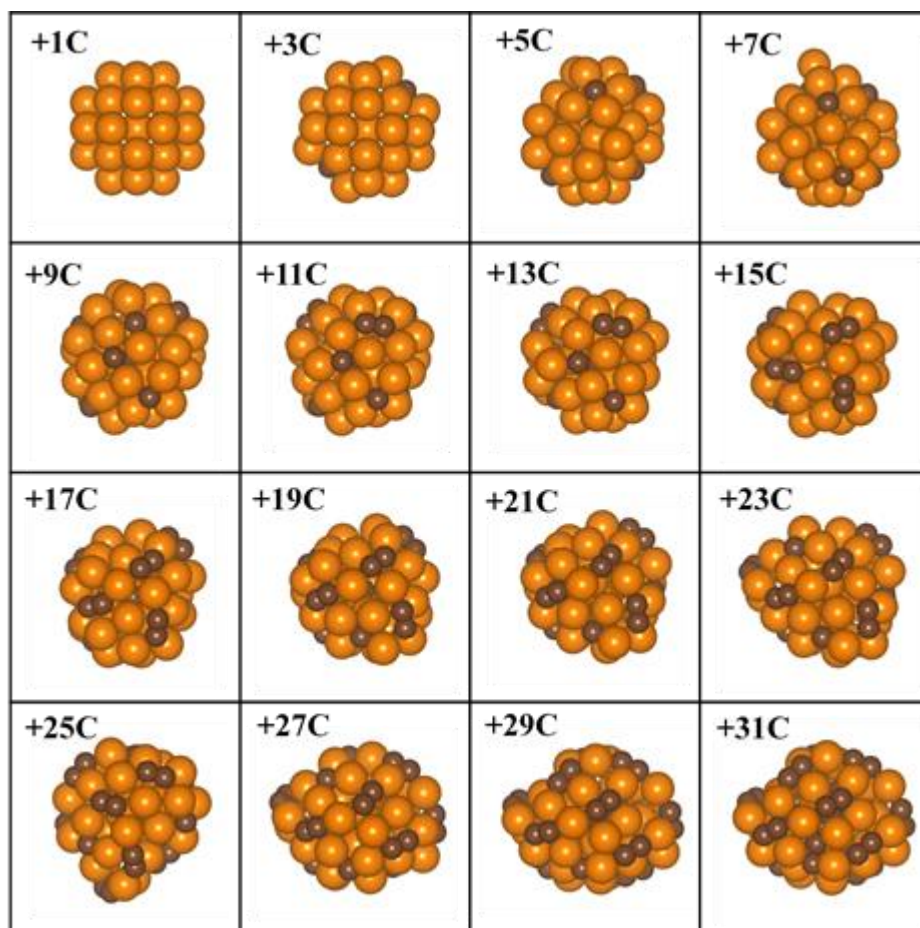


Figure 6.12 Gradual carburization and structure distortion of the un-supported 38-atom Cu nanoparticle. C atoms are in brown. For “+1C”, the single C atom is at the center of the nanoparticle and is hidden from view.

compared to the 38 *fcc* structure, dimers are less likely to form for this structure of Cu nanoparticle. In fact, from the 10th to the 15th addition very few dimers are formed. However, after the 15th addition, more dimers are adsorbed and the interaction energy increases sharply. Finally, in the 68-atom Cu nanoparticle, the first dimer appears at the 10th C addition. The stair-wise interaction energy trend for this nanoparticle is similar to that of 38 atom *fcc*, and dimers are likely to be formed as in the 38 atom *fcc* structure. More than 85% of dimers formed in all three nanoparticles are largely located on the

surface of the nanoparticles. These results indicate that C atoms interacting with unsupported Cu nanoparticles of various sizes tend to form dimers and remain on the surface rather than diffuse into the bulk of the nanoparticle. Therefore, it is emphasized that the interaction energies reported in **Figure 6.11** are not representative of C solubility.

Figure 6.11 also shows the energies of interaction corresponding to C atom additions into a 55-atom Ni nanoparticle, as reported by Gomez-Ballesteros and Balbuena [216]. The energy of interaction for the 55-atom Ni is well in the range for that of the 38-, 55-, and 68-atom Cu nanoparticles. However, for the 55-atom Ni nanoparticle, a total of 14 C atoms were added to the nanoparticle, and therefore, further comparisons with the Cu nanoparticles was not feasible. Beyond the energy of interaction, major differences are seen in the interactions of these two nanoparticles (Cu and Ni) with C. First, the structure of the Cu nanoparticle is distorted (see **Figure 6.12**) with each addition of a C atom, while the Ni nanoparticle remains well intact at least for the 14 atoms of C that it has accepted. Second, this structural distortion within the Cu nanoparticle helps C atoms to roam and bond with other C atoms, especially on the surface. This may imply large surface diffusion rates of C atoms on Cu nanoparticles. These observations have also been noted for graphene growth on Cu(111) and Ni(111) [161]. The ability of Cu to form good quality graphene sheets is attributed to the high mobility of surface Cu atoms. It may be argued that interaction energies for Cu are well in the range of those for Ni, while Ni is known to have high C solubility especially for smaller nanoparticle sizes [217]. It is noted that interaction energies reported here for Cu

are by no means representative of solubility since the majority of the incorporated C atoms actually relax to the surface rather than being dissolved below the subsurface.

6.4.2.2. MgO-Supported Cu Nanoparticles

Two different sizes (32- and 38-atoms) of Cu nanoparticles supported by MgO substrate are studied. Two facets of MgO were studied; the (100) and oxygen-terminated (111) facet. In each case, the nanoparticle was positioned on the MgO substrate and allowed to relax. After relaxation, the same procedure of adding C's as in unsupported nanoparticles was repeated here. The interaction energy of C with the structure was calculated and normalized by subtracting the sum of n C atoms and the energy of the supported nanoparticle without any C ($E_{M/MgO}$) from the total energy of the system ($E_{MC_n/MgO}$):

$$E_{int} = \frac{E_{MC_n/MgO} - (nE_C + E_{M/MgO})}{n} \quad (6.5)$$

The changes in adhesion energy between the MgO surface and the nanoparticle with each addition of C atoms was also explored. Single-point calculations were conducted on the surface (E_{MgO}) and the nanoparticle (E_{MC_n}) individually. These energies were summed up and subtracted from the total energy of the system:

$$E_{adh} = \frac{E_{MC_n/MgO} - (E_{MC_n} + E_{MgO})}{n} \quad (6.6)$$

The adhesion energy of the graphene fragment to the carburized Cu nanoparticle was calculated by subtracting the sum of the energies of the carburized nanoparticle and the graphene fragment from the total energy of the nanoparticle– graphene system.

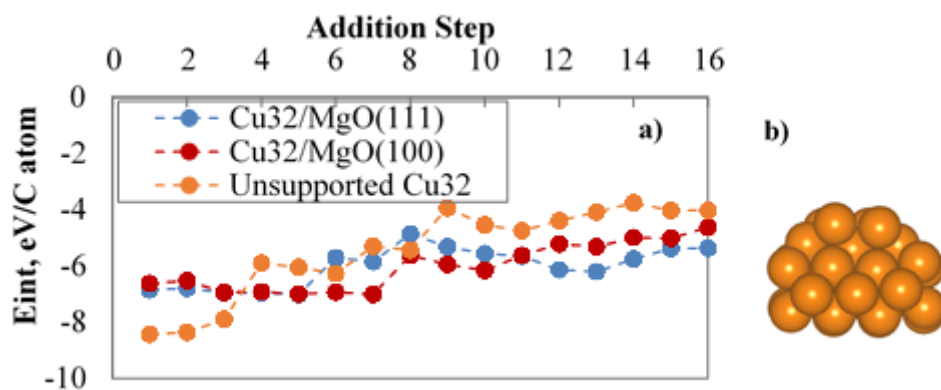


Figure 6.13 a) Energy of interaction for the successive addition of C atoms into 32-atom Cu nanoparticles: unsupported and supported on MgO(100) and MgO(111) and b) the 32-atom Cu nanoparticle used on the MgO supports.

6.4.2.2.1. Supported 32-Atom Cu Nanoparticle

Figure 6.13 shows the energy of interaction calculated from **Equation 6.5** for MgO-supported carburized 32-atom Cu nanoparticle compared to that of the unsupported. The initial geometry of the nanoparticle is also illustrated in **Figure 6.13**. As mentioned earlier, two different MgO facets of (100) and OH-terminated (111) were studied. In all cases, the interaction energy resulting from the addition of a C into the system is negative, and therefore, the addition of C atoms into the system is thermodynamically favorable. This energy increases (i.e., the C adsorption becomes weaker) after a certain amount of C atoms has been added to the system. This abrupt increase in energy is again due to the formation of dimers on the surface and inside the carburized Cu nanoparticle. The formation of a dimer within the Cu nanoparticle happens on the unsupported nanoparticle the earliest (i.e., with less C atoms), and then on the MgO(111) support, followed by that on the MgO(100) support, as revealed by the energy trend in the intermediate range. Also, the energy of interaction remains more favorable for further C

addition for the Cu nanoparticle supported by MgO(111) than by MgO(100). Therefore, in terms of C–C bonding and C interaction with supported Cu nanoparticle, the OH-terminated MgO(111) seems to be a better option.

6.4.2.2.2. Supported 38-Atom Cu Nanoparticle

Figure 6.14 shows the same type of analysis as for **Figure 6.13** but for the 38-atom Cu nanoparticle (initial geometry depicted in **Figure 6.10a**). Note that the geometry of the 32-atom Cu nanoparticle is different from that of the 38-atom Cu nanoparticle; the 38-atom Cu is rounded, while the 32-atom is nearly hemispherical and was placed on the support from the flatter side. As in the supported 32-atom Cu nanoparticle, carburizing the supported 38-atom Cu nanoparticle is energetically favorable. Here also, C atoms within the Cu nanoparticle supported by MgO(111) form dimers earlier (with less C atoms) than that supported by MgO(100). Thus far, comparing **Figures 6.13** and **6.14** shows that the supported rounder 38-atom Cu nanoparticle is slightly more favorable for carburization on the basis of stronger energy of interaction ranges. Nevertheless, bonding and formation of dimers take place with fewer C atoms in the 32-atom Cu nanoparticle than in the 38-atom. Also, with respect to C atom locations, the MgO(111) support allows approximately 94% of incorporated C atoms to remain on the surface of the Cu nanoparticle, while the MgO(100) allows a lesser percentage of approximately 80%. This may also explain why interaction energies for C addition to systems with MgO(111) switch from less favorable in the intermediate region to more favorable toward later addition steps. For MgO(100) supported Cu nanoparticles, the support–nanoparticle interface strongly dictates the position of Cu

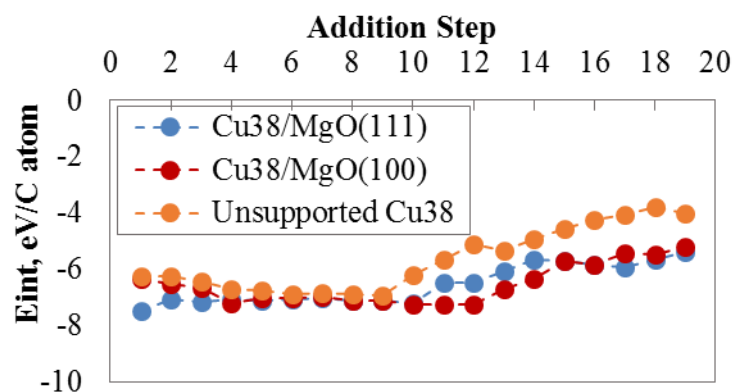


Figure 6.14 Energy of interaction for the successive addition of C atoms into unsupported, MgO(100) and MgO(111) supported 38-atom Cu nanoparticles.

atoms and subsequently the position of C atoms. For this facet of MgO, added C atoms appear to be located at considerably greater distances from the interface than in the case of the (111) facet. This leaves less space available for additional C atoms, translating to less favorable interaction energies than for the (111) facet, as described further in the following section.

6.4.2.2.3. Adhesion Energy between Carburized Cu Nanoparticles and MgO Support

Figure 6.15 shows the averaged distance of the closest Cu and C atoms to the MgO support for all supported carburized Cu nanoparticles. These results indicate that Cu atoms of nanoparticles supported by MgO(100) are slightly more distanced from the support compared to those supported by MgO(111). This distance from the support is even greater for C atoms in the nanoparticles supported by MgO(100) compared to those supported by MgO(111). It is also observed that the Cu nanoparticle adheres to the MgO(100) support only via Cu–O bonds, whereas on MgO(111) this bonding is switched to Cu–H.

	Cu distance to support, Å	C distance to support, Å
$\text{Cu}_{32}\text{C}_{16}/\text{MgO}(100)$	2.04	3.61
$\text{Cu}_{32}\text{C}_{16}/\text{MgO}(111)$	1.90	1.92
$\text{Cu}_{38}\text{C}_{19}/\text{MgO}(100)$	1.98	3.50
$\text{Cu}_{38}\text{C}_{19}/\text{MgO}(111)$	1.85	1.95

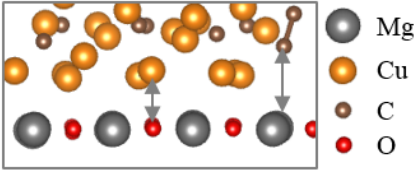


Figure 6.15 Average distance of closest Cu and C atoms to MgO support for all four carburized Cu nanoparticle and support cases. C atoms in both 32- and 38-atom Cu nanoparticles supported by the MgO(111) support are closer to the support compared to the nanoparticles supported by MgO(100) (illustrated in the image to the right).

Pacchioni and Rösch reported that Cu–O bonding is weaker than Ni–O bonding of metal nanoparticles on MgO(100) supports and that metal–metal bonds are stronger than such metal–oxygen bonds [218]. However, as discussed above, formation of dimers is delayed when the Cu nanoparticle is supported by MgO. Then, the adhesion of the Cu nanoparticle to the support is an aspect to study and is likely to be affected during carburization, as shown in **Figure 6.16**. The negative energy values reveal that adhesion is more favorable as the particle becomes carburized. For the smallest nanoparticle at the first stages of carbon addition, the adhesion is far better on the MgO(111) than on the MgO(100). As the nanoparticle accepts further C atoms, the adhesion energies on both substrates become relatively close, but the adhesion remains slightly more favorable for the MgO(111) support. **Figure 6.16** also shows that for the much rounder 38-atom Cu nanoparticle except for slight differences in the earliest stages of C addition, adhesion energies are very similar for both types of MgO supports. The difference in early stages is expected since the 38-atom nanoparticle is adhered to the support by a smaller area

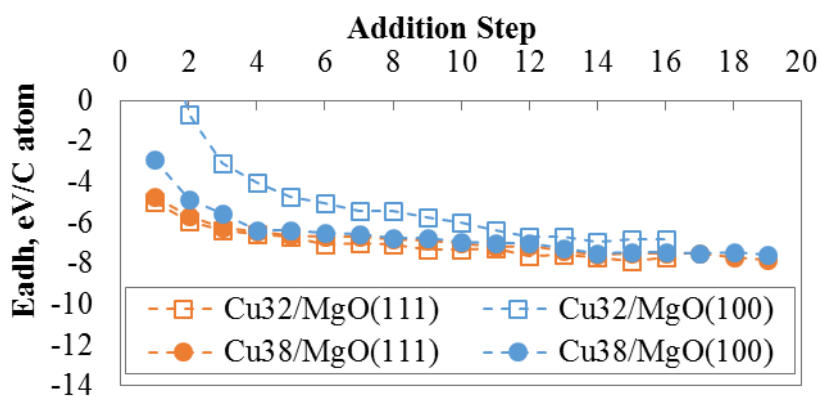


Figure 6.16 Energy of adhesion of the carburized 32- and 38-atom Cu nanoparticles to MgO(100) and MgO(111) supports during successive C atom additions. Adhesion of the Cu nanoparticles to the MgO(111) is greater, and in agreement with Figure 6.15.

composed by the lower four Cu atoms of the nanoparticle, whereas the hemispherical 32-atom nanoparticle is adhered to the support by the flat nanoparticle side consisting of eight Cu atoms. Thus, the larger contact area is more affected by the structure and chemical nature of the support exposed facet. In addition, **Figure 6.16** also implies that the adhesion of carburized Cu nanoparticles on MgO(100) supports is weaker than on MgO(111), which is in agreement with the findings in **Figure 6.15**. In total, the OH-terminated MgO(111) supported 38-atom Cu nanoparticle is the most energetically favorable in terms of carburization and adhesion energy.

6.4.2.3. Adhesion of Graphene Fragment to Carburized Supported Cu Nanoparticles

To gain some insight into the energetics of a nascent nanotube cap formed on a carburized Cu nanoparticle, a graphene fragment was placed in contact with the supported carburized Cu nanoparticles. A similar study was conducted by Silvearv et al

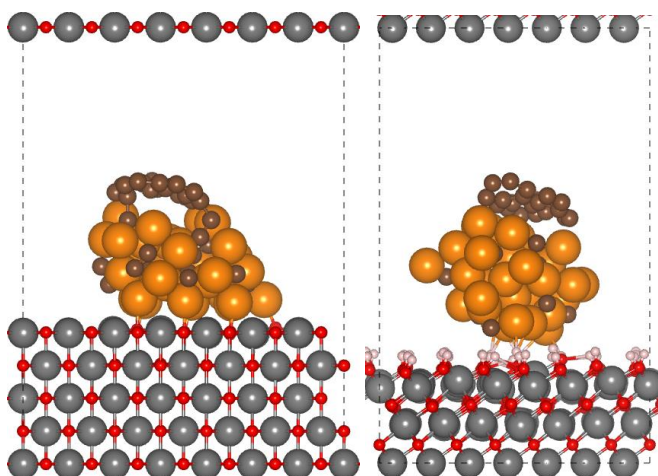


Figure 6.17 (a) Image of graphene fragment adhering to the MgO(100) supported carburized 32-atom Cu nanoparticle. (b) Image of graphene fragment adhering to the MgO(111) supported carburized Cu nanoparticle.

[207] where CNTs were brought into contact with various transition metal nanoparticles including Cu, although in that work the metal nanoparticles were not carburized prior to contact with CNTs. The analysis of previous sections have shown a large number of incorporated C atoms to be relaxed on the surface, mediating formation of C dimers and networks that can facilitate nascent CNT formation. **Figure 6.17** illustrates the geometry-optimized configuration of a graphene fragment adhered to the carburized 32-atom Cu nanoparticle supported by MgO. The graphene fragment consists of five six-membered rings of C atoms. This geometry is initially relaxed with a DFT optimization.

Table 6.2 lists the adhesion energies. The greatest support– nanoparticle adhesions belong to the supported 32-atom Cu, due to the larger and flatter contact area (8 Cu atoms) in contact with the support. However, the greatest graphene–nanoparticle adhesions are for the supported rounder 38-atom Cu, especially for MgO(111) supported carburized Cu. This implies that if the graphene fragment is assumed a cap and a

Table 6.2 Adhesion energies between graphene fragment and cluster (carburized nanoparticle) and between support and cluster for all four cases of supported carburized Cu nanoparticles. All energies in eV.

	graphene/cluster	support/cluster
Cu ₃₂ C ₁₆ /MgO(100)/graphene	-11.0	-8.9
Cu ₃₂ C ₁₆ /MgO(111)/graphene	-7.6	-8.7
Cu ₃₈ C ₁₉ /MgO(100)/graphene	-10.6	-6.7
Cu ₃₈ C ₁₉ /MgO(111)/graphene	-15.4	-5.3

precursor to nanotube growth, then the cap will adhere with greater strength to the rounder (38-atom) carburized Cu nanoparticle than to the hemispherical (32-atom) carburized Cu nanoparticle. While the rounder nanoparticle adheres strongly to the cap, it adheres weakly to the support. Note that in the previous section it was found that the round-shaped 38-atom Cu nanoparticle supported by MgO(111) was also the most favorable for carburization.

6.4.2.4. Charge Density of Carburized Supported Cu Nanoparticles

Figure 6.18 shows charge density differences obtained using the Bader charge analysis. These isosurfaces have been plotted at a density of 0.001 e/Å³. Charge density differences show charge depletion and accumulation areas. Charge density differences for carburized supported Cu nanoparticles before and after graphene placement are respectively calculated by:

$$\Delta\rho_{CuCMgO} = \rho_{CuCMgO} - \rho_{CuC} - \rho_{MgO} \quad (6.7)$$

$$\Delta\rho_{CuCMgOgraphene} = \rho_{CuCMgOgraphene} - \rho_{CuCMgO} - \rho_{graphene} \quad (6.8)$$

where ρ_{CuCMgO} , ρ_{CuC} , ρ_{MgO} , $\rho_{CuCMgOgraphene}$, and $\rho_{graphene}$ are charge densities of carburized MgO-supported Cu NP, carburized MgO-supported Cu NP

excluding the support, carburized MgO-supported Cu NP excluding the Cu NP, carburized MgO-supported Cu NP with the graphene, and graphene.

As seen from the figure, ions in the oxide surface affect the adjacent metal atoms, and the adjacent metal atoms experience opposite charge toward the oxide surface. This behavior has also been reported for alumina-supported metal nanoparticles [219]. Accumulation of charge is shown in blue and can be seen predominantly at the lower region of the cluster in the vicinity of the surface for all four cases of **Figure 6.18(a)–(d)** and before the addition of any C atoms to the cluster. Charge depletion is seen in yellow and mostly on the surface of the supports, *i.e.* charge is transferred from the support surface to the nanoparticle. With the addition of 16 C atoms, the charge distribution remains localized on the surface but involves a somewhat wider region, showing more interaction with the MgO surface. Compared to MgO(100) surface, the MgO(111) surface is more reactive and areas with charge accumulation/depletion are wider. The accumulation of electrons in the cluster in the vicinity of the surface is greater than in the MgO(100) case. In general, as expected, the electronic structure of the Cu nanoparticle appears to be modified by the metal–oxide (MgO) support. The interaction occurs within the first few layers of the cluster and metal–oxide interface. Charge transfer between the nanoparticle and the MgO support can affect the catalytic activity of the Cu nanoparticle [4, 220].

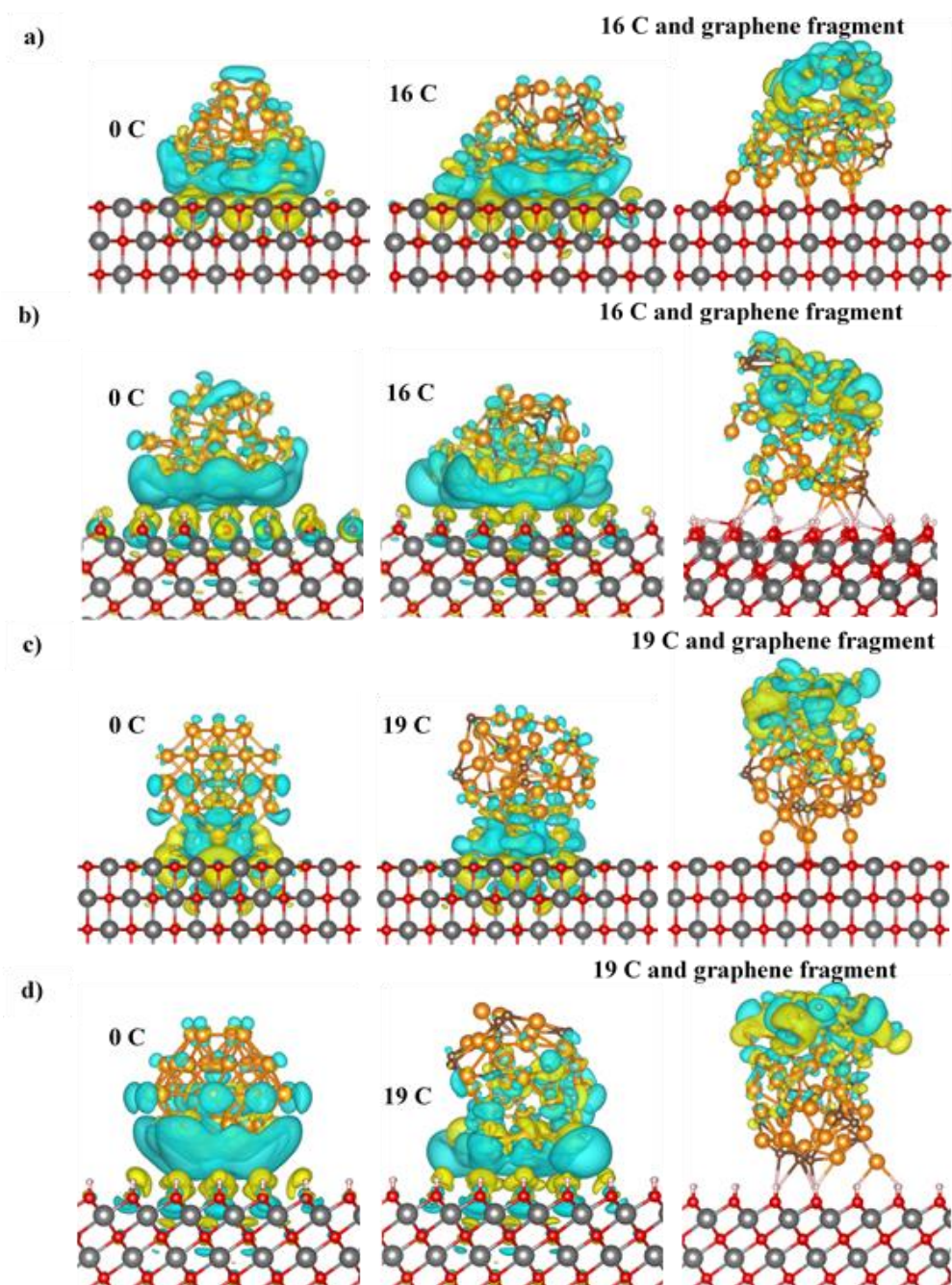


Figure 6.18 Charge density difference analysis before and after carburization and addition of graphene fragment for (a) MgO(100) supported 32-atom Cu, (b) MgO(111) supported 32-atom Cu, (c) MgO(100) supported 38-atom Cu, and (d) MgO(111) supported 38-atom Cu. Blue and yellow colors represent negative (accumulation) and positive (depletion) charge densities, respectively. Isosurface level = $0.001 \text{ e}/\text{\AA}^3$.

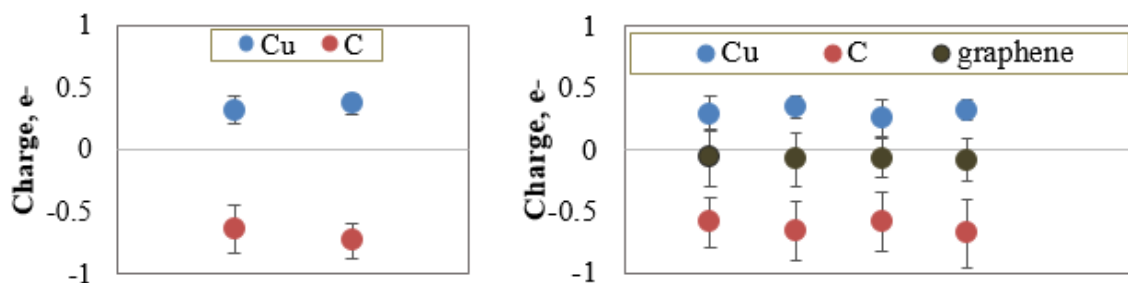


Figure 6.19 Average partial atomic charges of the left) carburized unsupported 32- and 38-atom Cu nanoparticles and right) Cu nanoparticle, C atoms, and the graphene fragment in contact with the nanoparticle. Charge transfer is greater for supported Cu nanoparticles, especially among the carbons and graphene fragment.

6.4.2.5. Bader Charge Analysis

The analysis of charges is summarized in **Figure 6.19** for unsupported and supported carburized Cu nanoparticles. Standard deviation of charges and therefore charge variations are also shown in these figures. For unsupported Cu nanoparticles, the average partial atomic charges for Cu and C in the nanoparticles are $0.34e^-$ and $-0.68e^-$, respectively. The average partial charge for Cu atoms in the supported nanoparticles for all four cases is similar and approximately $0.3e^-$, while the partial charge for the C atoms within and on the Cu nanoparticle varies significantly and averages at $-0.63e^-$. The variation in partial charges on C atoms within the graphene fragment is also large but averages at a slightly negative value of $-0.07e^-$. A comparison of the unsupported and supported reveals that the changes in charge transfer caused by supporting the carburized Cu nanoparticles and allowing contact with a graphene fragment are not significant. This observation points at the weak electrostatic interaction between the support and the Cu nanoparticle as well as between Cu and C atoms. Therefore, the large adhesion energies between the graphene fragment and carburized Cu

nanoparticles observed in the previous section are not driven by electrostatic interactions but rather due to covalent interactions.

6.5. Conclusions

DFT calculations were used to study the effect of Mo on the adsorption of Cu and Co atoms and nanoparticles on the MgO surface. In comparison, Co atoms and nanoparticles bind stronger to the MgO (100) surface. Mo doping of MgO surface strengthens the adsorption of both Co and Cu nanoparticles to the MgO surface. Mo also seems to change the crystal structure of Co nanoparticles on the MgO surface. Moreover, adsorption and dissociation (dehydrogenation and C-C bond breakage) of C_2H_2 on Cu and Co nanoparticles on pristine, stepped and Mo-doped MgO surfaces were also investigated. Results consistently show that activation energy barriers for both dehydrogenation and C-C bond breakage of C_2H_2 on Co nanoparticles on the three types of MgO surfaces studied, are lower than those on Cu nanoparticles. Mo doping of the MgO surface reduces the energy barriers for both the dehydrogenation and CH-CH bond breakage of C_2H_2 on Co nanoparticles. However, for Cu nanoparticles, Mo-doping increases the energy barrier for CH-CH bond scission. Therefore, as a general conclusion, the role of Mo is that of enhancing the binding of nanoparticles to the support and aiding in the dissociation of C_2H_2 .

DFT simulations were carried out to also study the energetics of carbon incorporation into various sizes of unsupported and MgO-supported Cu nanoparticles. For the unsupported nanoparticles, a significant number of carbon atoms tended to locate at the surface of the Cu nanoparticle, giving rise to surface diffusion and the formation of dimers that are precursors of carbon networks necessary for the onset of graphene or

carbon nanotube cap formation. In contrast to the well-known behavior observed in traditional non-noble catalysts such as Co and Ni, a very small amount of the incorporated carbon atoms remain inside the nanoparticle. Similar behavior is detected during the incorporation of carbon into the MgO-supported Cu nanoparticles. Two morphologies of the Cu nanoparticle, hemispherical and round, and two facets of MgO, MgO(100) and MgO(111), were studied. The structure and chemistry of the support exposed facet affects the carburization of the Cu nanoparticle inducing changes in the catalyst nanoparticle shape that results in changes of the adhesion energy and in the capacity to incorporated carbon atoms into the subsurface. The adhesion of the carburized Cu nanoparticle to the MgO(100) support is found to be weaker than that on the MgO(111) facet. Carbon atoms incorporated within the MgO(100)-supported Cu nanoparticle clearly locate at a further distance from the support than those incorporated within the MgO(111)- supported Cu nanoparticle. As for the effect of Cu nanoparticle shape, formation of dimers happens with less carbon atoms in the hemispherical Cu nanoparticle than that in the round, making the energetics of carbon incorporation into the rounder Cu nanoparticle slightly more thermodynamically favorable. Finally, contact of a graphene fragment with all four cases of supported carburized Cu nanoparticle was tested. Greater adhesion of graphene fragment to CuC cluster was seen for the round cluster on either of the supports. Comparing the two clusters, the curved geometry of the round cluster results in stronger adhesion to the graphene fragment and weaker to the support, whereas the hemispherical cluster adheres stronger to the support and weaker to the graphene fragment. Therefore, Cu nanoparticles would be favorable for growth of

single-walled carbon nanotubes, provided the appropriate combination of catalyst nanoparticle shape/support provides the necessary geometry of the exposed catalyst surfaces. It is also noted that such “template effect” of the catalyst would also be crucial to achieve some effects on the chirality of the nascent tubes. Moreover, in supported Cu nanoparticles, nanoparticle–support adhesion energies indicate weak Cu–O bonding that allows the nanoparticle to remain nearly spherical on the support. In turn, this may facilitate the separation of the nanoparticle from the support, once the SWCNT has formed.

7. CONCLUSIONS AND FUTURE DIRECTIONS

The growth of graphene and CNT involves many different parameters such as temperature, pressure, C precursor gas type and composition, catalyst and catalyst support type and structure, and growth scheme, all of which may affect the resulting structure of these nanoscale materials in terms of their length, diameter and chirality of carbon nanotubes, and quality of the graphene films. The present study was set out to explore some of these aspects with special focus on Cu as the catalyst and with the aim of elucidating causalities of events and shedding light on some of the current unknowns of the processes.

The spatiotemporal scales at which C precursor gas dissociation on a catalyst occurs makes several microscopic details of this event currently undetectable by experimental settings. On the other hand, information regarding this event is crucial in understanding the first stages of nucleation and growth of graphene and CNT. This knowledge helps in defining the building blocks of these materials and leads to the understanding of the growth mechanism. Therefore, one of the goals (*goal i*) of this dissertation was to investigate the pathway with which the C precursor gas is converted into C atoms or species necessary for the C network, on the catalyst surface. To this end, in Chapter 3 the dissociation pathway of CH₄ was studied on the Cu (111) surface from the thermodynamics point of view. The energy barriers for all reaction pathways obtained through DFT calculations revealed competing pathways. For example, energy barrier for the hydrogenation of H atoms and their conversion to H₂ is comparable to the

energy barriers of CH_x dehydrogenation reactions. The results also revealed that compared to dehydrogenation reactions, hydrogenation reactions have a lower energy barrier. Therefore, kMC was then employed to account for such competing energy barriers and, in addition, the diffusion of species and temperature effects. The results of this integration of DFT energetics and kMC kinetics revealed that the dissociation pathway is very sensitive to temperature, pressure and the presence of gaseous H_2 in the feedstock gas. In fact, it was shown that adding H_2 to the feedstock gas directs the dissociation towards further dehydrogenation of CH_x species. This beneficial effect of H_2 in the feedstock gas along with CH_4 was explained by the high diffusion of H surface species and the slightly lower energy barrier towards forming H_2 and desorbing to the gas phase, thus depleting the Cu surface of H that would otherwise reverse the CH_x dehydrogenation reactions.

In Chapter 4, another aspect of *goal i – the effect of other species on C precursor gas dissociation pathway* – was addressed. To this end, the effect of surface oxygen as a common specie present in the CCVD method of graphene and CNT growth was studied. The case of Ni was studied alongside Cu as a comparison. Results showed that surface oxygen, even at high coverages, lowers the energy barriers of CH_4 dissociation reactions on the Cu (111) surface but increases those on the Ni (111) surface. This finding was explained by the higher electronegativity and basicity of surface O on Cu surface than on Ni, which activate acidic C-H bonds. However, results also showed that surface O can bond with atomic C to form CO or CO_2 and desorb to the gas phase. This process is ideal for the cleaning of the Cu surface of any residual C before growth. Therefore, it is

concluded that partially oxygenating Cu surfaces *prior to* graphene and CNT growth can promote C precursor gas dissociation, however the presence of O *during* growth may lead to the deprivation of the catalyst of the C atoms that it needs to form the C network.

In the topic of graphene growth, the presence of the aforementioned residual C leads to the formation of individual graphene islands each with their own unique orientations across the catalyst surface, resulting in a non-uniform graphene sheet. The second goal (*goal ii*) of this dissertation, addressed in Chapter 5 for a Cu catalyst, was to investigate how temperature may affect these individual islands and alleviate the problem of non-uniformity, as observed in thermal cycling treatment of graphene growth in experimental settings. Results obtained in this dissertation showed that owing to weak Cu-C bonding and the high mobility of C atoms and networks on the Cu surface, high temperatures indeed facilitate graphene islands in their rotations above the Cu surface. While at lower temperatures graphene islands form, eventually at high temperatures and at higher densities of graphene islands, i.e. where graphene islands are closer to one another, metal-bridging effect was observed whereby metal atoms, here Cu, form a bridge between graphene islands thereby unifying them during their rotations on the Cu surface.

Finally, in Chapter 6 and in relation to *goals i* and *iii*, the dissociation of another C precursor gas, C₂H₂, was studied on supported catalyst nanoparticles which is the common setting for CNT growth. Simultaneously, this Chapter also addressed *goal iii*, the effect of the support and support dopants in the dissociation of the C precursor gas. In experimental settings, the catalyst support surface is not particularly doped by Mo, but

rather Mo is a constituent of the catalyst precursors. Results in this study showed that Mo atoms are most thermodynamically likely to substitute Mg atoms of the top layer of the MgO surface. Since Mo is not detected in ESTEM images and post-processing analyses of the catalyst, this leads the most likely positioning of Mo atoms to be immediately under the catalyst nanoparticles. While the focus of this dissertation was Cu as the catalyst, Co was studied alongside as a comparison. First, with regards to C precursor gas dissociation, the dehydrogenation of C_2H_2 on Cu nanoparticles was found to have a lower energy barrier compared to its CH-CH bond scission. This was true for all three cases of the catalyst support MgO being pristine, stepped or Mo-doped. However, for Co, Mo-doping in particular, yields the lowest energy barrier for C_2H_2 dissociation. Second, with regards to the effect of Mo-doping, doping indeed lowers the energy barrier to the lowest amount for C_2H_2 dehydrogenation for both metal nanoparticles. It seems that the most energetically favorable scenario is the dehydrogenation of C_2H_2 in the presence of Mo, leading to the formation of CCH and H. Third, DFT calculations performed in this regard, showed that species (CCH and H) resulting from the dissociation of C_2H_2 , were more thermodynamically favorable to be located at the edges of a nanoparticle and its interface with the support. This is due to the strong charge transfer present in those regions. This implies that CNT nucleation may begin from this region and grow from thereon, as is observed in time-resolved ESTEM videos. Whether the nascent CNT expands outwards from this region (tangential growth mode), or extends to reach the top of the nanoparticle (perpendicular growth mode) would most probably be dictated by the faceting of the nanoparticle which itself is

dictated by the support and its influence on the nanoparticle. This faceting was also observed from the DFT calculations performed in this study. The dissolution of C in Cu nanoparticles was also studied and found to be very low. In fact, almost all C tend to migrate to or remain on the surface of a Cu nanoparticle. Formation of C dimers on Cu nanoparticles is also very common and thermodynamically likely. Lastly, a nascent graphene fragment in contact with a carburized Cu nanoparticle on MgO surface, reduces the Cu nanoparticle adhesion to the MgO surface.

Based on the work presented in this dissertation, several areas are identified for further study:

- The dissociation of CH_4 , results in the formation of CH_x species. According to the DFT calculations presented in Chapter 3, the energy barrier for the diffusion of these species on Cu surface is fairly low. Thus, there is a possibility that these CH_x species may combine to form larger $\text{CH}_x\text{-CH}_y$ species. Hence, these pathways should also be investigated and included in the kMC simulations. Therefore, it is recommended to study the dissociation of C_2H_4 , where dehydrogenation/hydrogenation paths ultimately leading to $\text{C}_2/\text{C}_2\text{H}_6$ are accounted for. This dissociation process would then include the dissociation of C_2H_2 and several many dehydrogenation/hydrogenation, isomerization and C-C bond scission reaction pathways. In fact, C_2H_4 and C_2H_2 themselves are used as C precursor gas in graphene and CNT growth.

- MD simulations, including the highly-accurate DFT-based AIMD and the faster force-field-based classical MD (e.g. LAMMPS), are very useful in describing the kinetics of a system. In the study of the dissociation of C-precursor gas on Cu surfaces of

Chapter 3, it is recommended to use MD simulations to complement the DFT and coarse-grained kMC simulations conducted in this dissertation. Such simulations will provide qualitative insights into the dissociation process and may verify results obtained in this study. However, it is noted that a force field specific for this dissociation on the Cu surface is currently not available.

- In Chapter 4, the products of CH_x dehydrogenation on the oxygenated Cu and Ni surfaces are CH_{x-1} and OH. While the focus of the work was the sequential dehydrogenation of CH_4 to C in the presence of surface O, it seems important to study the fate of the OH species produced from this reaction. It is likely that these OH species may form H_2O molecules and desorb to the gas phase. This likelihood can be examined by finding the energy barrier for this reaction via DFT and also verified by experimental work.

- Chapter 4 also reports the effect of surface pre-adsorbed O on the dissociation of CH_4 . This effect on the dissociation of C_2H_2 or C_2H_4 , as other common C precursor gases, is currently unknown and therefore is recommended to be studied.

- In Chapter 6, the dissociation of C_2H_2 on the Cu and Co nanoparticles was addressed by studying the dehydrogenation ($\text{C}_2\text{H}_2 \rightarrow \text{CCH} + \text{H}$) and the C-C bond scission ($\text{C}_2\text{H}_2 \rightarrow \text{CH} + \text{CH}$) reactions. However, the dissociation pathway can be continued by using the same method (DFT-NEB). The products of these reactions – CCH and CH – can be further dissociated ($\text{CCH} \rightarrow \text{CC} + \text{H}$ or $\text{CCH} \rightarrow \text{C} + \text{CH}$, $\text{CH} \rightarrow \text{C} + \text{H}$) and should therefore be studied to provide a complete picture of the dissociation process of C_2H_2 on nanoparticle catalysts. Such a study would provide valuable

information in order to draw conclusions on the dependence of dissociation mechanism on different transition metal catalysts.

- As to complement the DFT-NEB results of Chapter 6, the dissociation of C_2H_2 on the Cu and Co nanoparticles can be studied using AIMD simulations, provided that the system of support and nanoparticle catalyst is sufficient in size as to accommodate the computational demand of the calculations and be representative of a realistic system as well.

- Aside from Mo-doping and stepped MgO, another aspect of the support surface that can be studied in Chapter 6 is the effect of oxygen vacancies of the MgO support on the nanoparticle catalyst adsorption and C precursor gas dissociation process. Oxygen vacancies are possible to develop on the MgO surface at the high temperatures that the CCVD process operates in.

- The Cu and Co nanoparticles studied in Chapter 6, consisted of 9-10 atoms. Some faceting of the nanoparticles were observed and C_2H_2 adsorption and dissociation occurred mainly along the edges of the nanoparticles and closer to the interface with the support. It is recommended to test larger nanoparticles to draw more definitive conclusions in regards to faceting and adsorption/dissociation of C_2H_2 . Although, DFT-NEB calculations on larger nanoparticles would demand greater computational time and resources.

- Finally, the growth of graphene and carbon nanotubes involves many different parameters that can affect the resulting nanostructure in many different ways. Investigating different aspects of the process, gathering their corresponding data and

using big data analytics can serve as a major leap forward towards understanding the mechanism of growth, finding the most efficient method and ultimately tailoring graphene and carbon nanotubes towards specific applications.

REFERENCES

1. Zaera, F., *Mechanisms of hydrocarbon conversion reactions on heterogeneous catalysts: analogies with organometallic chemistry*. Topics in Catalysis, 2005. **34**(1): p. 129-141.
2. van Santen, R.A., *Modern Heterogeneous Catalysis: An Introduction*. 2017: Wiley.
3. Geim, A.K., *Graphene: status and prospects*. Science, 2009. **324**(5934): p. 1530-1534.
4. Jourdain, V. and C. Bichara, *Review: Current understanding of the growth of carbon nanotubes in catalytic chemical vapour deposition*. Carbon, 2013. **58**: p. 2-39.
5. Mattevi, C., H. Kim, and M. Chhowalla, *A review of chemical vapour deposition of graphene on copper*. J. Mater. Chem., 2011. **21**(10): p. 3324-3334.
6. Batzill, M., *The surface science of graphene: Metal interfaces, CVD synthesis, nanoribbons, chemical modifications, and defects*. Surface Science Reports, 2012. **67**(3-4): p. 83-115.
7. Chanier, T. and L. Henrard, *From carbon atom to graphene on Cu(111): an ab-initio study*. The European Physical Journal B, 2015. **88**(2): p. 1-5.
8. Gugliuzza, A., A. Politano, and E. Drioli, *The advent of graphene and other two-dimensional materials in membrane science and technology*. Current Opinion in Chemical Engineering, 2017. **16**: p. 78-85.
9. Politano, A. and G. Chiarello, *Plasmon modes in graphene: status and prospect*. Nanoscale, 2014. **6**(19): p. 10927-10940.
10. Cupolillo, A., et al., *Substrate-dependent plasmonic properties of supported graphene*. Surface Science, 2015. **634**: p. 76-80.
11. Novoselov, K.S., et al., *Electric field effect in atomically thin carbon films*. Science, 2004. **306**(5696): p. 666-669.
12. Pei, S. and H.-M. Cheng, *The reduction of graphene oxide*. Carbon, 2012. **50**(9): p. 3210-3228.

13. Chua, C.K. and M. Pumera, *Selective removal of hydroxyl groups from graphene oxide*. Chemistry – A European Journal, 2013. **19**(6): p. 2005-2011.
14. Eigler, S. and A. Hirsch, *Chemistry with graphene and graphene oxide—challenges for synthetic chemists*. Angewandte Chemie International Edition, 2014. **53**(30): p. 7720-7738.
15. Seah, C.-M., S.-P. Chai, and A.R. Mohamed, *Mechanisms of graphene growth by chemical vapour deposition on transition metals*. Carbon, 2014. **70**: p. 1-21.
16. Iijima, S., *Helical microtubules of graphitic carbon*. Nature, 1991. **354**: p. 56-58.
17. Thess, A., et al., *Crystalline ropes of metallic carbon nanotubes*. Science, 1996. **273**(5274): p. 483-487.
18. Hou, P.X., et al., *Multi-step purification of carbon nanotubes*. Carbon, 2002. **40**(1): p. 81-85.
19. Chico, L., et al., *Pure carbon nanoscale devices: nanotube heterojunctions*. Physical Review Letters, 1996. **76**(6): p. 971-974.
20. Ajayan, P.M. and T.W. Ebbesen, *Nanometre-size tubes of carbon*. Reports on Progress in Physics, 1997. **60**(10): p. 1025-1062.
21. Dai, H., et al., *Single-wall nanotubes produced by metal-catalyzed disproportionation of carbon monoxide*. Chemical Physics Letters, 1996. **260**(3): p. 471-475.
22. Saito, R., et al., *Electronic structure of chiral graphene tubules*. Applied Physics Letters, 1992. **60**(18): p. 2204-2206.
23. Saito, R., G. Dresselhaus, and M.S. Dresselhaus, *Trigonal warping effect of carbon nanotubes*. Physical Review B, 2000. **61**(4): p. 2981-2990.
24. Shah, K.A. and B.A. Tali, *Synthesis of carbon nanotubes by catalytic chemical vapour deposition: A review on carbon sources, catalysts and substrates*. Materials Science in Semiconductor Processing, 2016. **41**: p. 67-82.
25. Page, A.J., et al., *Insights into carbon nanotube and graphene formation mechanisms from molecular simulations: a review*. Rep Prog Phys, 2015. **78**(3): p. 1-38.

26. Rao, R., et al., *Carbon nanotubes and related nanomaterials: critical advances and challenges for synthesis toward mainstream commercial applications*. ACS Nano, 2018. **12**(12): p. 11756-11784.
27. Cheng, H.M., et al., *Large-scale and low-cost synthesis of single-walled carbon nanotubes by the catalytic pyrolysis of hydrocarbons*. Applied Physics Letters, 1998. **72**(25): p. 3282-3284.
28. Wagner, R.S. and W.C. Ellis, *Vapor-liquid-solid mechanism of single crystal growth*. Applied Physics Letters, 1964. **4**(5): p. 89-90.
29. Hofmann, S., et al., *Surface diffusion: the low activation energy path for nanotube growth*. Phys Rev Lett, 2005. **95**(3): p. 036101(1)-036101(4).
30. Chen, M., et al., *Low-temperature synthesis multiwalled carbon nanotubes by microwave plasma chemical vapor deposition using CH₄-CO₂ gas mixture*. Japanese Journal of Applied Physics, 2003. **42**(Part 1, No. 2A): p. 614-619.
31. Seidel, R., et al., *Chemical vapor deposition growth of single-walled carbon nanotubes at 600 °C and a simple growth model*. The Journal of Physical Chemistry B, 2004. **108**(6): p. 1888-1893.
32. Sen, R., A. Govindaraj, and C.N.R. Rao, *Carbon nanotubes by the metallocene route*. Chemical Physics Letters, 1997. **267**(3): p. 276-280.
33. Dupuis, A.-C., *The catalyst in the CCVD of carbon nanotubes—a review*. Progress in Materials Science, 2005. **50**(8): p. 929-961.
34. Ding, F., A. Rosen, and K. Bolton, *Molecular dynamics study of the catalyst particle size dependence on carbon nanotube growth*. J Chem Phys, 2004. **121**(6): p. 2775-2779.
35. Nasibulin, A.G., et al., *Correlation between catalyst particle and single-walled carbon nanotube diameters*. Carbon, 2005. **43**(11): p. 2251-2257.
36. Fiawoo, M.F., et al., *Evidence of correlation between catalyst particles and the single-wall carbon nanotube diameter: a first step towards chirality control*. Phys Rev Lett, 2012. **108**(19): p. 195503(1)-195503(5).
37. Baba, M., et al., *Effect of Mo in Co-Mo/MgO catalysts on the synthesis yield and structure of carbon nanotubes*. Journal of the Ceramic Society of Japan, 2009. **117**(1365): p. 654-658.

38. Harutyunyan, A.R., et al., *Reduced carbon solubility in Fe nanoclusters and implications for the growth of single-walled carbon nanotubes*. Physical Review Letters, 2008. **100**(19): p. 195502(1)-195502(4).
39. Stadermann, M., et al., *Mechanism and kinetics of growth termination in controlled chemical vapor deposition growth of multiwall carbon nanotube arrays*. Nano Letters, 2009. **9**(2): p. 738-744.
40. Kim, S.M., et al., *Evolution in catalyst morphology leads to carbon nanotube growth termination*. Journal of Physical Chemistry Letters, 2010. **1**(6): p. 918-922.
41. Kim, S.M., et al., *Catalyst and catalyst support morphology evolution in single-walled carbon nanotube supergrowth: Growth deceleration and termination*. Journal of Materials Research, 2010. **25**(10): p. 1875-1885.
42. Yoon, B., et al., *Charging effects on bonding and catalyzed oxidation of CO on Au₈ clusters on MgO*. Science, 2005. **307**(5708): p. 403-407.
43. Sanchez, A., et al., *When gold is not noble: nanoscale gold catalysts*. The Journal of Physical Chemistry A, 1999. **103**(48): p. 9573-9578.
44. Greeley, J., J.K. Nørskov, and M. Mavrikakis, *Electronic structure and catalysis on metal surfaces*. Annual Review of Physical Chemistry, 2002. **53**(1): p. 319-348.
45. Sholl, D. and J.A. Steckel, *Density Functional Theory: A Practical Introduction*. 2011: Wiley.
46. Schrödinger, E., *Quantisierung als eigenwertproblem*. Annalen der Physik, 1926. **384**(4): p. 361-376.
47. Born, M. and R. Oppenheimer, *Zur quantentheorie der molekeln*. Annalen der Physik, 1927. **389**(20): p. 457-484.
48. van Santen, R.A. and P. Sautet, *Computational Methods in Catalysis and Materials Science: An Introduction for Scientists and Engineers*. 2009: John Wiley & Sons.
49. Lee, J.G., *Computational Materials Science: An Introduction*. 2011: CRC Press.
50. Hohenberg, P. and W. Kohn, *Inhomogeneous electron gas*. Physical Review, 1964. **136**(3B): p. B864-B871.

51. Kohn, W. and L.J. Sham, *Self-consistent equations including exchange and correlation effects*. Physical Review, 1965. **140**(4A): p. A1133-A1138.
52. Groß, A., *Theoretical Surface Science: A Microscopic Perspective*. 2013: Springer Berlin Heidelberg.
53. Ceperley, D.M. and B.J. Alder, *Ground state of the electron gas by a stochastic method*. Physical Review Letters, 1980. **45**(7): p. 566-569.
54. Becke, A.D., *Density-functional exchange-energy approximation with correct asymptotic behavior*. Physical Review A, 1988. **38**(6): p. 3098-3100.
55. Perdew, J.P., et al., *Atoms, molecules, solids, and surfaces: Applications of the generalized gradient approximation for exchange and correlation*. Physical Review B, 1992. **46**(11): p. 6671-6687.
56. Perdew, J.P., K. Burke, and M. Ernzerhof, *Generalized Gradient Approximation Made Simple*. Phys. Rev. Lett., 1996. **77**: p. 3865-3868.
57. Blöchl, P.E., *Projector augmented-wave method*. Phys. Rev. B: Condens. Matter Mater. Phys., 1994. **50**: p. 17953-17979.
58. Kresse, G. and D. Joubert, *From ultrasoft pseudopotentials to the projector augmented-wave method*. Physical Review B, 1999. **59**(3): p. 1758-1775.
59. Hellmann, H., *Einführung in die Quantenchemie*. 1937: Franz Deuticke.
60. Feynman, R.P., *Forces in molecules*. Physical Review, 1939. **56**(4): p. 340-343.
61. Kohn, W., A.D. Becke, and R.G. Parr, *Density functional theory of electronic structure*. The Journal of Physical Chemistry, 1996. **100**(31): p. 12974-12980.
62. Grimme, S., *Semiempirical GGA-type density functional constructed with a long-range dispersion correction*. J. Comput. Chem., 2006. **27**: p. 1787-1799.
63. Grimme, S., et al., *A consistent and accurate ab initio parametrization of density functional dispersion correction (DFT-D) for the 94 elements H-Pu*. The Journal of Chemical Physics, 2010. **132**(15): p. 154104(1)-154104(19).
64. Hubbard, J. and B.H. Flowers, *Electron correlations in narrow energy bands*. Proceedings of the Royal Society of London. Series A. Mathematical and Physical Sciences, 1963. **276**(1365): p. 238-257.
65. Anisimov, V.I., J. Zaanen, and O.K. Andersen, *Band theory and Mott insulators: Hubbard U instead of Stoner I*. Physical Review B, 1991. **44**(3): p. 943-954.

66. Dudarev, S.L., et al., *Electron-energy-loss spectra and the structural stability of nickel oxide: An LSDA+U study*. Physical Review B, 1998. **57**(3): p. 1505-1509.
67. Henkelman, G. and H. Jónsson, *Improved tangent estimate in the nudged elastic band method for finding minimum energy paths and saddle points*. The Journal of Chemical Physics, 2000. **113**(22): p. 9978-9985.
68. Henkelman, G., B.P. Uberuaga, and H. Jónsson, *A climbing image nudged elastic band method for finding saddle points and minimum energy paths*. The Journal of Chemical Physics, 2000. **113**(22): p. 9901-9904.
69. Car, R. and M. Parrinello, *Unified approach for molecular dynamics and density-functional theory*. Physical Review Letters, 1985. **55**(22): p. 2471-2474.
70. Hoover, W.G., *Temperature, least action, and Lagrangian mechanics*. Physics Letters A, 1995. **204**(2): p. 133-135.
71. Eyring, H., *The activated complex in chemical reactions*. The Journal of Chemical Physics, 1935. **3**(2): p. 107-115.
72. Vineyard, G.H., *Frequency factors and isotope effects in solid state rate processes*. Journal of Physics and Chemistry of Solids, 1957. **3**(1): p. 121-127.
73. Hänggi, P., P. Talkner, and M. Borkovec, *Reaction-rate theory: fifty years after Kramers*. Reviews of Modern Physics, 1990. **62**(2): p. 251-341.
74. Bligaard, T. and J.K. Nørskov, *Chapter 4 - Heterogeneous Catalysis*, in *Chemical Bonding at Surfaces and Interfaces*, A. Nilsson, L.G.M. Pettersson, and J.K. Nørskov, Editors. 2008, Elsevier: Amsterdam. p. 255-321.
75. Stamatakis, M., *Kinetic modelling of heterogeneous catalytic systems*. Journal of Physics: Condensed Matter, 2015. **27**(1): p. 013001-013018.
76. Bortz, A.B., M.H. Kalos, and J.L. Lebowitz, *A new algorithm for Monte Carlo simulation of Ising spin systems*. Journal of Computational Physics, 1975. **17**(1): p. 10-18.
77. Stamatakis, M. and D.G. Vlachos, *A graph-theoretical kinetic Monte Carlo framework for on-lattice chemical kinetics*. The Journal of Chemical Physics, 2011. **134**(21): p. 214115(1)-214115(13).
78. Stamatakis, M., *Zacros: Advanced Lattice-KMC simulation Made Easy*, http://www.e-lucid.com/i/software/material_modelling/Zacros.html.

79. Li, X., et al., *Large-area synthesis of high-quality and uniform graphene films on copper foils*. *Science*, 2009. **324**(5932): p. 1312-1314.
80. Kim, H., et al., *Activation energy paths for graphene nucleation and growth on Cu*. *ACS Nano*, 2012. **6**(4): p. 3614-3623.
81. Celebi, K., et al., *Evolutionary kinetics of graphene formation on copper*. *Nano Letters*, 2013. **13**(3): p. 967-974.
82. Shibuta, Y. and S. Maruyama, *Molecular dynamics simulation of formation process of single-walled carbon nanotubes by CCVD method*. *Chemical Physics Letters*, 2003. **382**(3): p. 381-386.
83. Zhao, Z.-J., C.-c. Chiu, and J. Gong, *Molecular understandings on the activation of light hydrocarbons over heterogeneous catalysts*. *Chemical Science*, 2015. **6**(8): p. 4403-4425.
84. Wang, X., et al., *The transition metal surface dependent methane decomposition in graphene chemical vapor deposition growth*. *Nanoscale*, 2017. **9**(32): p. 11584-11589.
85. Gajewski, G. and C.-W. Pao, *Ab initio calculations of the reaction pathways for methane decomposition over the Cu (111) surface*. *The Journal of Chemical Physics*, 2011. **135**(6): p. 064707.
86. Ciobîcă, I.M., et al., *A DFT study of transition states for C–H activation on the Ru(0001) surface*. *The Journal of Physical Chemistry B*, 2000. **104**(14): p. 3364-3369.
87. An, W., X.C. Zeng, and C.H. Turner, *First-principles study of methane dehydrogenation on a bimetallic Cu/Ni(111) surface*. *The Journal of Chemical Physics*, 2009. **131**(17): p. 174702(1)-174702(11).
88. Kokalj, A., et al., *Methane dehydrogenation on Rh@Cu(111): a first-principles study of a model catalyst*. *Journal of the American Chemical Society*, 2006. **128**(38): p. 12448-12454.
89. Arevalo, R.L., et al., *Tuning methane decomposition on stepped Ni surface: The role of subsurface atoms in catalyst design*. *Scientific Reports*, 2017. **7**(1): p. 13963(1)-13963(8).
90. Bengaard, H.S., et al., *Steam reforming and graphite formation on Ni catalysts*. *Journal of Catalysis*, 2002. **209**(2): p. 365-384.

91. Helveg, S., et al., *Atomic-scale imaging of carbon nanofibre growth*. Nature, 2004. **427**: p. 426-429.
92. Lee, Y., et al., *Wafer-scale synthesis and transfer of graphene films*. Nano Letters, 2010. **10**(2): p. 490-493.
93. Rasool, H., et al., *Atomic-scale characterization of graphene grown on copper (100) single crystals*. Journal of the American Chemical Society, 2011. **133**(32): p. 12536-12543.
94. Rasool, H.I., et al., *Continuity of graphene on polycrystalline copper*. Nano Letters, 2011. **11**(1): p. 251-256.
95. Reddy, K.M., et al., *High quality, transferrable graphene grown on single crystal Cu(111) thin films on basal-plane sapphire*. Applied Physics Letters, 2011. **98**(11): p. 113117(1)-113117(3).
96. Celebi, K., et al., *Observations of early stage graphene growth on copper*. Electrochemical and Solid-State Letters, 2011. **15**(1): p. K1-K4.
97. Gao, L., J. Guest, and N. Guisinger, *Epitaxial graphene on Cu(111)*. Nano letters, 2010. **10**(9): p. 3512-3516.
98. Vlassiouk, I., et al., *Role of hydrogen in chemical vapor deposition growth of large single-crystal graphene*. ACS Nano, 2011. **5**(7): p. 6069-6076.
99. Zhang, Y., et al., *Anisotropic hydrogen etching of chemical vapor deposited graphene*. ACS Nano, 2012. **6**(1): p. 126-132.
100. Choubak, S., et al., *No graphene etching in purified hydrogen*. The Journal of Physical Chemistry Letters, 2013. **4**(7): p. 1100-1103.
101. Qi, M., et al., *Hydrogen kinetics on scalable graphene growth by atmospheric pressure chemical vapor deposition with acetylene*. The Journal of Physical Chemistry C, 2013. **117**(27): p. 14348-14353.
102. Zhang, X., et al., *Role of hydrogen in graphene chemical vapor deposition growth on a copper surface*. Journal of the American Chemical Society, 2014. **136**(8): p. 3040-3047.
103. Losurdo, M., et al., *Graphene CVD growth on copper and nickel: role of hydrogen in kinetics and structure*. Physical Chemistry Chemical Physics, 2011. **13**(46): p. 20836-20843.

104. Goyal, A., et al., *Synthesis of carbide-free, high strength iron–carbon nanotube composite by in situ nanotube growth*. Chemical Physics Letters, 2007. **442**(4): p. 365-371.
105. Ohashi, F., et al., *The role of the gas species on the formation of carbon nanotubes during thermal chemical vapour deposition*. Nanotechnology, 2008. **19**(44): p. 445605(1)-445605(6).
106. Behr, M.J., et al., *Effect of hydrogen on catalyst nanoparticles in carbon nanotube growth*. Journal of Applied Physics, 2010. **108**(5): p. 053303(1)-053303(8).
107. Zhang, W., et al., *First-principles thermodynamics of graphene growth on Cu surfaces*. The Journal of Physical Chemistry C, 2011. **115**(36): p. 17782-17787.
108. Shibuta, Y., et al., *Low reactivity of methane on copper surface during graphene synthesis via CVD process: Ab initio molecular dynamics simulation*. Chemical Physics Letters, 2014. **610-611**: p. 33-38.
109. Kresse, G. and J. Furthmuller, *Efficient iterative schemes for ab initio total-energy calculations using a plane-wave basis set*. Physical Review B, 1996. **54**(16): p. 11169-11186.
110. Kresse, G. and J. Furthmuller, *Efficiency of ab-initio total energy calculations for metals and semiconductors using a plane-wave basis set*. Computational Materials Science, 1996. **6**(1): p. 15-50.
111. Perdew, J.P., K. Burke, and M. Ernzerhof, *Generalized gradient approximation made simple*. Physical Review Letters, 1996. **77**(18): p. 3865-3868.
112. Shu, H., X.-M. Tao, and F. Ding, *What are the active carbon species during graphene chemical vapor deposition growth?* Nanoscale, 2015. **7**(5): p. 1627-1634.
113. Galea, N.M., D. Knapp, and T. Ziegler, *Density functional theory studies of methane dissociation on anode catalysts in solid-oxide fuel cells: Suggestions for coke reduction*. Journal of Catalysis, 2007. **247**(1): p. 20-33.
114. Wu, P., et al., *Communication: Coalescence of carbon atoms on Cu (111) surface: Emergence of a stable bridging-metal structure motif*. The Journal of Chemical Physics, 2010. **133**(7): p. 071101(1)-071101(4).

115. Chen, H., W. Zhu, and Z. Zhang, *Contrasting behavior of carbon nucleation in the initial stages of graphene epitaxial growth on stepped metal surfaces*. Physical Review Letters, 2010. **104**(18): p. 186101(1)-186101(4).
116. Rao, R., K. Weaver, and B. Maruyama, *Atmospheric pressure growth and optimization of graphene using liquid-injection chemical vapor deposition*. Materials Express, 2015. **5**(6): p. 6.
117. Ogawa, Y., *Domain structure and boundary in single-layer graphene grown on Cu(111) and Cu(100) films*. The journal of physical chemistry letters, 2012. **3**(2): p. 219-226.
118. Yuan, Q., et al., *Formation of graphene grain boundaries on Cu(100) surface and a route towards their elimination in chemical vapor deposition growth*. Sci Rep, 2014. **4**: p. 6541(1)-6541(5).
119. Li, X., et al., *Graphene films with large domain size by a two-step chemical vapor deposition process*. Nano Letters, 2010. **10**(11): p. 4328-4334.
120. Tao, L., et al., *Synthesis of high quality monolayer graphene at reduced temperature on hydrogen-enriched evaporated copper (111) films*. ACS Nano, 2012. **6**(3): p. 2319-2325.
121. Braeuninger Weimer, P., *Understanding and controlling Cu-catalyzed graphene nucleation: the role of impurities, roughness, and oxygen scavenging*. Chemistry of materials, 2016. **28**(24): p. 8905-8915.
122. Magnuson, C.W., et al., *Copper oxide as a "self-cleaning" substrate for graphene growth*. Journal of Materials Research, 2014. **29**(3): p. 403-409.
123. Hao, Y., et al., *The role of surface oxygen in the growth of large single-crystal graphene on copper*. Science, 2013. **342**(6159): p. 720-723.
124. Gottardi, S., et al., *Comparing graphene growth on Cu(111) versus oxidized Cu(111)*. Nano Letters, 2015. **15**(2): p. 917-922.
125. Ma, L., J. Zhang, and K. Xu, *Structural and electronic properties of atomic oxygen adsorption on Cu(111) surface: A first-principles investigation*. Science China Physics, Mechanics and Astronomy, 2013. **56**(3): p. 573-580.
126. Lian, X., et al., *Calculations of oxide formation on low-index Cu surfaces*. The Journal of Chemical Physics, 2016. **145**(4): p. 044711(1)-044711(11).
127. Wood, J.D., *Effects of polycrystalline Cu substrate on graphene growth by chemical vapor deposition*. Nano letters, 2011. **11**(11): p. 4547-4554.

128. Zhao, L., et al., *Influence of copper crystal surface on the CVD growth of large area monolayer graphene*. Solid State Communications, 2011. **151**(7): p. 509-513.
129. Alstrup, I., I. Chorkendorff, and S. Ullmann, *The interaction of CH₄ at high temperatures with clean and oxygen precovered Cu(100)*. Surface Science, 1992. **264**(1): p. 95-102.
130. Xing, B., X.-Y. Pang, and G.-C. Wang, *C–H bond activation of methane on clean and oxygen pre-covered metals: A systematic theoretical study*. Journal of Catalysis, 2011. **282**(1): p. 74-82.
131. Yoo, J.S., et al., *On the role of the surface oxygen species during A–H (A = C, N, O) bond activation: a density functional theory study*. Chemical Communications, 2015. **51**(13): p. 2621-2624.
132. Hibbitts, D. and M. Neurock, *Promotional effects of chemisorbed oxygen and hydroxide in the activation of C–H and O–H bonds over transition metal surfaces*. Surface Science, 2016. **650**: p. 210-220.
133. Niu, T., et al., *Oxygen-promoted methane activation on copper*. The Journal of Physical Chemistry B, 2018. **122**(2): p. 855-863.
134. Vasenkov, A.V., D. Sengupta, and M. Frenklach, *Multiscale modeling catalytic decomposition of hydrocarbons during carbon nanotube growth*. The Journal of Physical Chemistry B, 2009. **113**(7): p. 1877-1882.
135. *Accelrys Software Inc. Materials Studio*. 2011: San Diego.
136. Henkelman, G., A. Arnaldsson, and H. Jonsson, *A fast and robust algorithm for Bader decomposition of charge density*. Computational Materials Science, 2006. **36**(3): p. 354-360.
137. Tang, W., E. Sanville, and G. Henkelman, *A grid-based Bader analysis algorithm without lattice bias*. Journal of Physics-Condensed Matter, 2009. **21**(8): p. 084204(1)-084204(7).
138. Gattinoni, C. and A. Michaelides, *Atomistic details of oxide surfaces and surface oxidation: the example of copper and its oxides*. Surface Science Reports, 2015. **70**(3): p. 424-447.
139. Besenbacher, F. and J.K. Nørskov, *Oxygen chemisorption on metal surfaces: General trends for Cu, Ni and Ag*. Progress in Surface Science, 1993. **44**(1): p. 5-66.

140. Wang, Z.X. and F.H. Tian, *The adsorption of O atom on Cu (100), (110), and (111) low-index and step defect surfaces*. The Journal of Physical Chemistry B, 2003. **107**(25): p. 6153-6161.
141. Pang, X.-Y., L.-Q. Xue, and G.-C. Wang, *Adsorption of atoms on Cu surfaces: a density functional theory study*. Langmuir, 2007. **23**(9): p. 4910-4917.
142. Riikonen, S., et al., *The role of stable and mobile carbon adspecies in copper-promoted graphene growth*. The Journal of Physical Chemistry C, 2012. **116**(9): p. 5802-5809.
143. Resasco, D.E., et al., *A scalable process for production of single-walled carbon nanotubes (SWNTs) by catalytic disproportionation of CO on a solid catalyst*. Journal of Nanoparticle Research, 2002. **4**(1-2): p. 131-136.
144. Picher, M., et al., *Nucleation of graphene and its conversion to single-walled carbon nanotubes*. Nano Lett, 2014. **14**(11): p. 6104-6108.
145. Nikolaev, P., et al., *Gas-phase catalytic growth of single-walled carbon nanotubes from carbon monoxide*. Chemical Physics Letters, 1999. **313**(1): p. 91-97.
146. Bronikowski, M.J., et al., *Gas-phase production of carbon single-walled nanotubes from carbon monoxide via the HiPco process: A parametric study*. Journal of Vacuum Science & Technology A: Vacuum, Surfaces, and Films, 2001. **19**(4): p. 1800-1805.
147. Valden, M., et al., *Dissociative chemisorption of methane on clean and oxygen precovered Pt(111)*. Applied Surface Science, 1996. **99**(2): p. 83-89.
148. Au, C.-T., C.-F. Ng, and M.-S. Liao, *Methane dissociation and syngas formation on Ru, Os, Rh, Ir, Pd, Pt, Cu, Ag, and Au: a theoretical study*. Journal of Catalysis, 1999. **185**(1): p. 12-22.
149. Hammer, B. and J.K. Nørskov, *Electronic factors determining the reactivity of metal surfaces*. Surface Science, 1995. **343**(3): p. 211-220.
150. Morozov, V.A., M.V. Petrova, and N.N. Lukzen, *Exchange coupling transformations in Cu (II) heterospin complexes of "breathing crystals" under structural phase transitions*. AIP Advances, 2015. **5**(8): p. 087161(1)-087161(13).

151. Mann, G.W., et al., *First-principles Hubbard U approach for small molecule binding in metal-organic frameworks*. The Journal of Chemical Physics, 2016. **144**(17): p. 174104(1)-174104(8).
152. Dathbun, A. and S. Chaisitsak. *Effects of three parameters on graphene synthesis by chemical vapor deposition*. in *The 8th Annual IEEE International Conference on Nano/Micro Engineered and Molecular Systems*. 2013.
153. Politano, A., et al., *Multiple acoustic surface plasmons in graphene/Cu(111) contacts*. Physical Review B, 2018. **97**(3): p. 035414(1)-035414(7).
154. Politano, A., et al., *Dispersion and damping of the interband π plasmon in graphene grown on Cu(111) foils*. Carbon, 2017. **114**: p. 70-76.
155. McLellan, R.B., *The solubility of carbon in solid gold, copper, and silver*. Scripta Metallurgica, 1969. **3**(6): p. 389-391.
156. Lopez, G.A. and E. Mittemeijer, *The solubility of C in solid Cu*. Scripta Materialia, 2004. **51**(1): p. 1-5.
157. Yazyev, O.V. and A. Pasquarello, *Effect of metal elements in catalytic growth of carbon nanotubes*. Physical Review Letters, 2008. **100**(15): p. 156102(1)-156102(4).
158. Li, Y., et al., *How catalysts affect the growth of single-walled carbon nanotubes on substrates*. Adv Mater, 2010. **22**(13): p. 1508-1515.
159. Yazyev, O.V. and A. Pasquarello, *Carbon diffusion in CVD growth of carbon nanotubes on metal nanoparticles*. physica status solidi (b), 2008. **245**(10): p. 2185-2188.
160. Li, J., E. Croiset, and L. Ricardez-Sandoval, *Effects of metal elements in catalytic growth of carbon nanotubes/graphene: A first principles DFT study*. Applied Surface Science, 2014. **317**: p. 923-928.
161. Li, H.-B., et al., *Graphene nucleation on a surface-molten copper catalyst: quantum chemical molecular dynamics simulations*. Chemical Science, 2014. **5**(9): p. 3493-3500.
162. Wassei, J.K., et al., *Chemical vapor deposition of graphene on copper from methane, ethane and propane: evidence for bilayer selectivity*. Small, 2012. **8**(9): p. 1415-1422.

163. Faggio, G., et al., *High-temperature growth of graphene films on copper foils by ethanol chemical vapor deposition*. The Journal of Physical Chemistry C, 2013. **117**(41): p. 21569-21576.
164. Michon, A., et al., *Effects of pressure, temperature, and hydrogen during graphene growth on SiC(0001) using propane-hydrogen chemical vapor deposition*. Journal of Applied Physics, 2013. **113**(20): p. 203501(1)-203501(8).
165. Robinson, Z.R., et al., *Influence of chemisorbed oxygen on the growth of graphene on Cu(100) by chemical vapor deposition*. The Journal of Physical Chemistry C, 2013. **117**(45): p. 23919-23927.
166. Yu, H.K., et al., *Chemical vapor deposition of graphene on a "peeled-off" epitaxial Cu(111) foil: a simple approach to improved properties*. ACS Nano, 2014. **8**(8): p. 8636-8643.
167. N'Diaye, A.T., et al., *Structure of epitaxial graphene on Ir(111)*. New Journal of Physics, 2008. **10**(4): p. 043033(1)-043033(16).
168. Huang, P.Y., et al., *Grains and grain boundaries in single-layer graphene atomic patchwork quilts*. Nature, 2011. **469**: p. 389-393.
169. Kim, K., et al., *Grain boundary mapping in polycrystalline graphene*. ACS Nano, 2011. **5**(3): p. 2142-2146.
170. Hwang, C., et al., *Initial stage of graphene growth on a Cu substrate*. The Journal of Physical Chemistry C, 2011. **115**(45): p. 22369-22374.
171. Rogge, P.C., et al., *Real-time observation of epitaxial graphene domain reorientation*. Nature Communications, 2015. **6**: p. 6880(1)-6880(6).
172. Taioli, S., *Computational study of graphene growth on copper by first-principles and kinetic Monte Carlo calculations*. J Mol Model, 2014. **20**(7): p. 2260(1)-2260(13).
173. Vlassiouk, I., et al., *Graphene nucleation density on copper: fundamental role of background pressure*. The Journal of Physical Chemistry C, 2013. **117**(37): p. 18919-18926.
174. Horcas, I., et al., *WSXM: A software for scanning probe microscopy and a tool for nanotechnology*. Review of Scientific Instruments, 2007. **78**(1): p. 013705(1)-013705(8).
175. Sutter, P.W., J.-I. Flege, and E.A. Sutter, *Epitaxial graphene on ruthenium*. Nature Materials, 2008. **7**: p. 406-411.

176. Coraux, J., et al., *Growth of graphene on Ir(1 1 1)*. New J. Phys., 2009. **11**(2): p. 023006(1)-023006(22).
177. N'Diaye, A.T., et al., *A versatile fabrication method for cluster superlattices*. New Journal of Physics, 2009. **11**(10): p. 103045(1)-103045(19).
178. Zhiping, X. and J.B. Markus, *Interface structure and mechanics between graphene and metal substrates: a first-principles study*. Journal of Physics: Condensed Matter, 2010. **22**(48): p. 485301(1)-485301(5).
179. Joseph, M.W., et al., *Extraordinary epitaxial alignment of graphene islands on Au(111)*. New Journal of Physics, 2012. **14**(5): p. 053008(1)-053008(10).
180. Nie, S., et al., *Scanning tunneling microscopy study of graphene on Au(111): Growth mechanisms and substrate interactions*. Physical Review B, 2012. **85**(20): p. 205406(1)-205406(6).
181. Wu, P., et al., *Carbon dimers as the dominant feeding species in epitaxial growth and morphological phase transition of graphene on different Cu substrates*. Physical Review Letters, 2015. **114**(21): p. 216102(1)-216102(5).
182. Li, Y., et al., *An important atomic process in the CVD growth of graphene: Sinking and up-floating of carbon atom on copper surface*. Applied Surface Science, 2013. **284**: p. 207-213.
183. Page, A.J., et al., *Nucleation of graphene precursors on transition metal surfaces: insights from theoretical simulations*. The Journal of Physical Chemistry C, 2013. **117**(28): p. 14858-14864.
184. Jiao, M., et al., *QM/MD studies on graphene growth from small islands on the Ni(111) surface*. Nanoscale, 2016. **8**(5): p. 3067-3074.
185. Ding, F., *The importance of strong carbon-metal adhesion for catalytic nucleation of single-walled carbon nanotubes*. Nano letters, 2008. **8**(2): p. 463-468.
186. Gomez-Gualdron, D.A., J.M. Beetge, and P.B. Balbuena, *Characterization of metal nanocatalyst state and morphology during simulated single-walled carbon nanotube growth*. Journal of Physical Chemistry C, 2013. **117**(23): p. 12061-12070.
187. Gomez-Gualdron, D.A. and P.B. Balbuena, *Characterization of carbon atomistic pathways during single-walled carbon nanotube growth on supported metal nanoparticles*. Carbon, 2013. **57**: p. 298-309.

188. Li, X.S., *Evolution of graphene growth on Ni and Cu by carbon isotope labeling*. Nano letters, 2009. **9**(12): p. 4268-4272.
189. Tetlow, H., et al., *Ethylene decomposition on Ir(111): initial path to graphene formation*. Physical Chemistry Chemical Physics, 2016. **18**(40): p. 27897-27909.
190. Lee, G.-D., et al., *Catalytic decomposition of acetylene on Fe(001): A first-principles study*. Physical Review B, 2002. **66**(8): p. 081403(1)-081403(4).
191. Lo, J.M.H. and T. Ziegler, *Theoretical studies of the formation and reactivity of C₂ hydrocarbon species on the Fe(100) surface*. The Journal of Physical Chemistry C, 2007. **111**(35): p. 13149-13162.
192. Kitiyanan, B., et al., *Controlled production of single-wall carbon nanotubes by catalytic decomposition of CO on bimetallic Co–Mo catalysts*. Chemical Physics Letters, 2000. **317**: p. 497-503.
193. Shajahan, M., et al., *High growth of SWNTs and MWNTs from C₂H₂ decomposition over Co-Mo/MgO catalysts*. Carbon, 2004. **42**(11): p. 2245-2253.
194. Bachilo, S.M., et al., *Narrow (n,m)-distribution of single-walled carbon nanotubes grown using a solid supported catalyst*. Journal Of The American Chemical Society, 2003. **125**(37): p. 11186-11187.
195. Picher, M., et al., *Processes controlling the diameter distribution of single-walled carbon nanotubes during catalytic chemical vapor deposition*. ACS Nano, 2011. **5**(3): p. 2118-2125.
196. Singh, B.K., et al., *Growth of multiwalled carbon nanotubes from acetylene over in situ formed Co nanoparticles on MgO support*. Solid State Communications, 2006. **139**(3): p. 102-107.
197. Ni, L., et al., *Kinetic study of carbon nanotube synthesis over Mo/Co/MgO catalysts*. Carbon, 2006. **44**(11): p. 2265-2272.
198. Tang, S., et al., *Controlled growth of single-walled carbon nanotubes by catalytic decomposition of CH₄ over Mo/Co/MgO catalysts*. Chemical Physics Letters, 2001. **350**(1): p. 19-26.
199. Ago, H., et al., *Gas analysis of the CVD process for high yield growth of carbon nanotubes over metal-supported catalysts*. Carbon, 2006. **44**(14): p. 2912-2918.

200. Zhou, L.-P., et al., *Catalytic functions of Mo/Ni/MgO in the synthesis of thin carbon nanotubes*. The Journal of Physical Chemistry B, 2005. **109**(10): p. 4439-4447.
201. Scanlon, D.O., et al., *Surface sensitivity in lithium-doping of MgO: a density functional theory study with correction for on-site coulomb interactions*. The Journal of Physical Chemistry C, 2007. **111**(22): p. 7971-7979.
202. Shao, X., et al., *Tailoring the shape of metal ad-particles by doping the oxide support*. Angew. Chem., Int. Ed., 2011. **50**: p. 11525-11527.
203. Nikbin, N., et al., *Catalysis at the sub-nanoscale: complex CO oxidation chemistry on a few Au atoms*. Catalysis Science & Technology, 2015. **5**(1): p. 134-141.
204. Prada, S., *Charging of gold atoms on doped MgO and CaO: Identifying the key parameters by DFT calculations*. The journal of physical chemistry. C, 2013. **117**(19): p. 9943-9951.
205. Page, A.J., et al., *Comparison of single-walled carbon nanotube growth from Fe and Ni nanoparticles using quantum chemical molecular dynamics methods*. Carbon, 2010. **48**(11): p. 3014-3026.
206. Page, A.J., *Mechanisms of single-walled carbon nanotube nucleation, growth, and healing determined using QM/MD methods*. Accounts of chemical research, 2010. **43**(10): p. 1375-1385.
207. Silveary, F., et al., *Establishing the most favorable metal-carbon bond strength for carbon nanotube catalysts*. J. Mater. Chem. C, 2015. **3**(14): p. 3422-3427.
208. Cadigan, C.A., et al., *Nanoscale (111) faceted rock-salt metal oxides in catalysis*. Catal. Sci. Technol., 2013. **3**(4): p. 900-911.
209. Corpuz, A. and R. Richards, *Chemistry of rocksalt-structured (111) metal oxides*, in *Nanoscale Materials in Chemistry : Environmental Applications*, L.E. Erickson, R.T. Koodali, and R.M. Richards, Editors. 2010, Amer Chemical Soc: Washington. p. 51-76.
210. Lazarov, V.K., et al., *Structure of the hydrogen-stabilized MgO(111)-(1×1) polar surface: Integrated experimental and theoretical studies*. Physical Review B, 2005. **71**(11): p. 115434(1)-115434(9).
211. Pacchioni, G. and H. Freund, *Electron transfer at oxide surfaces. The MgO paradigm: from defects to ultrathin films*. Chemical Reviews, 2013. **113**(6): p. 4035-4072.

212. Stavale, F., et al., *Donor characteristics of transition-metal-doped oxides: Cr-doped MgO versus Mo-doped CaO*. Journal of the American Chemical Society, 2012. **134**(28): p. 11380-11383.
213. Andersin, J., et al., *The redox chemistry of gold with high-valence doped calcium oxide*. Angewandte Chemie International Edition, 2013. **52**(5): p. 1424-1427.
214. Metiu, H., et al., *Chemistry of Lewis acid–base pairs on oxide surfaces*. The Journal of Physical Chemistry C, 2012. **116**(19): p. 10439-10450.
215. Musolino, V. and A. Selloni, *First principles study of adsorbed Cu[sub n] (n=1-4) microclusters on MgO(100): Structural and*. Journal of Chemical Physics, 1998. **108**(12): p. 5044-5054.
216. Gomez-Ballesteros, J.L. and P.B. Balbuena, *Structure and dynamics of metallic and carburized catalytic Ni nanoparticles: effects on growth of single-walled carbon nanotubes*. Phys Chem Chem Phys, 2015. **17**(22): p. 15056-15064.
217. Diarra, M., et al., *Carbon solubility in nickel nanoparticles: A grand canonical Monte Carlo study*. physica status solidi (b), 2012. **249**(12): p. 2629-2634.
218. Pacchioni, G. and N. Rösch, *Supported nickel and copper clusters on MgO(100): A first-principles calculation on the metal/oxide interface*. Journal of Chemical Physics, 1996. **104**(18): p. 7329-7337.
219. Mason, S.E., *Spontaneous formation of dipolar metal nanoclusters*. The journal of physical chemistry. A, 2009. **113**(16): p. 4134-4137.
220. Martinez de la Hoz, J.M. and P.B. Balbuena, *Geometric and electronic confinement effects on catalysis*. Journal of Physical Chemistry C, 2011. **115**(43): p. 21324-21333.

APPENDIX A

HYDROCARBON DISSOCIATION ON COPPER SURFACES: REACTIONS

MECHANISMS

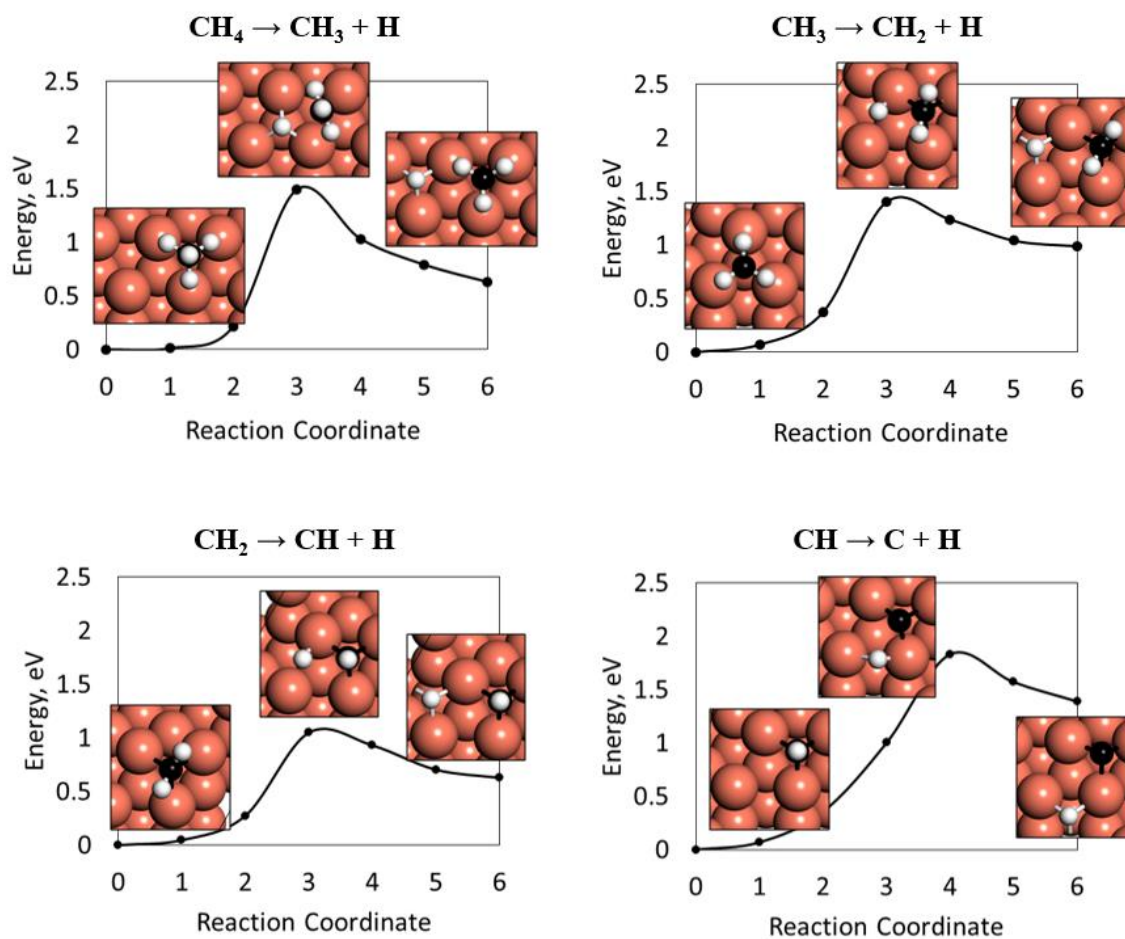


Figure A1 Successive CH_4 dehydrogenation reaction energy profiles along with initial, transition and final state images. Cu, C and H atoms are shown in orange, black and white.

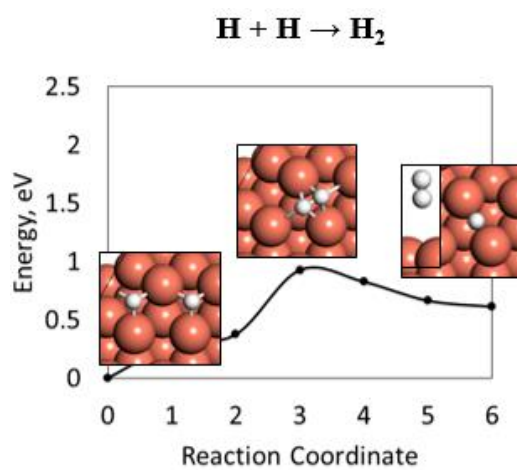


Figure A2 H₂ dissociative adsorption reaction energy profile along with the initial, transition and final state images. Cu and H atoms are shown in orange and white.

APPENDIX B

OXYGEN ADSORPTION ON LOW-INDEX COPPER SURFACES

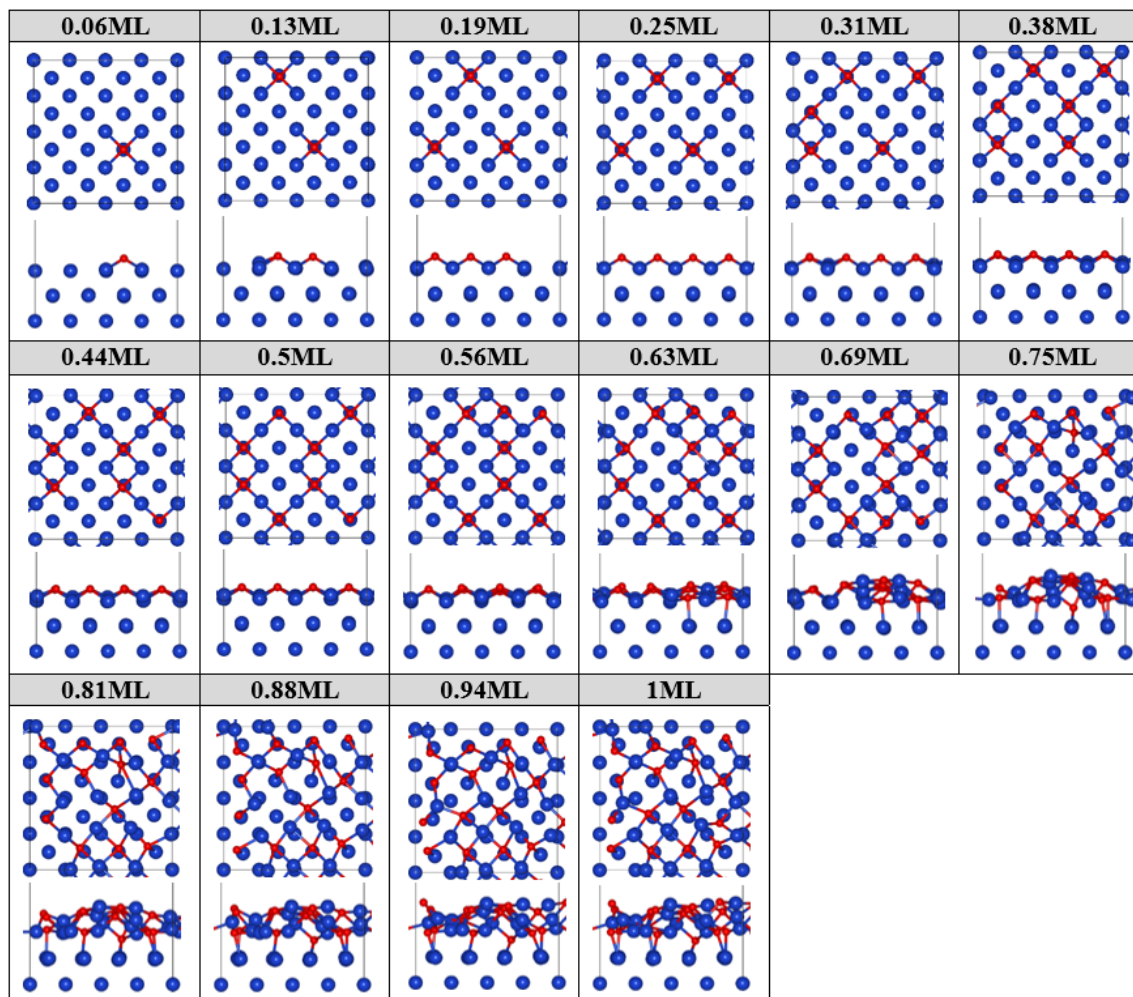


Figure B1 Top (top panels) and side (bottom panels) views of sequential O adsorption on Cu (100).

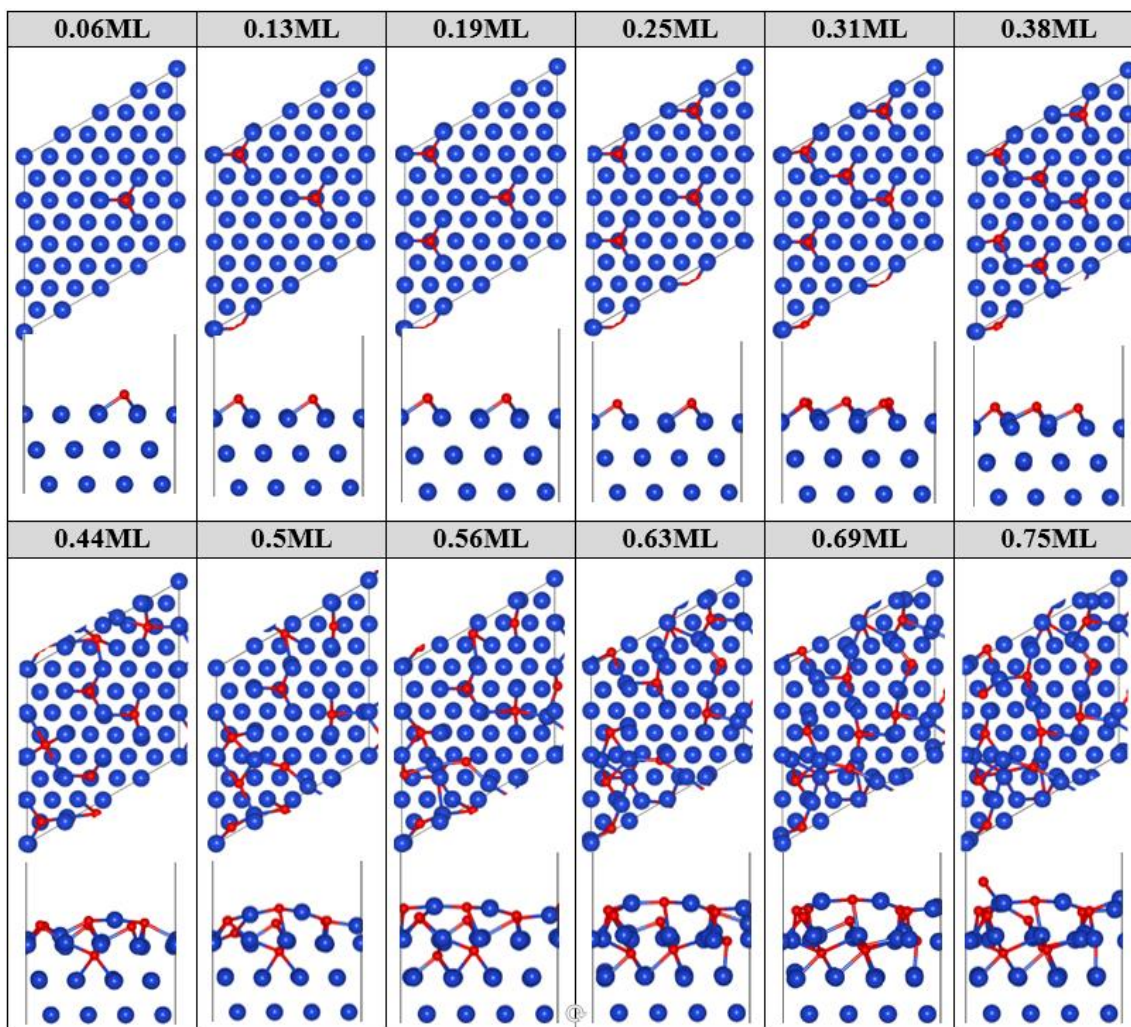


Figure B2 Top (top panels) and side (bottom panels) views of sequential O adsorption on Cu (111).

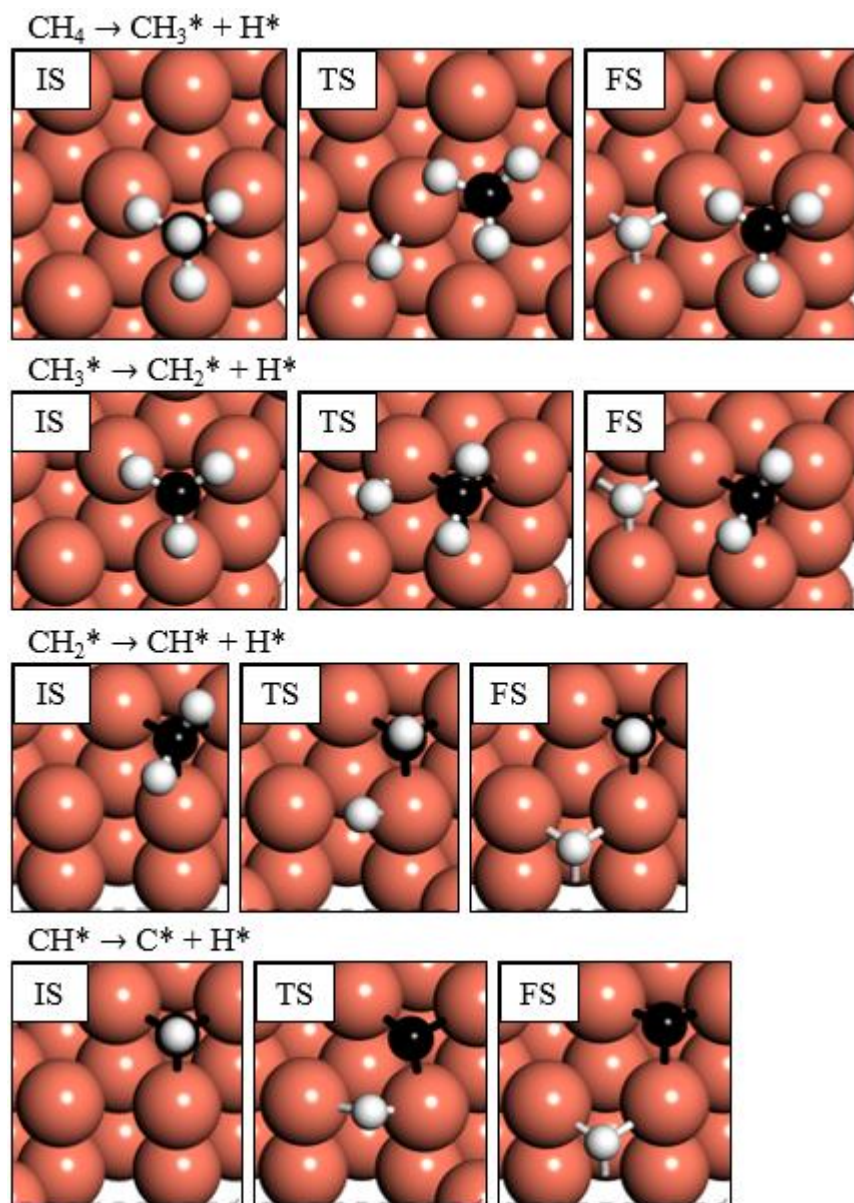


Figure B3 Initial, transition and final states of the sequential CH₄ dissociation steps on clean Cu (111). Cu, C and H atoms are shown in orange, black and white.

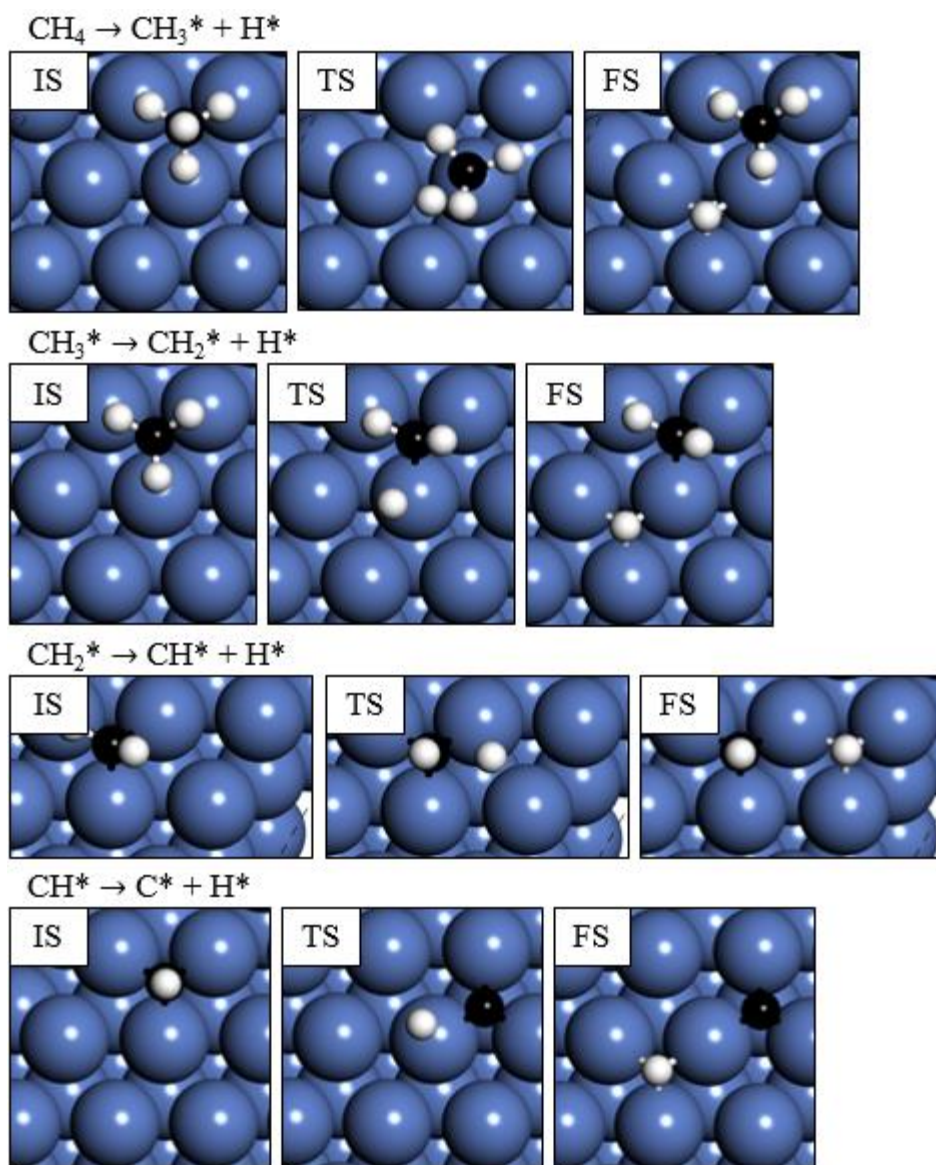


Figure B4 Initial, transition and final states of the sequential CH_4 dissociation steps on clean Ni (111). Ni, C and H atoms are shown in blue, black and white.

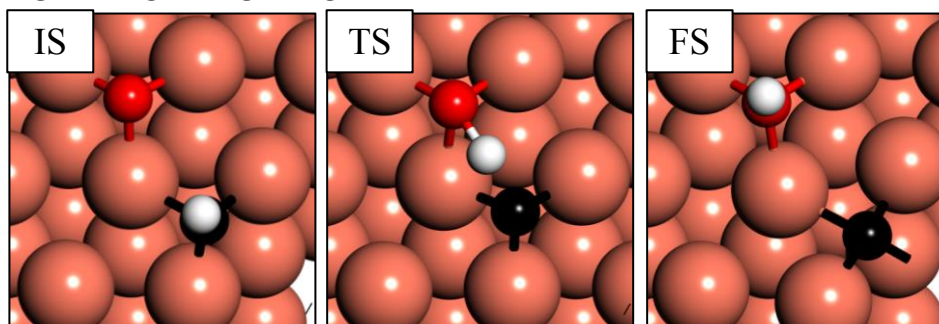
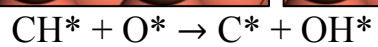
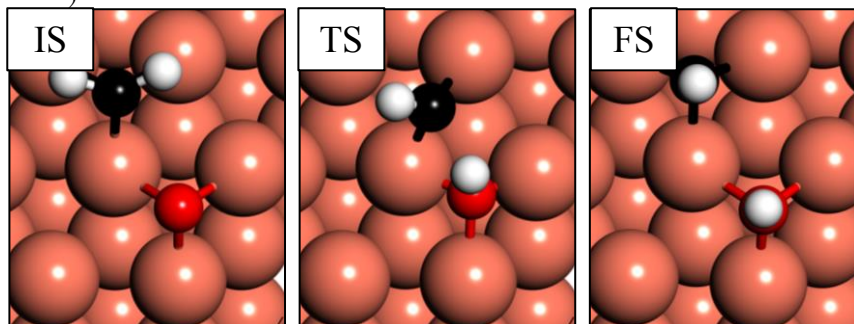
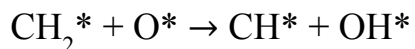
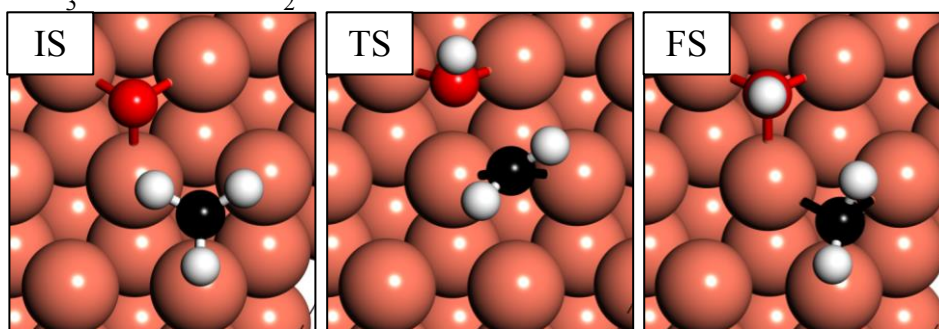
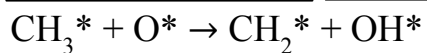
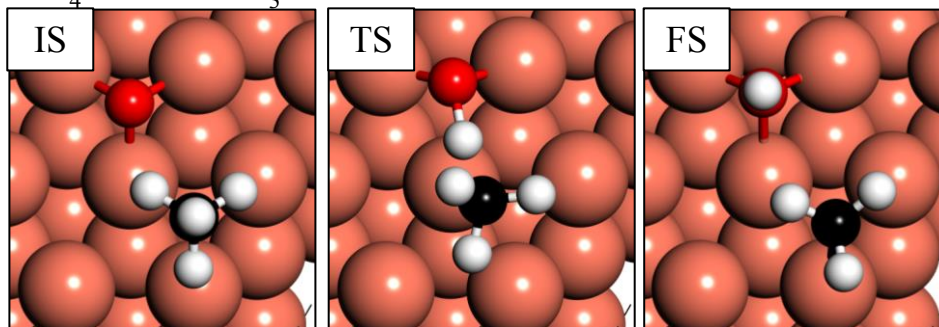
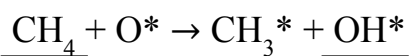


Figure B5 Initial, transition and final states of the sequential CH₄ dissociation steps on 1/16ML O-covered Cu (111). Cu, O, C and H atoms are shown in orange, red, black and white.

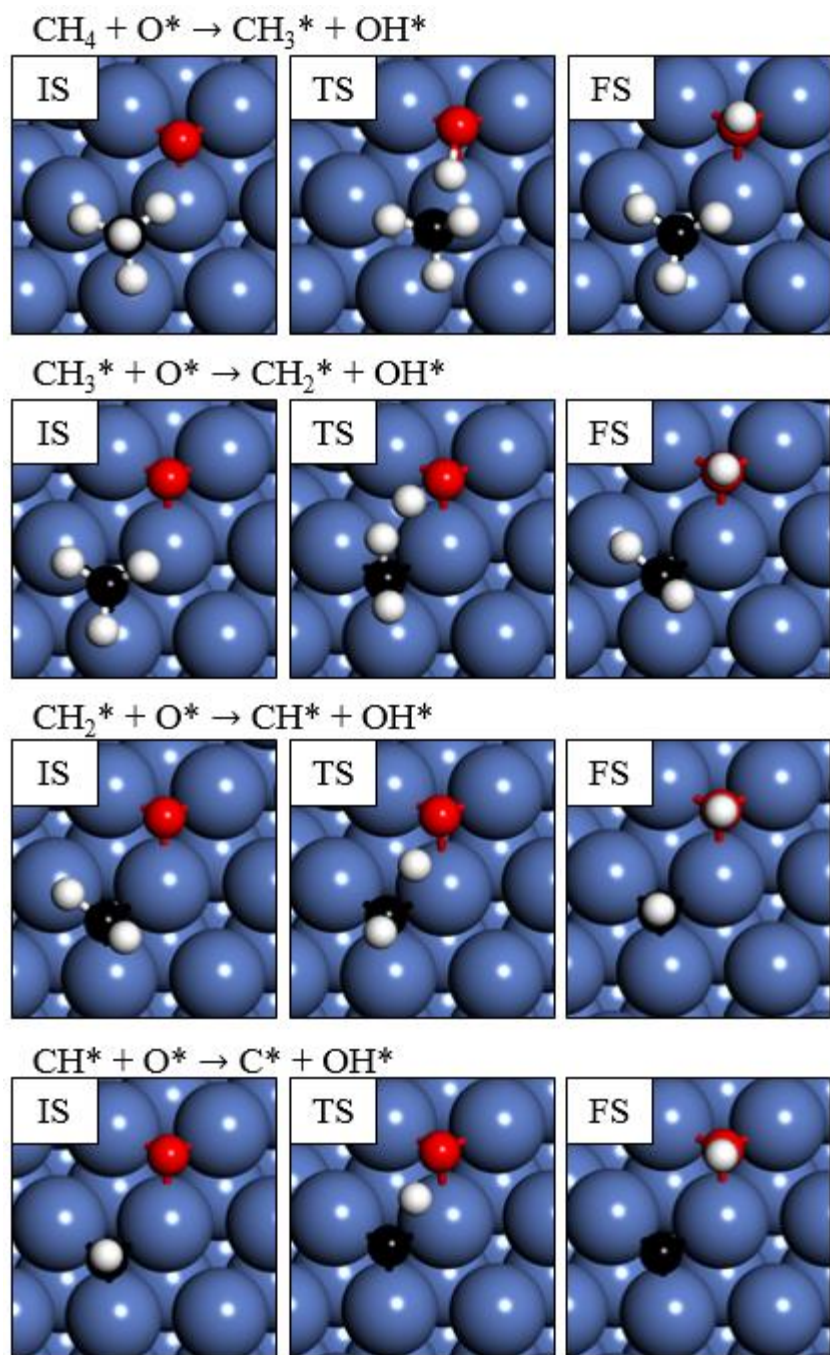


Figure B6 Initial, transition and final states of the sequential CH₄ dissociation steps on 1/16ML O-covered Ni (111). Ni, O, C and H atoms are shown in blue, red, black and white.

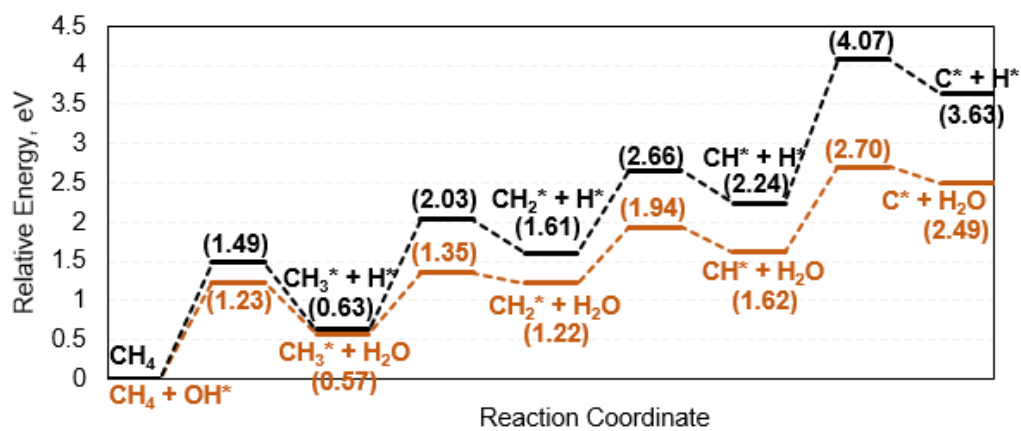


Figure B7 Energy profile for CH₄ dehydrogenation on clean (black) and 1/16 ML OH-covered (orange) Cu (111) surfaces.

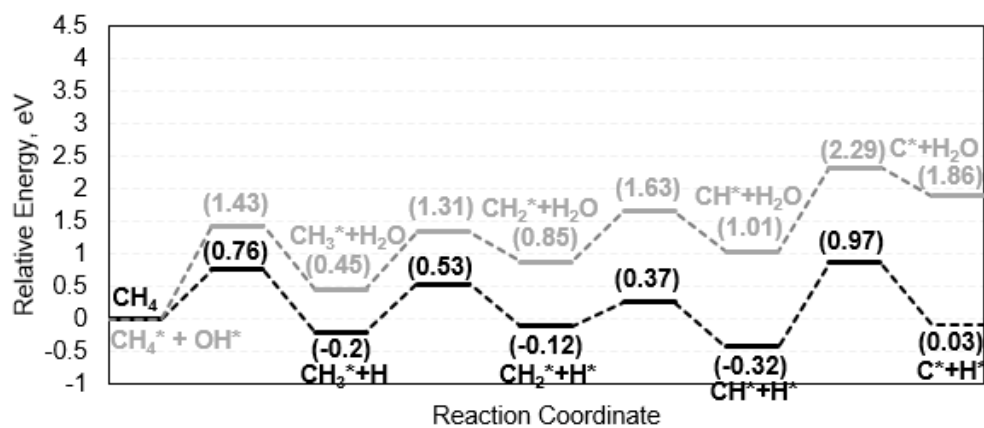


Figure B8 Energy profile for CH₄ dehydrogenation on clean (black) and 1/16 ML OH-covered (grey) Ni (111) surfaces.

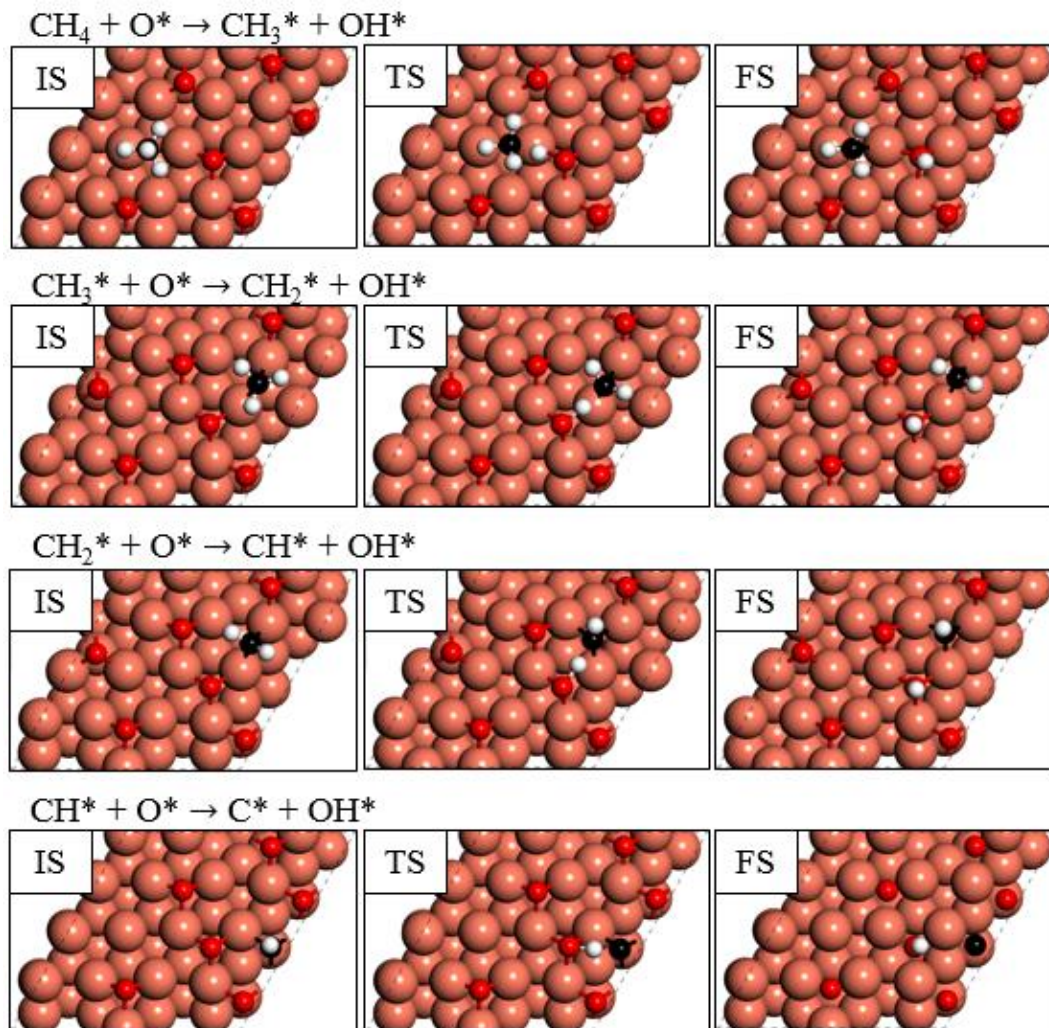


Figure B9 Initial, transition and final states of the sequential CH_4 dissociation steps on 6/16ML O-covered Cu (111). Cu, O, C and H atoms are shown in orange, red, black and white.

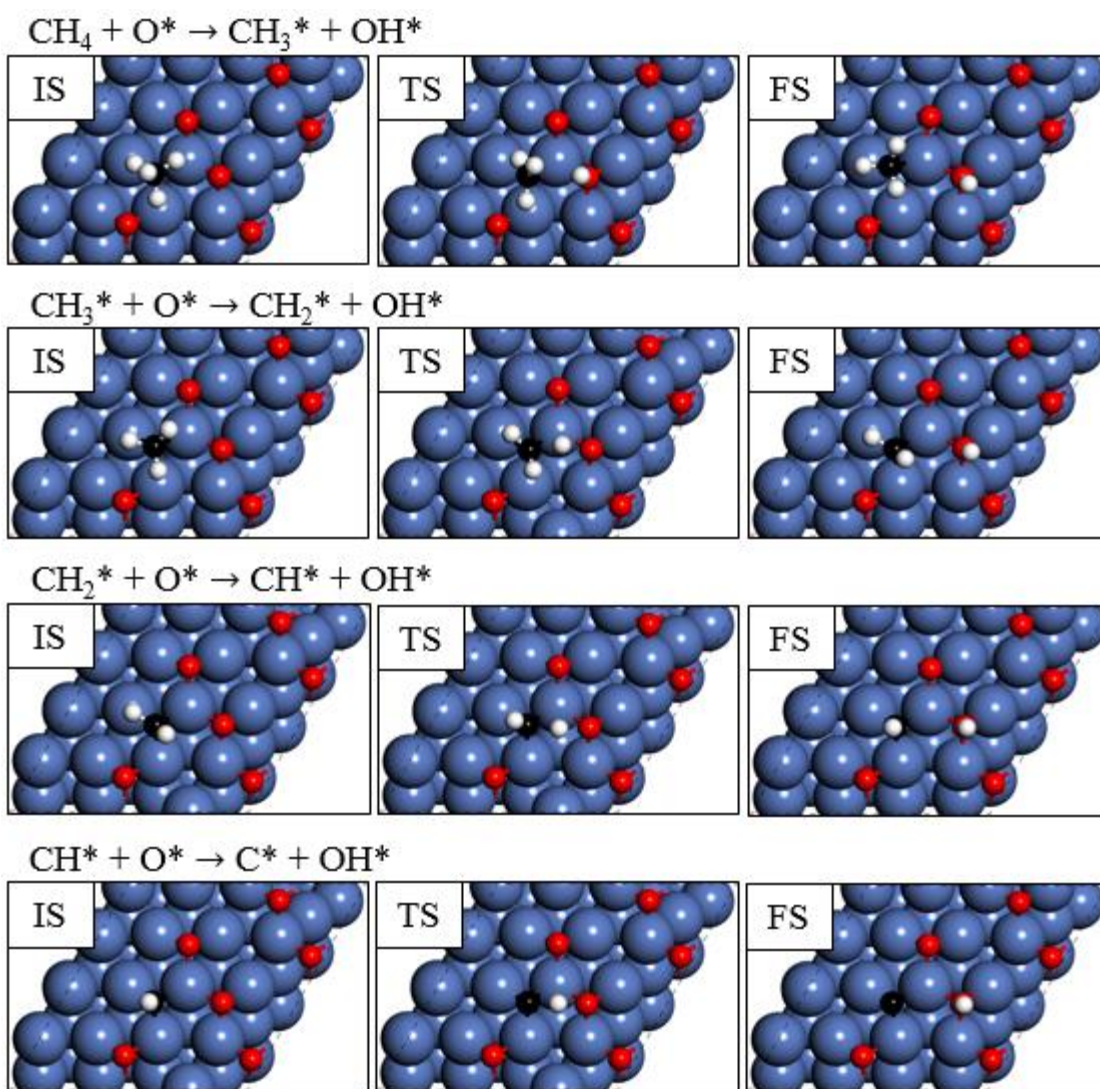


Figure B10 Initial, transition and final states of the sequential CH_4 dissociation steps on 6/16ML O-covered Ni (111). Ni, O, C and H atoms are shown in blue, red, black and white.

APPENDIX C

ADSORPTION AND DIFFUSION OF CARBON RINGS

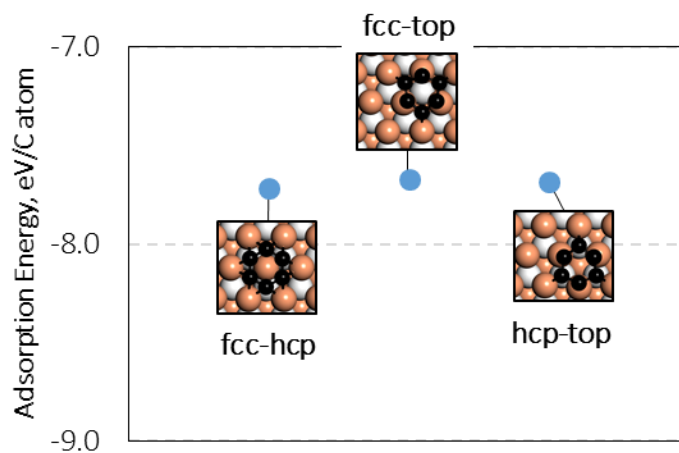


Figure C1 Adsorption energies and structures of three possible adsorption sites for a C6 ring on the Cu (111) surface. Top and second layer Cu atoms are colored in orange and white, respectively. Differences between adsorption energies are within 0.05eV/C from one another. The adsorption energies are calculated by:

$$E_{ads} = \frac{E_{sys} - E_{Cu\ slab} - n_C E_C}{n_C (= 6)} \quad (C.1)$$

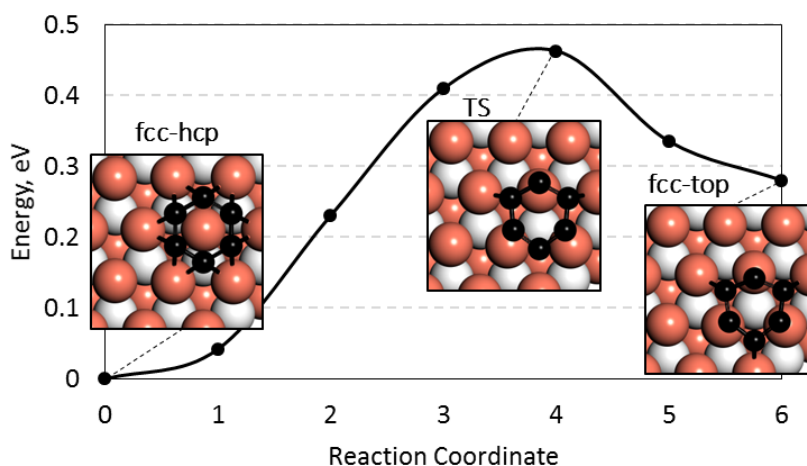


Figure C2 Diffusion of a C₆ ring on the Cu (111) surface from fcc-hcp site to fcc-top site obtained from NEB DFT calculations. Initial (fcc-hcp), TS (transition state) and final (fcc-top) images are also depicted. Top and second layer Cu atoms are colored in orange and white, respectively. Energy barrier for forward and reverse reactions are 0.46 eV and 0.18 eV, respectively.

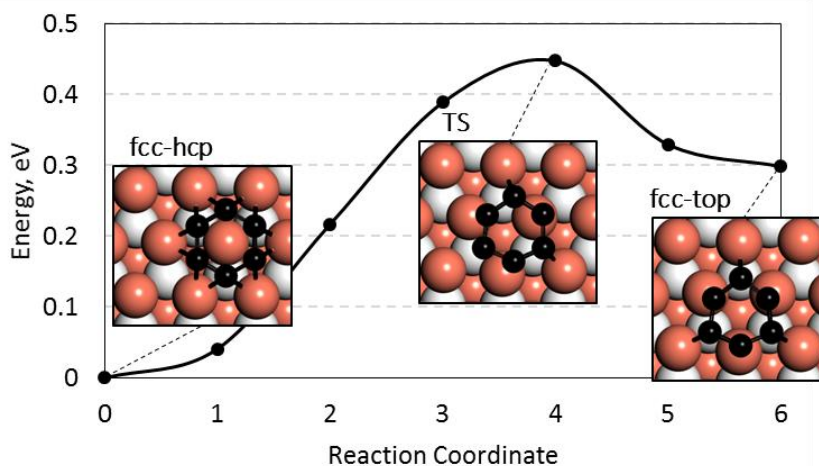


Figure C3 Diffusion of a C₆ ring on the Cu (111) surface from fcc-hcp site to hcp-top site obtained from NEB DFT calculations. Initial (fcc-hcp), TS (transition state) and final (hcp-top) images are also depicted. Top and second layer Cu atoms are colored in orange and white, respectively. Energy barrier for forward and reverse reactions are 0.45 eV and 0.15 eV, respectively.

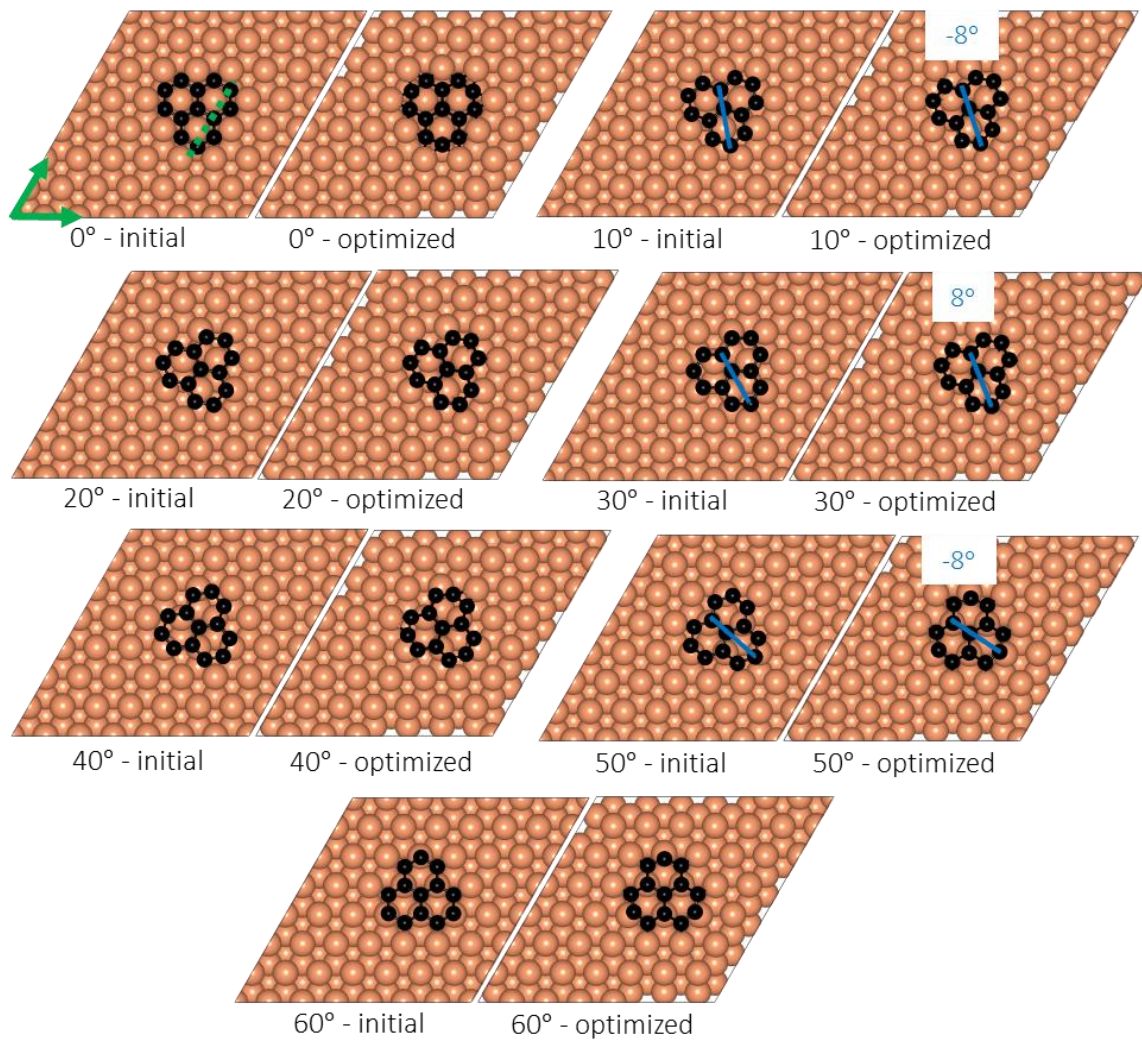


Figure C4 Rotation of a graphene fragment on the Cu (111) surface upon geometry optimization of initial alignments of 0° to 60° with the Cu lattice. Negative values correspond to anti-clockwise rotation.

APPENDIX D

C₂H₂ DECOMPOSITION ON SUPPORTED NANOPARTICLES

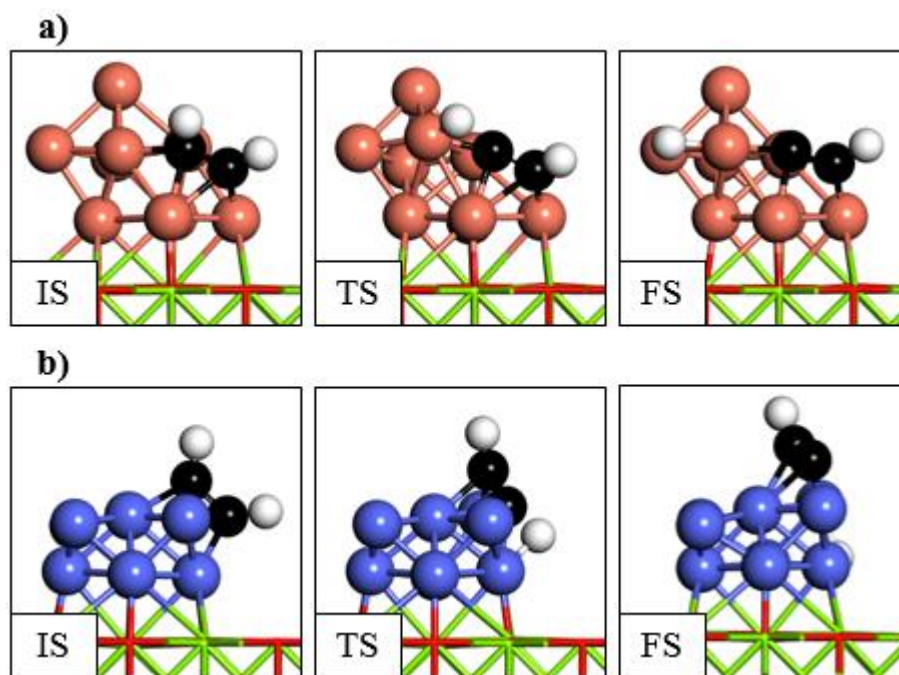


Figure D1 Initial, transition and final states of the dehydrogenation reaction of C₂H₂ on a) Cu and b) Co nanoparticles supported by MgO (100).

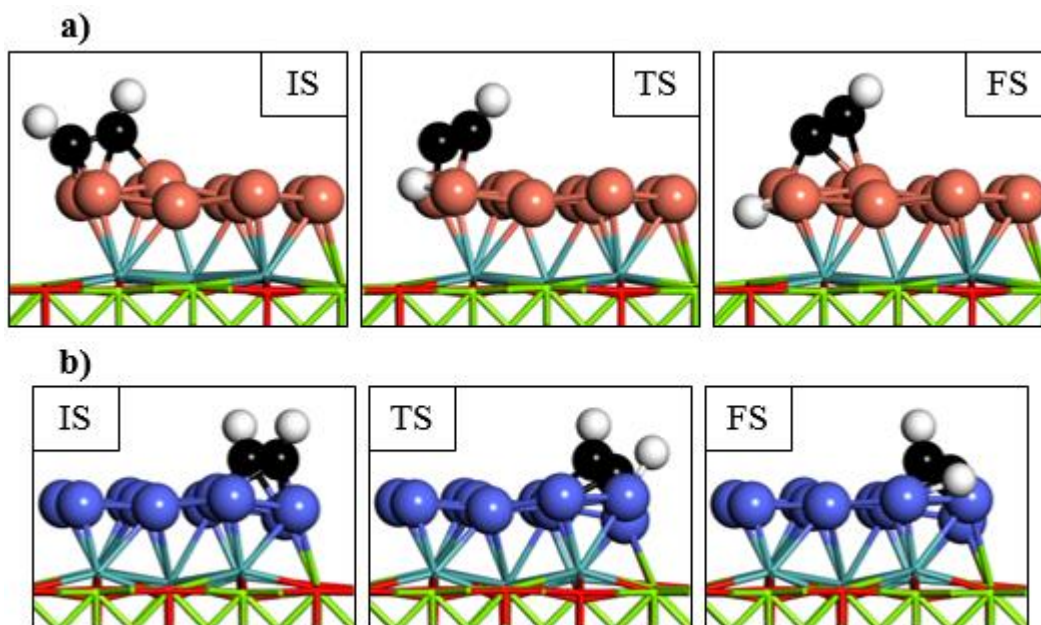


Figure D2 Initial, transition and final states of the dehydrogenation reaction of C_2H_2 on a) Cu and b) Co nanoparticles supported by Mo-doped MgO (100).

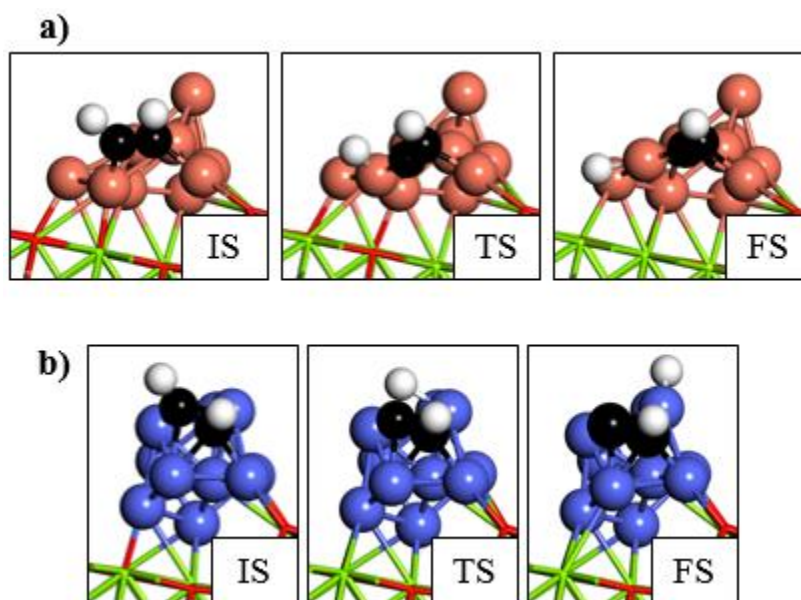


Figure D3 Initial, transition and final states of the dehydrogenation reaction of C_2H_2 on a) Cu and b) Co nanoparticles supported on the stepped MgO (105) surface.

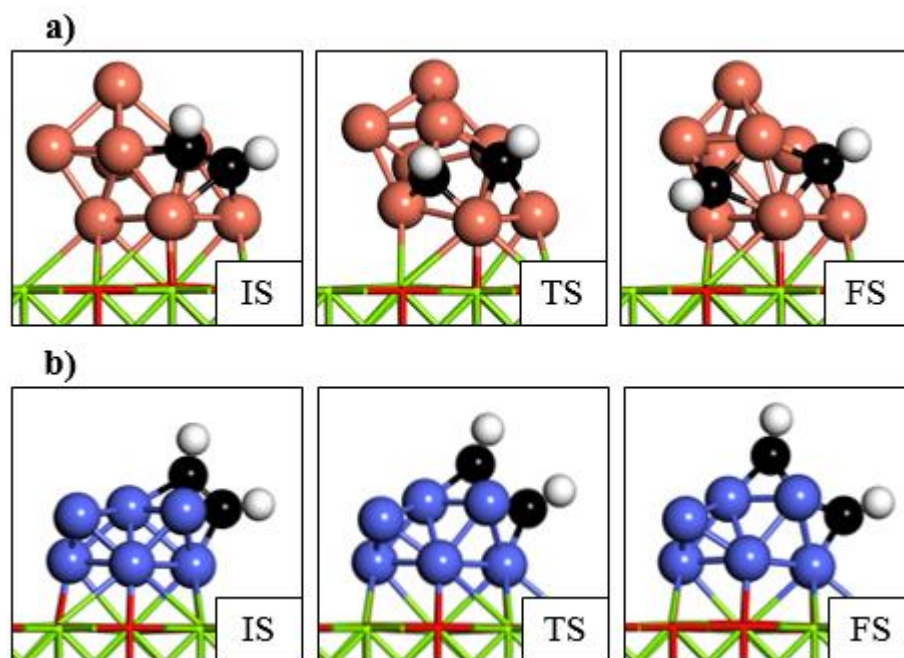


Figure D4 Initial, transition and final states of the CH-CH bond breakage of C_2H_2 on a) Cu and b) Co nanoparticles supported by MgO (100).

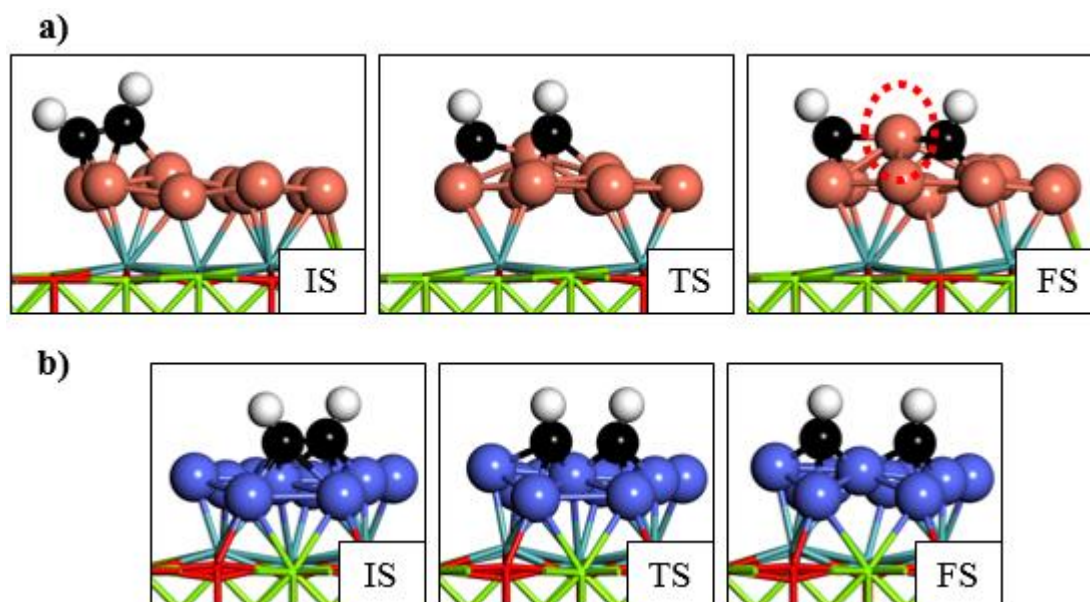


Figure D5 Initial, transition and final states of the CH-CH bond breakage reaction of C_2H_2 on a) Cu and b) Co nanoparticles supported by Mo-doped MgO (100). The Cu atom bridging between the two CH species is indicated in a)FS.

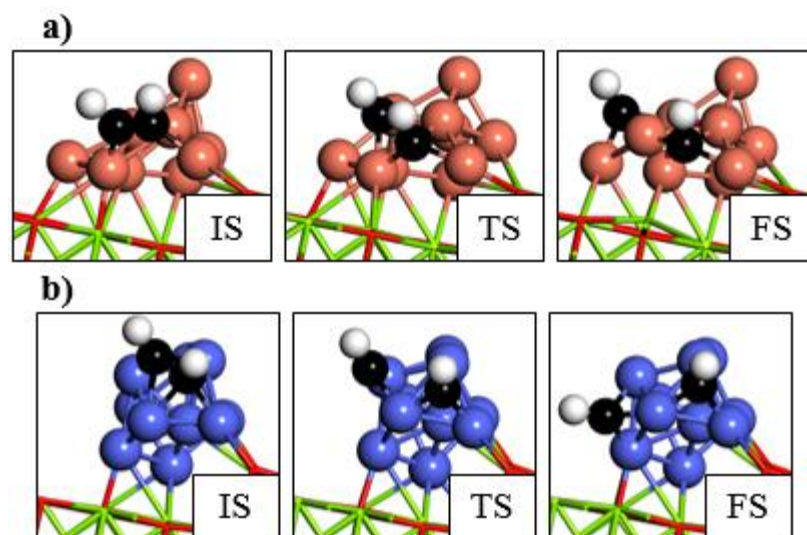


Figure D6 Initial, transition and final states of the CH-CH bond breakage reaction of C_2H_2 on a) Cu and b) Co nanoparticles supported on the stepped MgO (105) surface.